S-CUBED

A Division of Maxwell Laboratories, Inc.

W/O 42077 SSS-R-87-8801

GROUND MOTION SIMULATIONS FOR THRUST EARTHQUAKES BENEATH WESTERN WASHINGTON

S. M. Day
J. L. Stevens
T. G. Barker

Final Report

Submitted to:

Washington Public Power Supply System
3000 George Washington Way
Richland, Washington 99352

February 1988

P. O. Box 1620, La Jolla, California 92038-1620
(619) 453-0060

S-CUBED

A Division of Maxwell Laboratories, Inc.

W/O 42077 SSS-R-87-8801

GROUND MOTION SIMULATIONS FOR THRUST EARTHQUAKES BENEATH WESTERN WASHINGTON

S. M. Day
J. L. Stevens
T. G. Barker

Final Report

Submitted to:

Washington Public Power Supply System
3000 George Washington Way
Richland, Washington 99352

February 1988

P. O. Box 1620, La Jolla, California 92038-1620
(619) 453-0060

TABLE OF CONTENTS

TABLE OF CONTENTS (Continued)

LIST OF ILLUSTRATIONS

LIST OF ILLUSTRATIONS (Continued)

LIST OF ILLUSTRATIONS (Continued)

LIST OF ILLUSTRATIONS (Continued)

LIST OF ILLUSTRATIONS (Continued)

Figure **Page**

LIST OF ILLUSTRATIONS (Concluded)

LIST OF TABLES

I. INTRODUCTION AND SUMMARY

Numerical simulation of earthquake ground motion has some important advantages over the more conventional empirical approaches for estimation of spectral response and peak motion parameters. Empirical methods are based on regression analysis of the existing ground motion data base. Data are rather sparse at hypocentral distances less than about 50 km, and typically only fault distance and magnitude are included as independent variables. Numerical simulations, on the other hand, incorporate model parameters for which one can estimate bounds from geophysical observations and geological reasoning. One can then perform sensitivity studies with the model to estimate the corresponding bounds on ground motion. Conversely, the resulting sensitivities can then be used to focus additional geophysical studies on further bounding those specific parameters to which site ground motion is most sensitive.

We report here the results of a sensitivity study of ground motion at the WNP-3 site due to hypothetical, large subduction zone thrust earthquakes in western Washington state. As a preliminary step, we reviewed the geologic structure and tectonic setting at the site, in order to estimate bounds on thrust zone dip, maximum depth, and static stress drop for use in the sensitivity study. A synopsis of that review is given in Appendix A.

Section II describes the ground motion simulation method employed in the sensitivity studies for the WNP-3 site. The earthquake model incorporates the modern concepts of fault strength barriers and asperity failure by means of a deterministic subevent model. In addition, the model includes a stochastic element, in that a very large number of independent subevent contributions are superposed, with a large degree of incoherence, to produce the site motion. Finally, the source model retains a kinematic description of earthquake initiation location, rupture direction, rupture velocity, fault orientation, and final fault dimensions and static stress drop. This enables us to incorporate bounds on these kinematic parameters obtained from geophysical evidence. Propagation of the source radiation to the site is accomplished using ray theory, and limitations of the method are delineated in Section II.

The method is appropriate in the period range 0.1 to 5.0 seconds. At longer periods the wave propagation model begins to be limited by the use of a far field approximation, while at short periods, there is increasing uncertainty in the source and propagation models. In particular, it is well established empirically that earthquake acceleration spectra fall sharply, perhaps exponentially, above a cutoff frequency f_{max}. The observed cutoff is variable, but usually lies above about 5 to 10 Hz. However, the origin of f_{max}, and even whether it is primarily a source effect (Papageorgiou and Aki, 1983a) or a propagation effect (Hanks, 1982; Anderson and Hough, 1984), is still controversial. There is thus no well-accepted geophysical method by which to estimate f_{max} on a site-specific basis. For these reasons we do not present response spectral estimates for periods below 0.1 seconds in this report.

Section III describes test calculations with the model and comparison to strong motion observations. First, we analyze a data set from the May 2, 1983 Coalinga earthquake and its aftershocks. We derive source spectra from near-field data and show that the source spectra are consistent with the numerical source spectra scaled to stress drops ranging from 25 to 600 bars. We then simulate the ground motion from the main shock and from a large aftershock using the summation method proposed in Section II and show that the simulated response spectra agree very well with observed response spectra.

As a test of the model in a geometry very similar to that of the WNP-3 site, we apply it to the 1985 Michoachan, Mexico earthquake. We constrain the total moment of the model to equal the moment of the event determined from long period seismic records. We find excellent agreement between our predictions and observations at four stations located above or near the fault plane when we use subevents with a source dimension of 2.5 km and a local stress drop of 38 bars.

Section IV presents the results of the sensitivity study for the WNP-3 site. We find that the most critical parameters for the prediction of ground motion are fault dip and the up-dip width of rupture, which together determine the nearest approach of the rupture to the site. The simulations predict that even the largest earthquakes will not result in ground motion in excess of the SSE spectrum in the 0.2 to 10.0 Hz frequency band, provided that the thrust zone dips at 12 degrees or more and the nearest point on the fault is at least 40 km from the site. On the other hand, a magnitude 8.2 earthquake could exceed the SSE spectrum if the fault dips at the most shallow hypothesized angle and passes beneath the site.

II. GROUND MOTION SIMULATION METHOD

2.1 Introduction

It has become clear over the past two decades, from both teleseismic and strong motion studies, that crustal earthquakes are complex events, characterized by spatial inhomogeneity in both the velocity of rupture and stress drop. Evidence of this complexity is the disparity between low-frequency (or static) and high-frequency estimates of earthquake stress drops. As noted by Kanamori and Anderson (1975), stress drops for large earthquakes, as estimated statically or via low-frequency seismology, are concentrated in the range from 10 to 100 bars, with 30 bars being a representative value for interplate earthquakes. On the other hand, Hanks and McGuire (1981) studied 300 horizontal components of ground motion for moderate to large California earthquakes and concluded that RMS accelerations for these records implied, with relatively little scatter, stress drops of 100 bars.

A graphic illustration of the effect of source complexity on strong ground motion is provided by accelerograms recorded during the September 19, 1985 Michoacan, Mexico earthquake. Figure 2.1, from Anderson, *et al.* (1986), shows ground displacement, from double integration of the accelerogram recorded at the Caleta de Campos station directly above the fault plane of this event. The static displacement is well defined and equals roughly 100 cm on the north-south component. The displacement rise time is about 10 seconds. Figure 2.2, also from Anderson, *et al.* (1986), shows Fourier spectra of acceleration (N-S component) from the same station as well as two other stations within the aftershock zone of that event. The lower dotted curve shows the spectrum corresponding to a synthetic seismogram consisting of a ramp displacement function, with amplitude equal to 100 cm and rise time equal to 10 seconds. Clearly, high-frequency ground motion generation is controlled by irregularities, exceeding by nearly an order of magnitude the level one would estimate from the static fault parameters, assuming smooth slip.

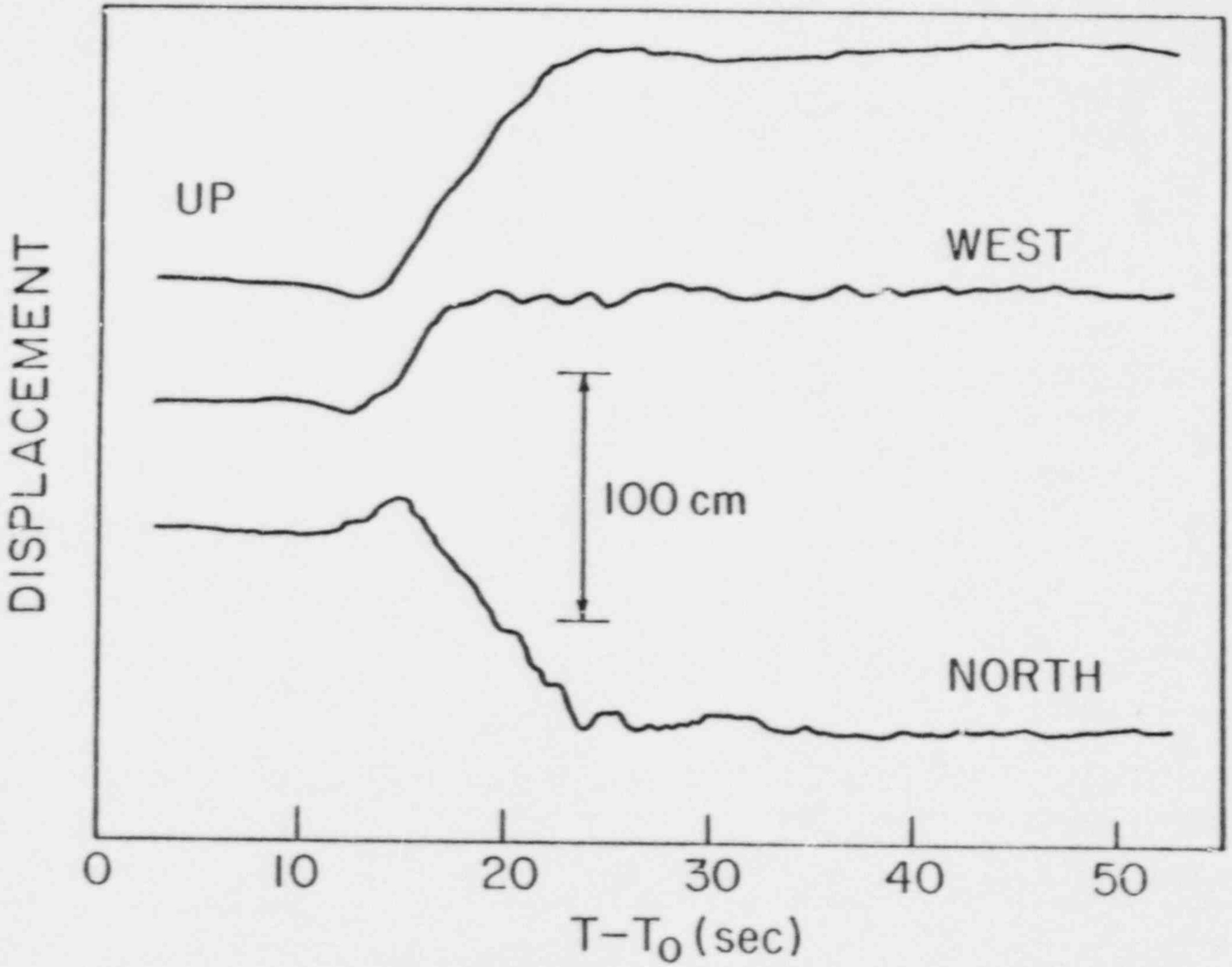

Figure 2.1. Ground displacement at Caleta de Campos, from double integration of accelerograms of the 19 September 1985 Mexico earthquake (from Anderson, *et al.*, 1986). The apparent rise time of slip, about 10 seconds, is consistent with the results of previous dynamic simulation, i.e., roughly 0.5 to 1.0 times the ratio of fault width to rupture velocity.

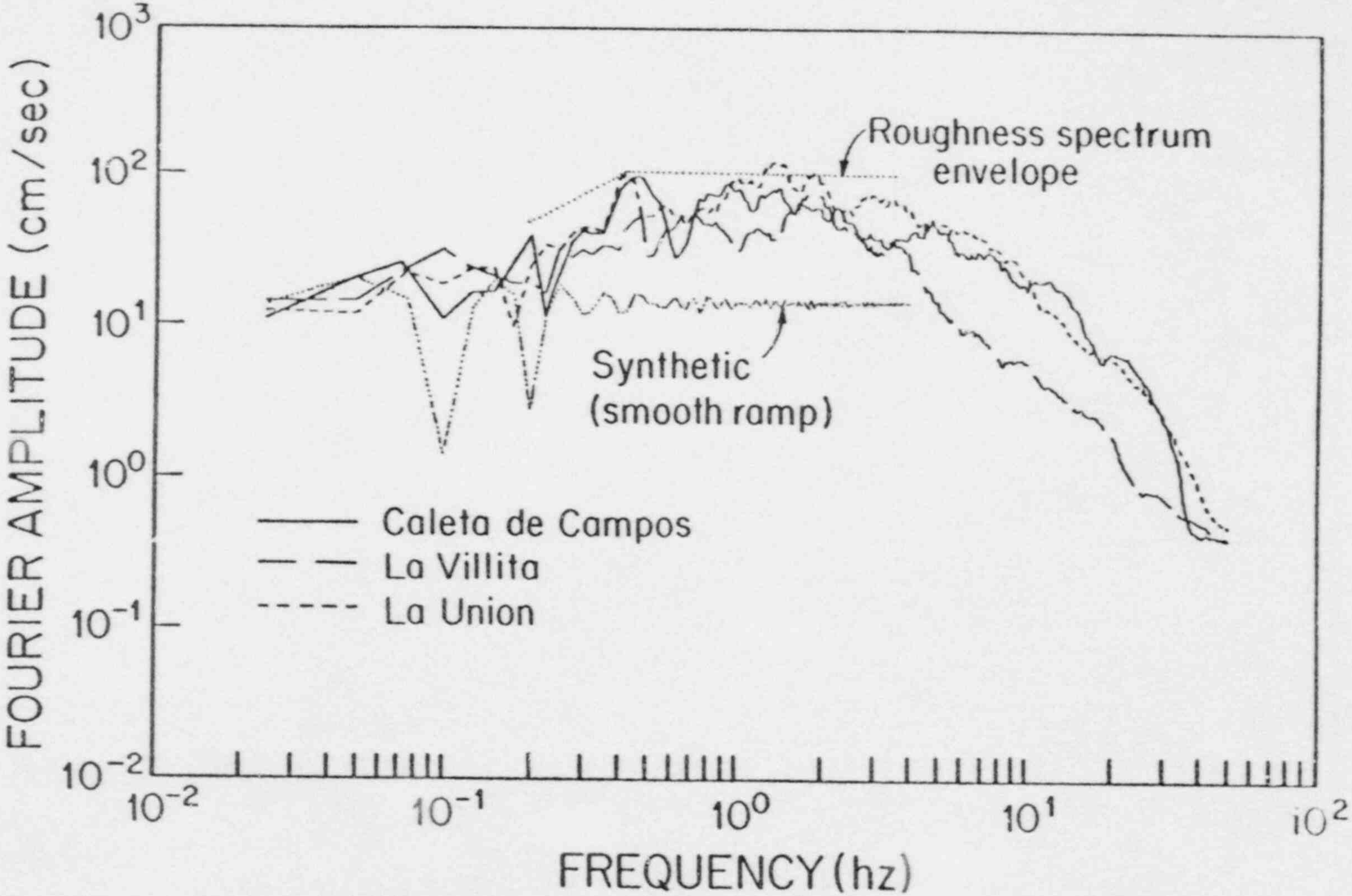

Figure 2.2. Fourier spectra of acceleration (N-S component) at the three stations above the aftershock zone of the 19 September 1985 Mexico earthquake (from Anderson, *et al.*, 1986). The lower dotted curve shows the spectrum corresponding to a synthetic seismogram consisting of a ramp displacement function.

In order to accommodate observations of this type, Aki (1979) developed the barrier concept, according to which the rupture front in an earthquake leaves behind unbroken patches. To give quantitative content to the barrier concept, Papageorgiou and Aki (1983a, b) proposed a specific barrier model, in which a large earthquake is viewed as an assemblage of small, disjoint, circular cracks. Each crack is assigned a stress drop, but because the perimeters of the individual cracks remain unbroken, the aggregate slip is much smaller than it would be if the same stress drop were incurred on a crack whose dimension was that of the whole assemblage. An individual crack is assumed to radiate as in the approximation proposed by Sato and Hirasawa (1973).

We employ an earthquake model which is similar to that of Papageorgiou and Aki. We have introduced some features designed to render the model appropriate for simulating high-frequency ground motion for large, subduction zone thrust earthquakes. In particular, we (1) represent subregion radiation by means of dynamic crack theory, (2) add a stochastic component to subregion dimensions, stress drops and rupture times, and (3) permit total slip duration at a point to be related to overall earthquake dimensions (as implied by Figure 2.1) by permitting subregions to reload and undergo repeated stress drops as the rupture expands to cover the whole fault plane.

By way of introduction, we consider the relationship between local stress drop $\Delta\tau_L$ and apparent global stress drop $\Delta\tau_G$ for an array of circular cracks. The average static slip $\bar{S}_L$ for a circular crack of radius a and stress drop $\Delta\tau_L$ is (Neuber, 1937)

$$\bar{S}_L = \frac{16}{7\pi} \frac{\Delta\tau_L a}{\mu} \tag{1}$$

where μ is the shear modulus. For a long fault, with uniform stress drop $\Delta\tau_G$, and with slip directed across its width (as might represent a large thrust event at a subduction zone), the average static slip (from Sneddon and Lowengrub, 1969) is

$$\bar{s}_G = \frac{3\pi}{16}\frac{\Delta\tau_G W}{\mu}, \tag{2}$$

where W is the fault width. If we replace the long fault with an assemblage of contiguous circular cracks which fill the fault surface, then (1) and (2) imply that $\Delta\tau_L$ must have the value

$$\Delta\tau_L = \frac{21\pi}{64}\frac{W}{a}\Delta\tau_G \tag{3}$$

in order to produce the same static slip as the uniform fault with stress drop $\Delta\tau_G$.

We can identify $\Delta\tau_G$ with the low-frequency stress drop obtained by seismic or geodetic means. If we set $\Delta\tau_G$ to the representative value of 30 bars, say, then (3) would imply that the product $\Delta\tau_L a$ is proportional to fault width. We prefer to interpret the characteristic dimension a and dynamic stress drop $\Delta\tau_L$ as local properties of the fault which are independent of the ultimate size to which a given earthquake rupture grows. In the case of local stress drop $\Delta\tau_L$, this viewpoint has empirical support in the apparent uniformity of stress drops as inferred from RMS accelerations, as cited above.

2.2 Earthquake Source Model

Our earthquake model simulates fault roughness by defining an assemblage of subregions, of average dimension $\bar{a}$($\bar{a} \equiv (A/\pi)^{1/2}$ where A is subregion area) as shown in Figure 2.3. A given subregion undergoes slip episodes which are dynamically independent of the rest of the fault. The radiation from each subregion slip episode is obtained numerically from a dynamic simulation of faulting, based on three-dimensional finite difference solutions to propagating crack problems (Day, 1982a,b; Stevens and Day, 1985). The radiated seismic pulses are scaled to the prescribed input values of subregion dimension $\bar{a}$ and average local subregion stress drop $\overline{\Delta\tau_L}$.

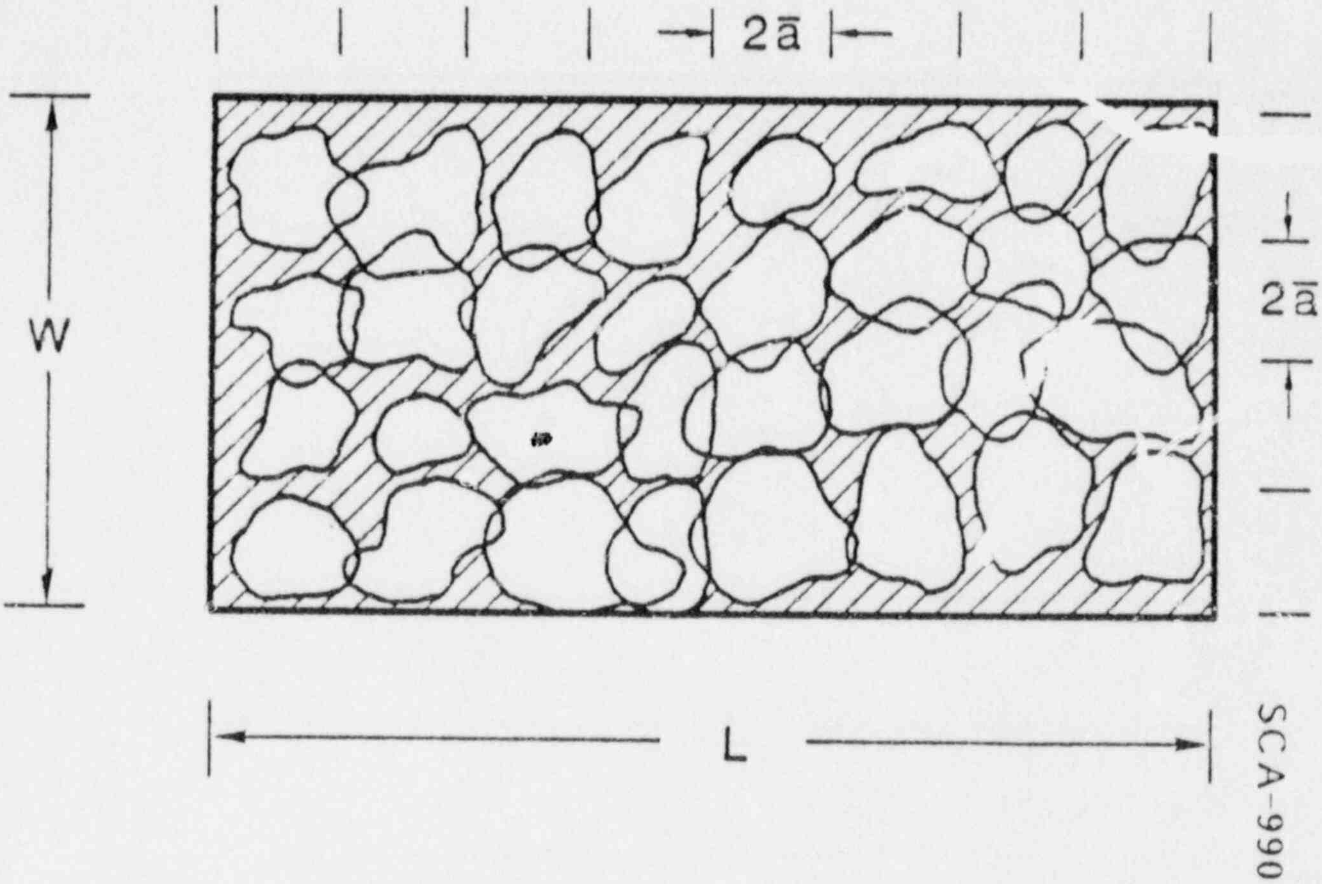

Figure 2.3. A schematic representation of the fault model. The fault surface is assigned a roughness denoted by a local subevent dimension with mean $\bar{a}$. Overall fault dimensions are denoted by length and width, L and W, respectively.

The actual crack simulations are described in detail in the publications cited above. Two subevent simulations denoted NRC1 and NRC7 are described in Appendix B. These two represent relatively simple and complex sources, respectively. In neither case is the crack geometry circular, and for convenience, we have defined $\overline{\Delta\tau_L}$ to be the stress drop which, applied uniformly to a circular crack of radius $\bar{a}$, would give the same average slip as the stressed crack used to represent each subregion.

While a dynamic crack model is used to represent the radiation from each subregion, a large earthquake is simulated by a kinematically prescribed superposition of subregion contributions. In addition, a stochastic element has been incorporated in this superposition.

Figures 2.4 and 2.5 show schematically how subregion contributions are combined. Each frame in Figure 2.4 is a snapshot of rupture at a given time. A global rupture front sweeps the fault with a prescribed rupture velocity near the shear wave velocity. When a given subregion is subsumed by the global rupture front, a subevent is triggered in that subregion. Shading in Figure 2.4 indicates subregions which are actively slipping; an arrow denotes subregions in which a slip episode has been completed. The mean stress drop and source dimension of the subevent are model inputs, and provision is made for these, as well as rupture arrival time, to vary randomly within prescribed variances.

Expansion of the rupture front and the consequent triggering of adjacent subregions will reload a subregion, and the model permits repeated failure of previously slipped subregions. This is illustrated schematically in Figure 2.4, where, for example, subregion A is triggered at time t_2, is locked at time t_3, but is then reloaded by expansion of the rupture front and triggers again at t_4. This secondary and other secondary subevents additionally load and trigger adjacent regions.

For an overall fault dimension large compared to $\bar{a}$, this retriggering process may have to occur repeatedly to build up sufficient slip to accord with seismically observable average stress drops. Figure 2.5 illustrates the resultant slip history at a representative point on a large fault which has undergone five slip episodes. From (1) and (2), we can deduce that the apparent global stress drop $\Delta\tau_G$ will be given by

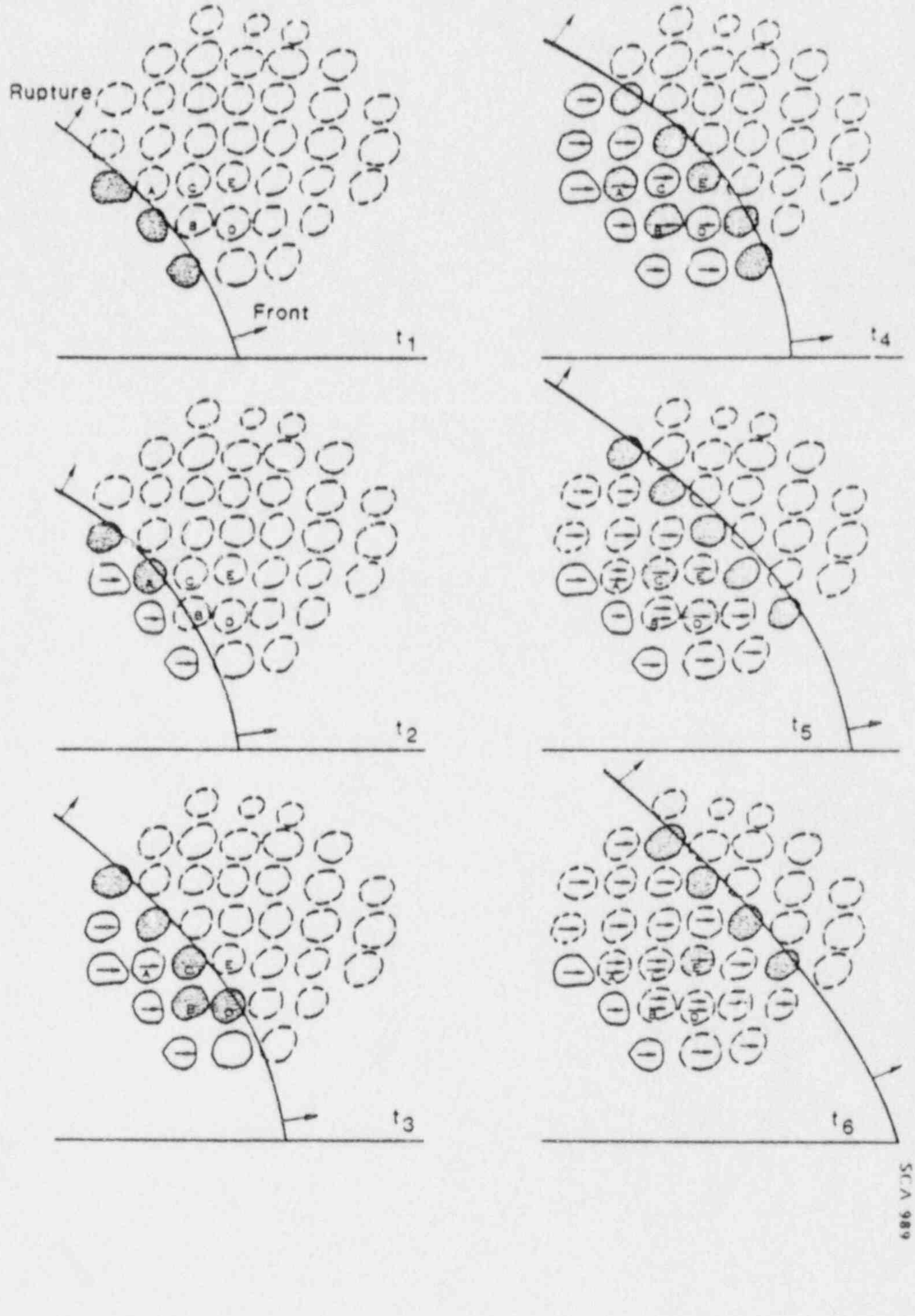

Figure 2.4. Schematic representation of rupture propagation, illustrating subevent initiation, reloading, and subsequent secondary failure of previously slipped subregions. Each frame is a snapshot of rupture at a given time. Shading indicates subregions which are actively slipping; an arrow is drawn in a given subregion for each completed slip episode incurred.

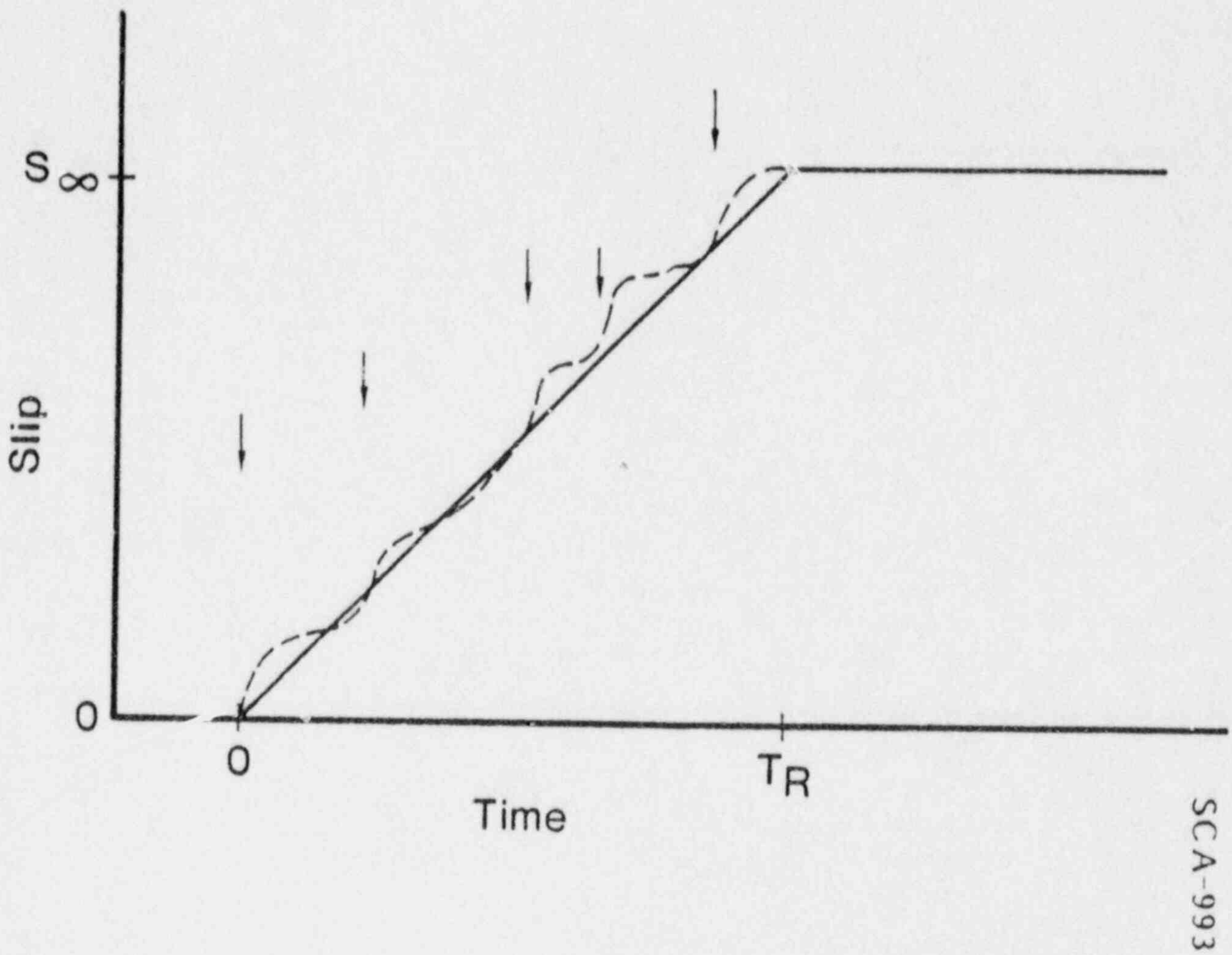

Figure 2.5. Schematic illustration of buildup of static slip at a point on the fault, through repeated triggering of a subregion. The overall slip and rise time are determined by the prescribed fault width and assumed values for the average stress drop and rupture velocity, through relations given in the text.

$$\Delta\tau_G = \frac{\bar{a}N}{W}\,\overline{\Delta\tau_L}\ , \tag{4}$$

where N is the average number of slip episodes of each subregion. If we fix $\bar{a}$ and $\overline{\Delta\tau_L}$, and set $\Delta\tau_G$ to agree with seismic and geodetic estimates (say 30 bars), then (4) determines N as a function of fault width:

$$N = \frac{W}{\bar{a}}\ \frac{\Delta\tau_G}{\overline{\Delta\tau_L}}\ . \tag{5}$$

Finally, we can estimate an appropriate global rise time, denoted by T_R in Figure 2.5. Dynamic modeling, as well as seismic observations, support the approximation

$$T_R \approx K\frac{W}{\nu_r}\ , \quad \frac{1}{2} < K < 1\ , \tag{6}$$

where ν_r is the rupture velocity. For example, dynamic earthquake simulations by Day (1982a) show slip rise time along rectangular faults of various aspect ratios. Rise times in Figure 2.7 of that paper agree with (6), as does the rise time of displacement observed above the Mexico earthquake fault plane, Figure 2.1.

In our model, $\Delta\tau_G$, $\overline{\Delta\tau_L}$, $\bar{a}$, W, and L are inputs. The number of slip episodes N is derived from (5); following rupture front arrival, these episodes are distributed randomly over the time interval determined by (6).

The moment magnitude M is derived from Hanks and Kanamori's (1979) expression

$$M = \frac{2}{3} \log M_0 - 10.7 \ , \tag{7}$$

and the total moment M_0 is:

$$M_0 = \frac{4}{7} N \ \overline{\Delta\tau_L} \ W L \bar{a} \quad . \tag{8}$$

2.3 Ground Motion Computation

The last section describes the source model used in the ground motion simulations. Ultimately, we are required to propagate the seismic pulses radiated by the $NWL/4\bar{a}$ subevents from their respective subregion locations to the surface site of interest. In order to accomplish this step expediently, and facilitate an extensive parametric study using reasonable computing resources, we employ the following approximations: (1) Geometrical ray theory is used to propagate the subevent pulses from source region to the site. (2) To simplify the ray calculations, we use a horizontally stratified, anelastic earth model. (3) The Fraunhofer approximation (see Appendix B) is employed to compute the source radiation of each subevent directed along each ray path.

The stratified earth approximation is justified in that the available geophysical characterization of the WNP-3 site is highly generalized and does not warrant using a complex, two-dimensional or three-dimensional earth structure at this time. The Fraunhofer approximation is generally appropriate when the condition

$$\bar{a}^2 \ll \frac{\lambda R}{2} \quad , \tag{9}$$

is satisfied, where λ is the minimum wavelength of interest and R the minimum source-receiver separation. Inequality (Equation 9) is satisfied up to about 5 Hz for all simulation geometries of interest to us. Above 5 Hz, we are still justified in using the Fraunhofer approximation, however, even though Equation (9) fails for some geometries (e.g., $\bar{a}$ = 2.5 km, R $\approx$ 25 km). The reason that Equation (9) is overly conservative when we consider very high frequencies (i.e., $\lambda << a$) is that high-frequency radiation is derived from stopping phases, as analyzed in detail by Madariaga (1977). Stopping phases emanate from localized segments of the subevent periphery, and effectively involve a source dimension much less than $\bar{a}$.

The adequacy of ray theory is more difficult to assess. Certainly local site resonances are neglected under ray theory; this is probably not significant, since the WNP-3 site is on hard rock. Surface wave contributions are neglected, but, at the high frequencies of interest in the study (0.5 to 10 Hz), they are unlikely to be significant for the relatively deep sources and short horizontal ranges of interest here. In test simulations of shallow earthquakes observed at larger ranges, we did see some possible evidence of breakdown in the ray approximation, in that ray theory estimates of ground motion are low compared to a number of published observations at the same range. Further numerical experiments demonstrated that the shortfall is associated with near-grazing incidence of shear wave energy at the base of shallow strata in the earth model. Repeating the simulations in a uniform halfspace gave results in excellent agreement with observations of peak velocity, peak acceleration, and response spectral ordinates. In our WNP-3 parameter study, we have identified cases where significant energy may be incident on the site at low angle to the vertical, and we have repeated these calculations using a uniform halfspace. Thus, we believe this modeling uncertainty has been well quantified and that the engineering results are presented accurately in Section IV. For a test simulation of recordings of the 1985 Mexico event, furthermore, in which the source receiver geometry resembles that of interest for WNP-3, ray theory appears to be fully adequate, and leads to excellent agreement with observations. These tests are discussed further in Section III.

An important question is whether scattering effects (or unmodeled source complexities) are sufficiently important in the 0.5 to 10 Hz range to substantially suppress the double-couple radiation pattern of the subevents. There is evidence that, at high frequencies, scattering mechanisms act to homogenize explosion (e.g., Gupta and Blandford, 1983) and earthquake (Hanks and McGuire, 1981) radiation patterns. Our analysis of Coalinga aftershock data discussed in Section III clearly confirms this effect for strong motion data in the frequency band of interest. For this reason, we use a homogenized radiation pattern derived from the average radiation pattern for each subevent.

2.4 Analysis of the Model

In Appendix C we describe a simplified model for ground motion which captures the main features of the earthquake model described here. Equation C.15 gives the peak pseudo-relative velocity V of an oscillator, of natural frequency f_0 and critical damping fraction γ, in response to ground motion from the model:

$$V(f_0) \sim \frac{0.32\sqrt{\pi}}{2} \frac{(\Delta\tau_L/2)a}{\rho\beta R} \left[\frac{\lambda \ln(T_u f_0)}{\gamma f_0}\right]^{1/2} e^{-\pi R f_0/\beta Q} . \quad (10)$$

In Equation 10, T_u is the duration of the dominant part of the signal, R is the distance from which the dominant signal originates, and λ is the shot rate, i.e., the rate of arrival at the receiver of direct shear wave phases from the subevents. Equation C.15 is written in terms of the Brune stress drop estimate, which is approximately $\Delta\tau_L/2$, as reflected in Equation 10. Equation 10 expresses the result, from random vibration theory, that peak oscillator response is proportional to rms acceleration of the input.

We now use this expression to show that our earthquake model is consistent with observed scaling of short period teleseismic P waves from large earthquakes. This is important, since we have no strong motion recordings of subduction-zone earthquakes at distances nearer than 50 km and magnitudes greater than approximately 8. Therefore, we must calibrate our model using events up to magnitude 8 and rely on the model to carry the correct magnitude dependence of short-period seismic radiation when applied to hypothetical events of larger magnitude.

Houston and Kanamori (1986) have defined a short-period magnitude measurement which does not saturate with increasing magnitude as does conventional body wave magnitude m_b. They call this measurement m_b, and they define it to be proportional to ground displacement, as measured at the maximum amplitude of the entire short-period teleseismic P wave train. Figure 2.6, from Houston and Kanamori, shows the behavior of m_b as a function of moment magnitude. The straight line has a slope of 0.53 indicating (using Equation 7)

$$m_b \propto M_0^{0.35} , \qquad (11)$$

as reported by Houston and Kanamori.

Equation 10, applied to a short-period seismometer, implies that our model predicts m_b proportional to $\lambda^{1/2}$, the square root of the shot rate. For a teleseismic signal. λ should be proportional, approximately, to the total number of subevents divided by the duration of signal. The total number of shots is proportional to total event moment M_0, and the duration should be roughly proportional to $M_0^{1/3}$. Thus

$$\lambda \propto \frac{M_0}{M_0^{\,1/3}} = M_0^{\,2/3}$$

$$\hat{m}_b \propto \lambda^{1/2} \propto M_0^{\,1/3} . \qquad (12)$$

This is almost exactly the Houston and Kanamori empirical result, Expression 11.

We can carry out the same calculation for the standard ω^2 source model, with similarity assumed, which predicts an acceleration amplitude spectrum proportional (above the corner frequency) to $M_0^{1/3}$. Since peak seismometer response is proportional to rms ground acceleration, we have

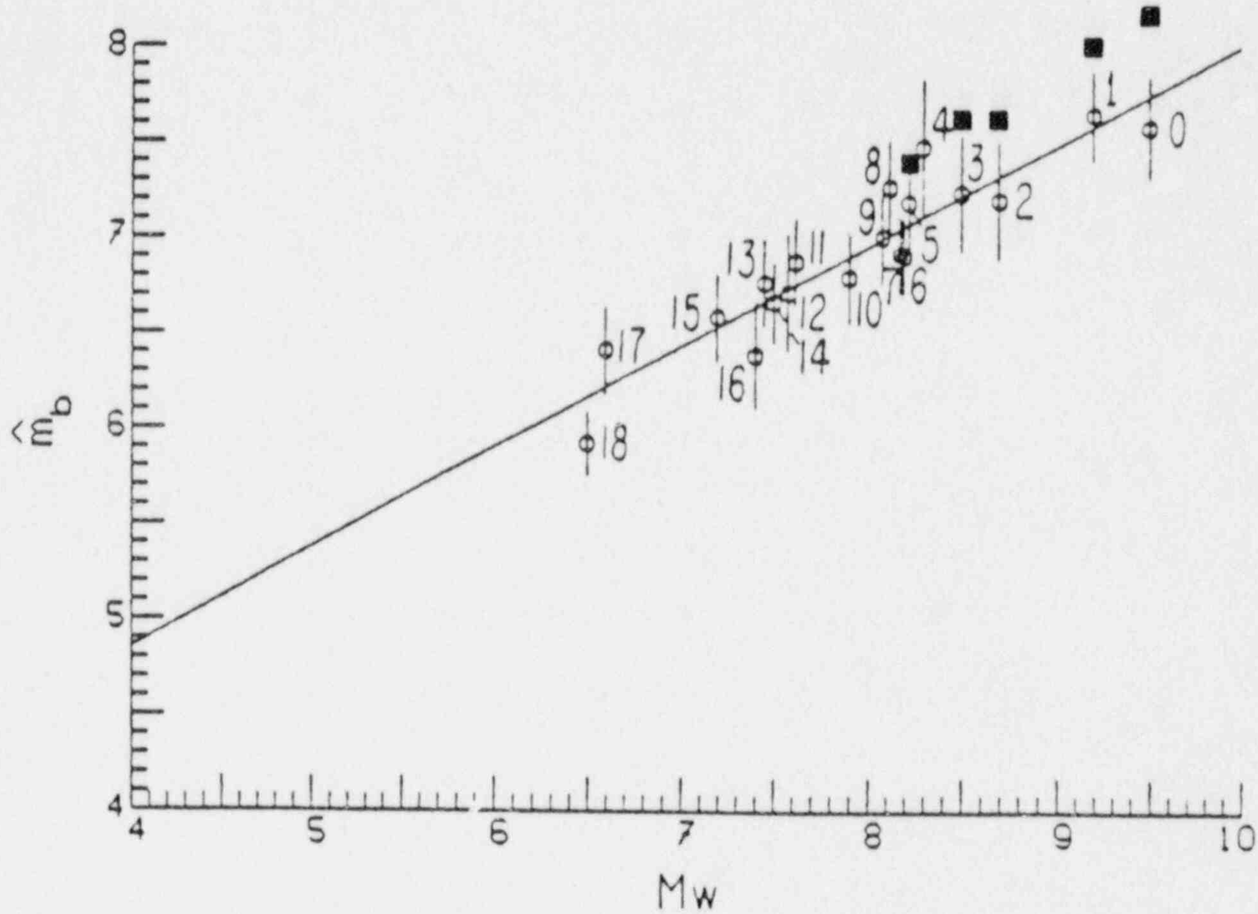

Figure 2.6. Observations of m_b versus moment magnitude, from Houston and Kanamori (1986). Open circles are earthquake data, bars are standard deviations on m_b values (solid squares refer to theoretical simulations studied by Houston and Kanamori).

$$\hat{m}_b \propto \left[\frac{M_0^{2/3}}{M_0^{1/3}}\right]^{1/2} = M_0^{1/6} \ .$$

Although this asymptote is not in accord with the observations summarized in Figure 2.6 and Expression (11), Boore (1983) has shown through a more complete analysis that the self-similar ω^2 model is also consistent with Figure 2.6.

Thus, the earthquake model used for ground motion computations in this report has short-period scaling properties consistent with seismic observations (although we cannot rule out the self-similar ω^2 model as an alternative). This analysis also supports our treatment of subevent dimension a as a fixed parameter, with N proportional to total fault slip via Equation 5. For example if we held N fixed instead, by making a proportional to overall fault dimension, then $\lambda \propto a^{-2}$ and m_b would be independent of moment, in contradiction to Figure 2.6 and empirical expression (11).

III. COMPARISONS WITH STRONG MOTION OBSERVATIONS

3.1 Introduction

In the last section, we described an earthquake source model which incorporates, in a consistent fashion, much of the understanding of earthquake mechanics developed by observational and theoretical seismic studies over the past two decades. Particular attention was given to the very difficult problems associated with predicting high frequency seismic excitation. The modern concepts of fault strength barriers and asperity failure were incorporated into the model, using the fully deterministic simulations of Day (1982a, b). Thus, we have avoided the spurious high frequency source phenomena which have beset some earlier ground motion simulations which relied wholly on kinematic source prescriptions (this problem is discussed in some detail in Day's 1982a paper, and was further reviewed for the Nuclear Regulatory commission by Swanger, *et al.* (1981)). In addition to this deterministic element, the model incorporates a stochastic element, in that a very large number of independent contributions combine, with a large degree of incoherence, to produce the site ground motion. This stochastic character is clearly mandated by numerous analyses of high frequency earthquake ground motion, including studies by Hanks and colleagues (Hanks and Johnson, 1976; Hanks, 1979; McGuire and Hanks, 1980; Hanks and McGuire, 1981) as well as others (e.g., Boore, 1983; Joyner, 1984; Papageorgiou and Aki, 1983a, b). Finally, the model retains a kinematic element, in that rupture initiation, rupture direction, rupture velocity, and final fault dimensions and static stress drop are kinematically prescribed. This permits us to incorporate information about gross earthquake parameters obtained from teleseismic and geodetic observations. It also permits us to perform sensitivity studies of rupture directivity and focusing effects.

Our objective is to apply the model to hypothetical, large subduction zone thrust earthquakes in western Washington state. Since there is no such event in the historical record for the region, we have no reliable site specific estimates of the dynamic fault parameters appropriate for such an event. We are faced, therefore, with the following imperatives:

1. We should perform our predictive simulations using a generic earthquake model which incorporates well accepted values of gross earthquake parameters such as average stress drop ($\Delta\tau_G$), and geophysically observable geometric parameters such as fault zone orientation and dimensions, but otherwise contains as few free parameters as possible.

2. These few remaining free model parameters should be set for consistency with high frequency seismic observations and the predictions of the resultant generic model must be tested against existing strong motion data sets.

In this section we test the model predictions against strong motion recordings of the 1983 Coalinga, California earthquake (M = 6.7) and some of its aftershocks and the 1985 Michoacan, Mexico earthquake (M = 8.1). Comparison with the Coalinga data set demonstrate the appropriateness of the subevent model NRC1 and leads us to reject subevent model NRC7. The comparison also leads us to modify the subevent radiation pattern representation to bring model predictions into better accord with ground motion observations. Finally, comparison with the Coalinga data set shows the appropriateness of our summation procedure, at least for modeling moderate-sized earthquakes.

As a more specific test of the model, we applied it to the geometry of the 1985 Mexico earthquake. The observed hypocenter and fault geometry for this event was input to the model, but otherwise the model was applied exactly as it would have been for a predictive simulation of a hypothetical event. We fixed the average, or global, rupture velocity at 3.5 km/sec, which is fairly representative of seismic inferences of this parameter for large earthquakes. The local roughness dimension $\bar{a}$ was set in all cases at 2.5 km. Values of this order find some support in strong motion studies. For example, Anderson, *et al.* (1986) estimated this parameter to be 3 to 4 km on the basis of acceleration Fourier spectral shape for the 1985 Mexico earthquake. In addition, Irikura (1985) estimated a roughness radius of 2 km from strong motion recording of a 1983 magnitude 7.1 earthquake in the Japan Sea. The value of the local dynamic stress drop $\overline{\Delta\tau}_L$ was adjusted to obtain agreement with the response spectral levels of the recorded ground motion, with N determined by the constraint that the total moment of the simulated event agree with seismic estimates of moment obtained from long-period seismic studies. The resulting value for $\overline{\Delta\tau}_L$ was 38 bars.

The results show the model to be quite accurate in its predictions of ground motion for this event. We obtain excellent agreement with the observed ground motion peaks, response spectral ordinates, and strong motion duration.

At the end of Chapter 4 we will compare the model predictions with two other strong motion data sets. The first is a set of empirically-derived average response spectra for subduction zone earthquakes, compiled by Heaton and Hartzell (1986). The second is the one rock-site response spectrum which is currently available for the March 3, 1985, Valparaiso, Chile earthquake. In each case model predictions and data are in excellent agreement, using the same values of $\bar{a}$ and $\overline{\Delta\tau}_L$. These same parameter values were retained for the WNP-3 prediction simulations, as well.

In the following sections, response spectral estimates are presented for frequencies up to 10 Hz. At higher frequencies, there is increasing uncertainty about the earthquake and wave propagation models, as discussed in the introduction. In particular, there is uncertainty about the mechanism controlling the observed high frequency decay of earthquake acceleration spectra, which is often approximately exponential above some cutoff frequency, f_{max} (e.g., Anderson and Hough, 1984). We note, however, that our ground motion time history computations have been computed with a 20 Hz Nyquist frequency, and peak acceleration estimates are based on this higher cutoff rather than the 10 Hz cutoff of the response spectral displays.

3.2 Comparison With 1983 Coalinga Earthquake and Aftershocks

An excellent strong motion data set was collected from the 1983 Coalinga Earthquake and its aftershocks by the California Division of Mines and

Geology and by the U. S. Geological Survey. This data set gives us an opportunity to compare our numerical source model with actual near field data and to see if our modeling procedure is appropriate for earthquakes in the magnitude 6 to magnitude 7 range.

Our procedure for modeling large earthquakes consists of adding together the seismic radiation from a large number of smaller subevents. In our modeling work, we have used subevent source functions derived from numerical calculations combined with ray theory to predict the ground motion at a given observation point. Since aftershocks are small and relatively simple events located close to a large event, we expect them to have characteristics similar to the subevents that we are using in our source modeling. These events therefore provide an important constraint on our subevent model.

3.2.1 Coalinga Aftershock Data

A large number of instruments were placed near Coalinga after the magnitude 6.7 main event by the U. S. Geological Survey (Mueller, *et al.*, 1984) and the California Division of Mines and Geology (Shakal and Ragsdale, 1983). As a result, there is an excellent data set for the Coalinga aftershocks. Eight aftershocks were selected for analysis. Parameters for these events and for the main shock (from Eaton, 1985) are listed in Table 3.1. Strike, dip, and rake were derived from focal plane orientations. Since the fault and auxiliary planes were not identified, there are two possible values of strike, dip, and rake for each event.

Event 2 was well recorded at 5 CDMG stations and at seven USGS stations. All other events were recorded at two CDMG stations. The station and event locations are shown in Figure 3.1. The CDMG data is prefiltered and is good over a frequency band of approximately 0.5 to 20 Hz. The USGS acceleration records were converted to displacement using the method of Iwan, *et al.* (1985), followed by high-pass filtering.

Empirical source functions were derived from the aftershock data in the following way. Since the observed waveforms are dominated by the shear arrival (especially on the horizontal components), the first step is to calculate a

TABLE 3.1

PARAMETERS OF COALINGA EVENTS

Event	Date	Time	M	Depth (km)	sdr_1	sdr_2
1	05/02/83	23:42:38	6.70	10.01	307,67, 90	127,23,90
2	05/09/83	2:49:12	5.30	12.04	293,48, 73	136,44,107
3	06/11/83	3:09:52	5.20	2.40	17,50, 90	197,40,90
4	07/09/83	7:40:51	5.39	9.02	18,41, 64	165,54,69
5	07/22/83	2:39:54	6.04	7.37	355,38, 78	159,53,81
6	07/22/83	3:43:01	5.02	7.89	342,30, 90	167,60,90
7	07/25/83	22:31:40	5.33	8.42	348,38, 90	168,52,90
8	09/09/83	9:16:14	5.30	6.69	334,75,-19	68,72,16
9	09/11/83	11:48:06	4.48	10.04	350,32, 90	180,58,90

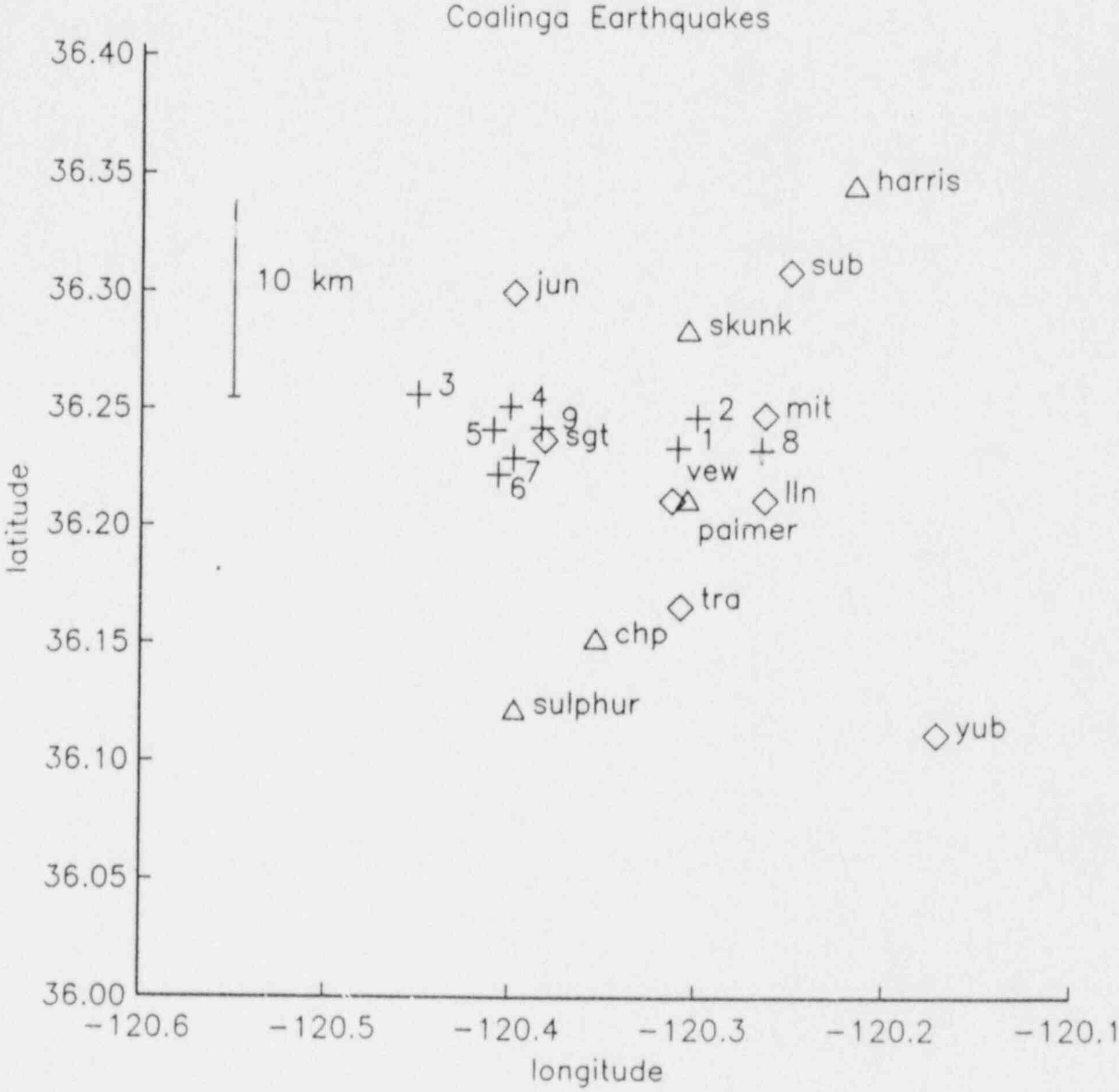

Figure 3.1. Locations of the Coalinga mainshock (1) and aftershocks (2 to 9), and the CDMG and USGS stations used in this study.

shear wave Green's function for the source to receiver path using the source parameters for the earthquake and a model for the Coalinga earth structure. The Coalinga earth structure, derived from the model of Eaton (1985), is listed in Table 3.2. Next, the data was windowed in a band of five seconds around the peak displacement. The windowed data was then transformed to the frequency domain and divided by the Green's function to give the empirical source function.

One fact that was immediately apparent from these results is that there is no correlation between the observed amplitude variations and the radiation pattern predicted from the source mechanism. Correcting for the radiation pattern increases the scatter in the data, particularly on recorders that are predicted to be nearly nodal. Furthermore, the two horizontal components of the data are usually approximately equal in amplitude, and the use of the theoretical receiver function to predict the relative amplitude of the two components almost always increased the difference between the source function derived from the two components.

In order to achieve more consistent results, we modified the procedure and derived a homogenized Green's function and used this function to infer the empirical source functions. The Green's function is a product of a source radiation pattern factor, a geometric spreading factor, a transmission coefficient, an attenuation function, and a (three component) receiver function. We assumed that the geometric spreading factor, attenuation function, and transmission coefficients are accurately predicted theoretically, but the radiation pattern factor and receiver function are not.

We tested several possible ways of deriving a homogenized Green's function and looked for the one that gave the most consistent results. To do this, we first replaced the receiver function of the horizontal components with an average receiver function such that each component of the receiver function was equal in magnitude. We tried this two ways – averaging only the horizontal components of the Green's function and averaging all three components of the Green's function. Second, we replaced the source radiation pattern factor with an average value of 0.6 – the value of the magnitude of the radiation pattern

TABLE 3.2

COALINGA EARTH STRUCTURE

Depth (km)	Thickness (km)	P (km/sec)	S (km/sec)	Density (gm/cc)	Q
1.50	1.50	2.50	1.40	2.10	100
3.50	2.00	4.30	2.40	2.50	240
7.00	3.50	4.70	2.60	2.60	260
9.00	2.00	5.60	3.20	2.70	320
14.00	5.00	5.80	3.30	2.70	330
15.50	1.50	6.30	3.60	2.70	360
28.00	12.50	6.60	3.80	2.70	380
∞	∞	7.95	4.50	2.90	450

factor averaged over the focal sphere. In all cases, we preserved the magnitude of the Green's function and retained the sign of the real part of the receiver function for each component.

In Table 3.3, we show the results of this test applied to the May 9 Coalinga aftershock. To derive this table, we averaged the logarithm of the spectra in the 1 to 10 Hz frequency band for each component at each station divided by the corresponding Green's function, and then calculated the mean and standard deviation of these averaged spectra over all stations and components. A small standard deviation indicates that the source spectrum is being recovered consistently from all of the available data. The results show a large improvement in consistency when the horizontal components are averaged, and a smaller, but significant increase in consistency when the source radiation pattern is also averaged. There is a very slight, and probably insignificant improvement in consistency when only the two horizontal components are averaged rather than all three. Based on these results, we derive our empirical source functions by dividing the windowed shear arrival by a Green's function that has been homogenized using an average radiation pattern and an average of the two horizontal components.

Spectra of the empirical source functions for Event 2 derived from all of the usable USGS and CDMG data are shown in Figure 3.2. The results are very consistent, especially over the 1 to 10 Hz frequency band. Because the data is high-pass filtered, the source functions are not valid below about 0.5 Hz; however it appears from comparison of the higher frequency data to source spectra from numerical models that the source functions are consistent with a moment of about 10^{17} Newton-meters, which is the value predicted from the standard moment-magnitude relation for an event of magnitude 5.3.

The amplitude of the source function in the 1 to 10 Hz frequency band depends on the moment and the stress drop of the earthquake. Since we do not have long period information, we cannot directly measure the moment of each event and then infer the stress drop. However, we can use the high frequency information to define a relation between moment and stress drop for

TABLE 3.3

LOG SPECTRAL AVERAGES OVER THE 1 TO 10 HZ FREQUENCY BAND FOR MAY 9, 1983 AFTERSHOCK WITH DIFFERENT LEVELS OF GREEN'S FUNCTION HOMOGENIZATION

	Average	Standard Deviation
Theoretical Green's Function	15.58	0.49
Horizontal Components Averaged	15.39	0.16
All Three Components Averaged	15.46	0.17
Horizontals, Radiation Pattern Averaged	15.43	0.10
All Components, Radiation Pattern Averaged	15.50	0.10

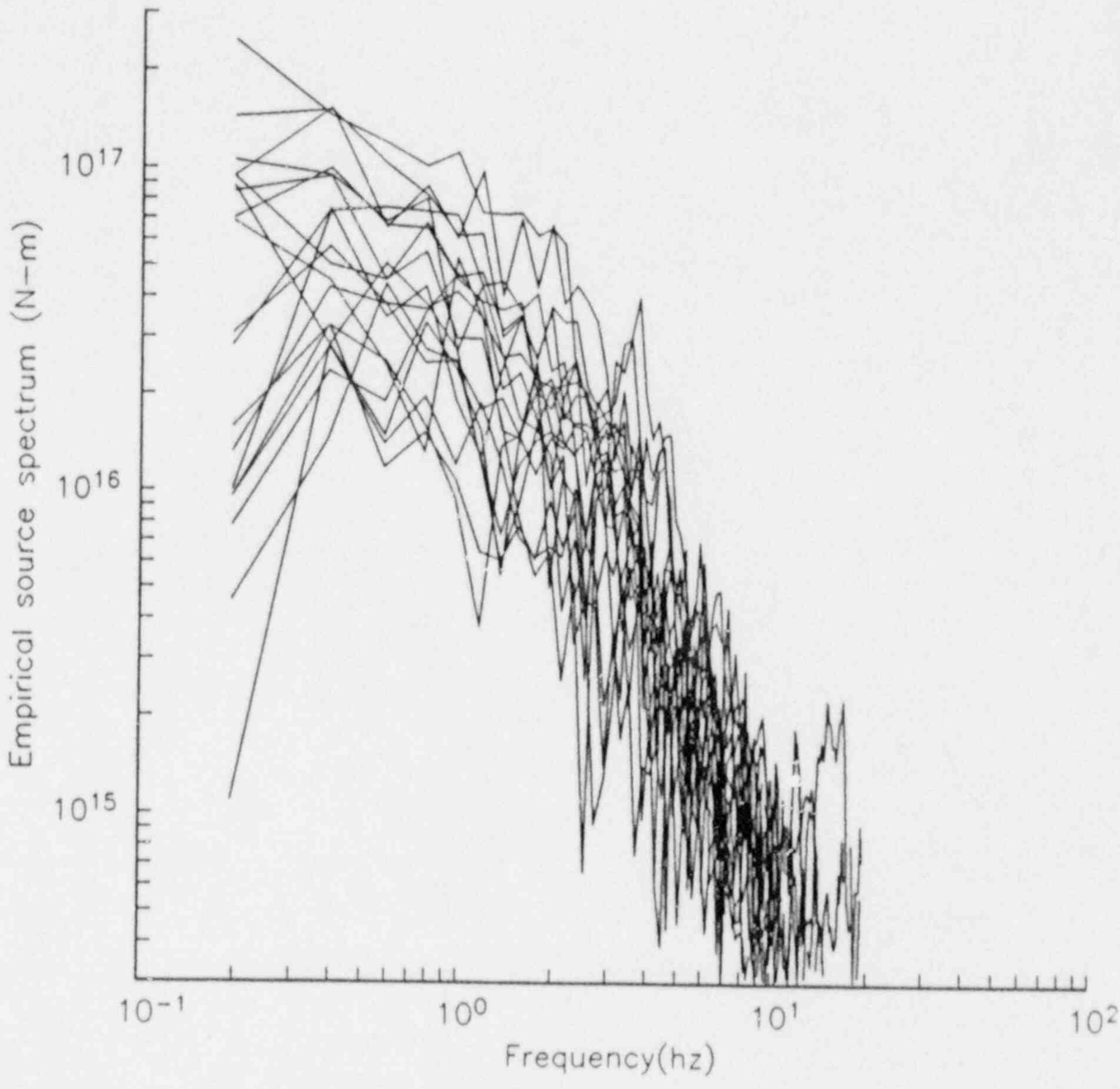

Figure 3.2. Source spectra derived from all observations of the May 9, 1983 Coalinga aftershock.

each event. This is done by scaling the numerical source functions over a range of moments for a number of stress drops and searching for results that minimize the difference between the data and the scaled source model over the 1 to 10 Hz frequency band. While neither moment nor stress drop is independently well determined by the data, this relation is very well defined and can be used to determine stress drop given an estimate of moment or to estimate moment given the stress drop.

In Figure 3.3, we show the results of this procedure applied to the data for two numerical source functions. This figure shows the data fit obtained when the two source functions are scaled to a moment of 10^{17} Newton-meters and a stress drop of 200 bars. The long-dashed line shows the numerical source functions which have been averaged over all azimuths. The solid line shows the average empirical source function for the event and the short-dashed lines are ± one standard deviation curves for the empirical source spectra. The fit between the numerical and empirical source functions is excellent in both cases, although there is some indication that numerical source NRC7 is excessive in amplitude at the high end of the frequency range.

Figure 3.4 shows how the stress drop was determined for this event. Each point on the plot represents a minimum in the data misfit as described above. The bars show the standard deviations on the data fit over the 1 to 10 Hz frequency band (the averages, misfits and standard deviations were calculated for the logarithm of the spectra). The horizontal line show the moment predicted by the moment-magnitude scale. In this case the data is consistent with this moment if the stress drop of the event is 200 bars. This result is the same for both empirical sources. Also shown on the plot is the result for a Brune source model. The Brune source model leads to stress drops that are about one-half as large as the stress drops predicted from the numerical source models.

In some cases, the data are not consistent with the moment predicted by the moment-magnitude scale. In Figure 3.5, for example, we show the moment and stress drops estimated for Event 9 which had a magnitude of 4.5 and an implied moment of 6.3×10^{15} Newton-meters. With this moment, the estimated stress drop is 2 kilobars. As can be seer [illegible] gure 3.5, however, the

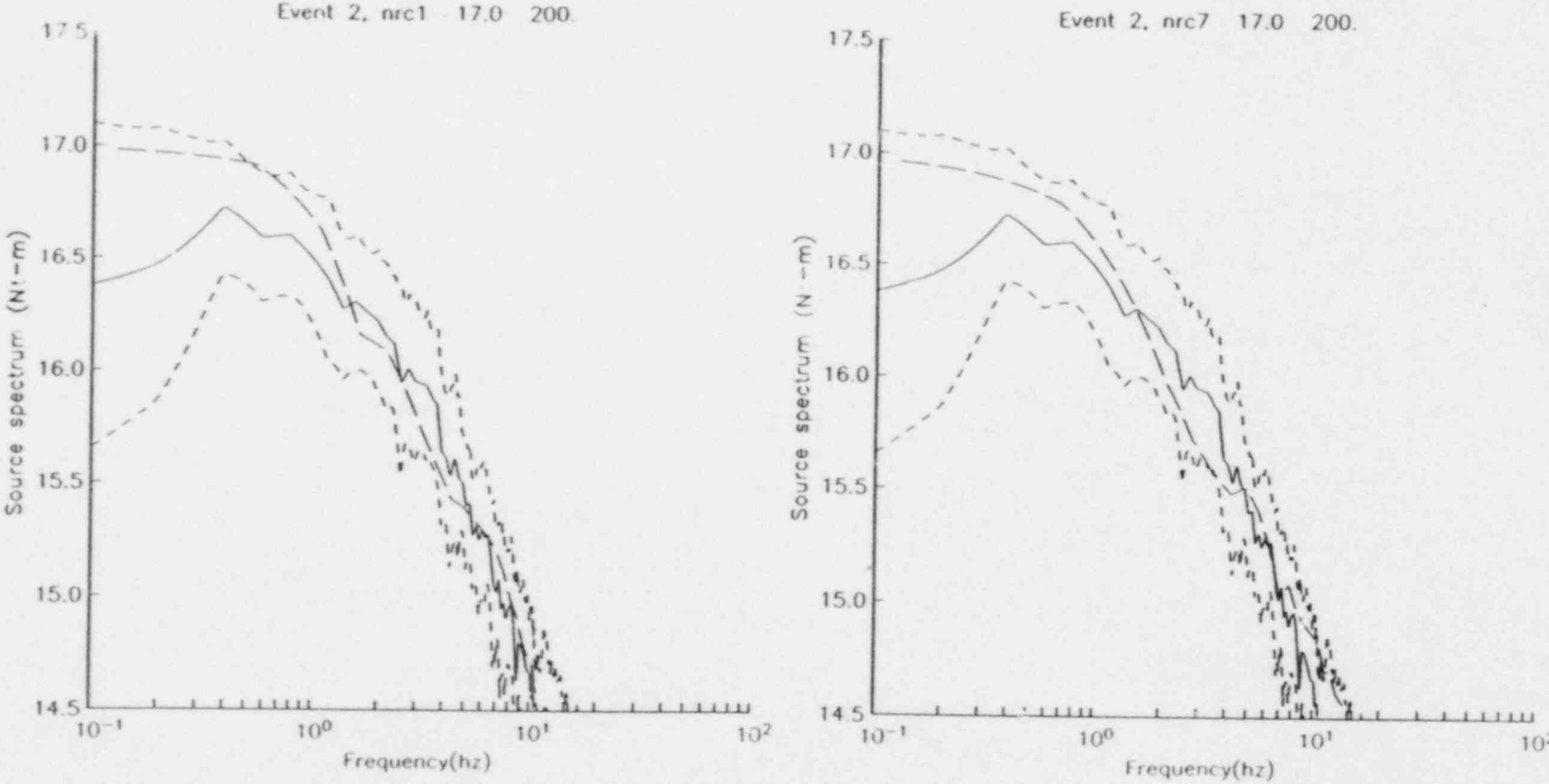

Figure 3.3. Average source spectrum of the May 9, 1983 aftershock (solid line) and ± 1 standard deviation (short dashed lines), together with the numerical source spectrum nrc1 (left) and nrc7 (right) (long dashed line) averaged over all takeoff angles and scaled to a moment of 10^{17} newton-meters and a stress drop of 200 bars.

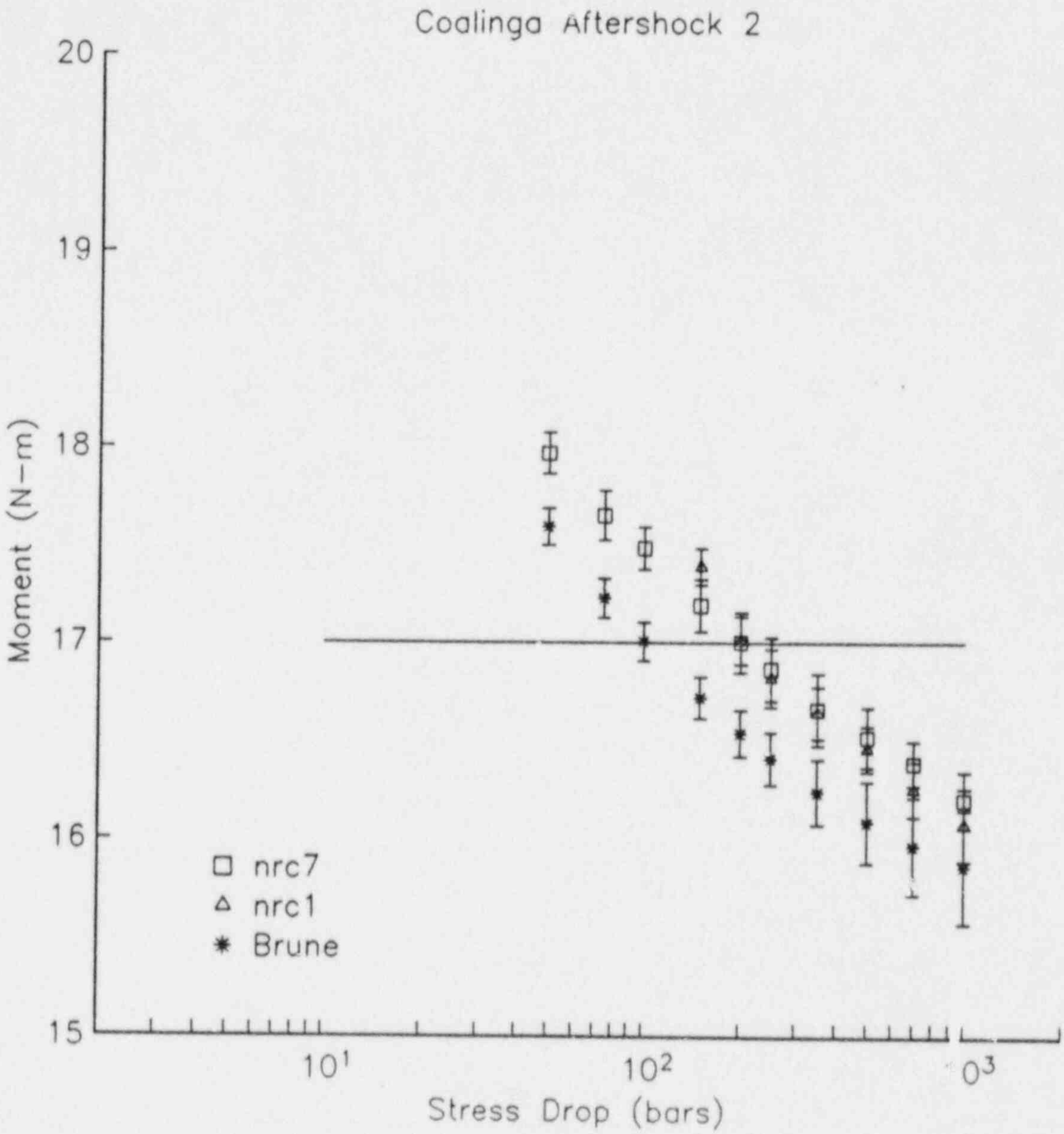

Figure 3.4. Estimated moment and stress drop for the May 9, 1983 Coalinga aftershock. The points on the plot are determined by finding a best fit comparison between the two numerical source models and a Brune source model in the 1 to 10 Hz frequency band. The horizontal line corresponds to the moment estimated from the moment-magnitude relation.

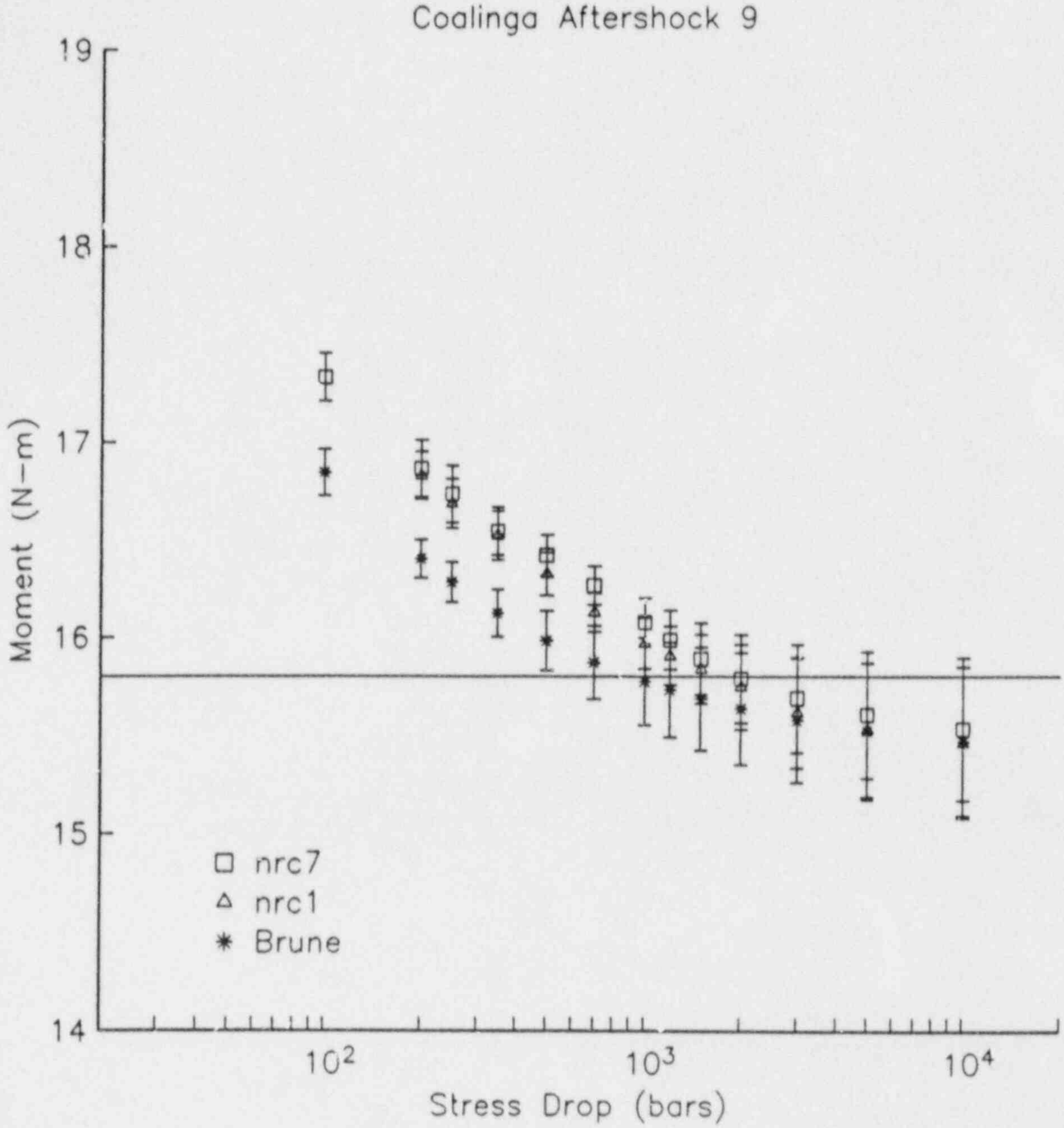

Figure 3.5. Estimated moment and stress drop for the September 11, 1983 Coalinga aftershock.

data fit is significantly better with a lower stress drop. This is because the corner frequency for this event is within the 1 to 10 Hz frequency band, and as show... .n Figure 3.6 the best fit solution with a 2 kilobar stress drop is too low at low frequencies (1 to 3 Hz) and too high at high frequencies (9 to 10 Hz). A much better result (Figure 3.6) is obtained with a stress drop of 500 bars and a moment of 2×10^{16} Newton-meters.

In Table 3.4, we list our best estimates of moment and stress drop for all of the aftershocks. These estimates were obtained using the numerical source models. The moment/stress drop curves for all events derived using source nrc7 are shown in Figure 3.7. In all cases, data fits with the two numerical sources gave the very similar estimates for stress drop. Stress drops range from 25 to 600 bars. The magnitude 6 event (Number 5), and the data fit for this event is shown in Figure 3.8. Again, the agreement is excellent for source NRC1 over the entire frequency band. Source NRC7, a complex source that had strong high frequency focusing in one direction, is larger than the empirical source for this event at the highest frequencies, as was the case for Event 2.

We conclude from this analysis of Coalinga events that the numerical source NRC1 is suitable as a subevent model, while NRC7 is anomalously rich in high frequency energy. This is not surprising, in that this source model was deliberately constructed to investigate potential effects of large, sharply delineated stress concentrations on seismic radiation. Comparable high-frequency effects are not present in the Coalinga aftershock data. As further support for the conclusion that NRC7 is not a representative subevent model, we made numerous attempts to simulate response spectra from large thrust events (1985 Michoacan, Mexico and 1985 Valparaiso, Chile) using NRC7 as a subevent. In every case, these simulations were disproportionately enriched in high frequencies compared to the recorded ground motion.

3.2.2 Simulation of July 22, 1983 Magnitude 6 Aftershock

In addition to validating the Green's function homogenization procedure and the subevent source model, the Coalinga earthquake sequence provides an opportunity to test the concept of approximating large events as summations of

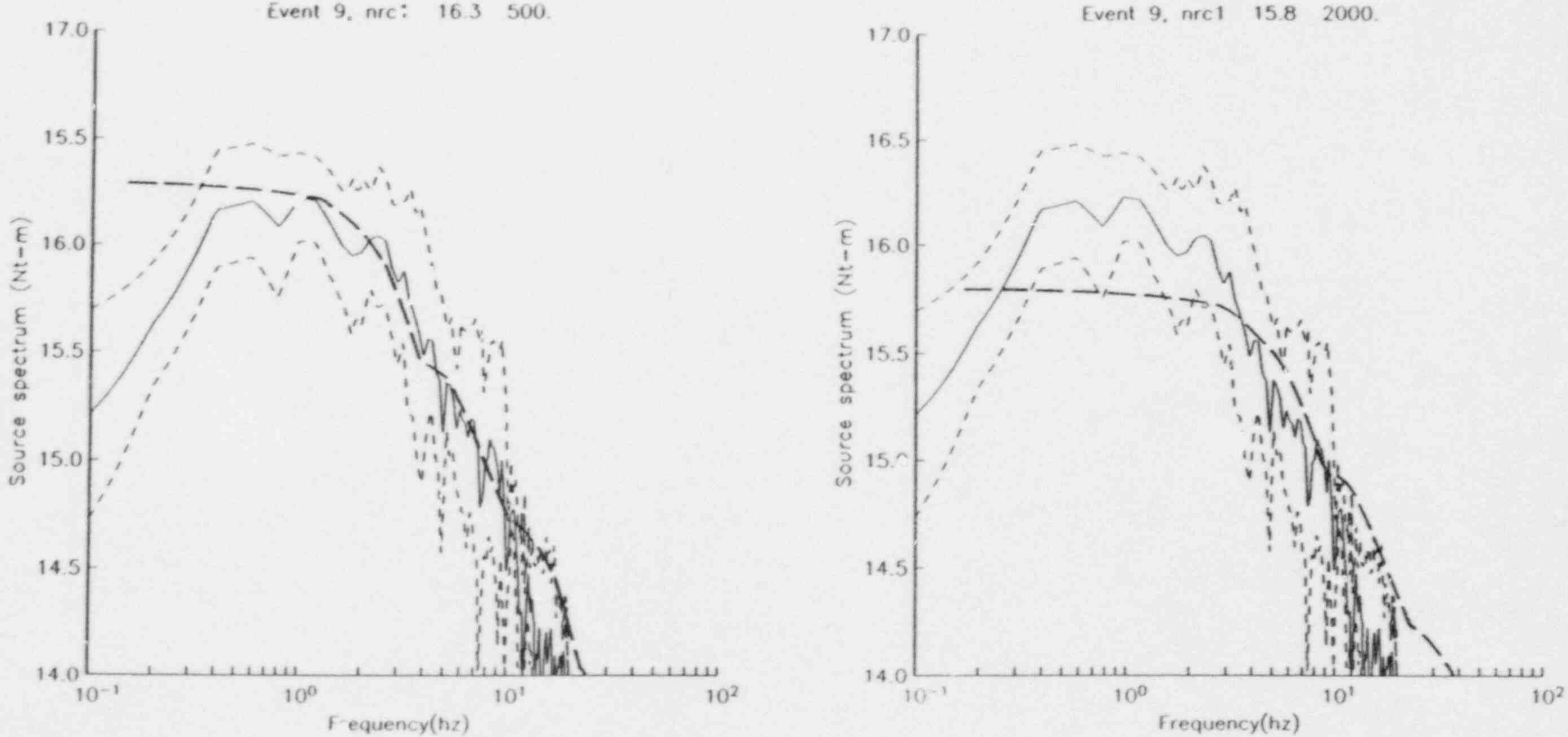

Figure 3.6. Best fit spectra for Event 9. The left figure shows numerical source spectrum nrc1 scaled to a 500 bar stress drop and a moment of 2×10^{16}. The right figure shows the numerical spectrum scaled to a 2 kilobar stress drop and a moment of 6×10^{15}.

TABLE 3.4

COALINGA AFTERSHOCKS
MOMENT, MAGNITUDE, STRESS DROP

Event	M_L	log M_0 (M_L)	log M_0	$\Delta\sigma$
2	5.3	17.0	17.00	200
3	5.2	16.85	16.85	350
4	5.4	17.15	17.15	80
5	6.0	18.05	18.05	400
6	5.0	16.55	16.55	80
7	5.3	17.0	17.00	600
8	5.3	17.0	16.40	25
9	4.5	15.8	16.30	500

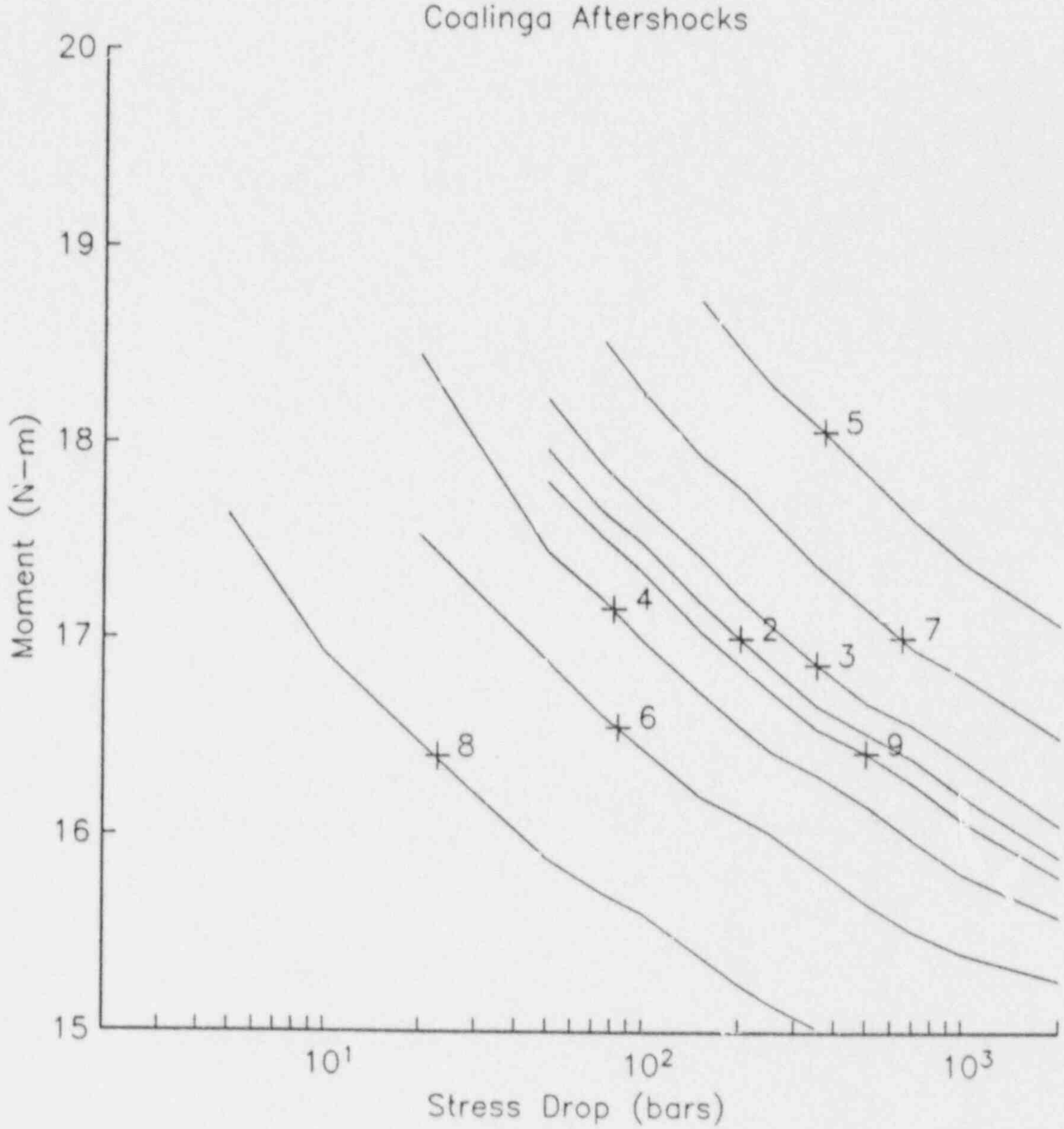

Figure 3.7. Moment and stress drops for all Coalinga aftershocks estimated using source nrc7. The + sign indicates the moment and stress drop selected for each event.

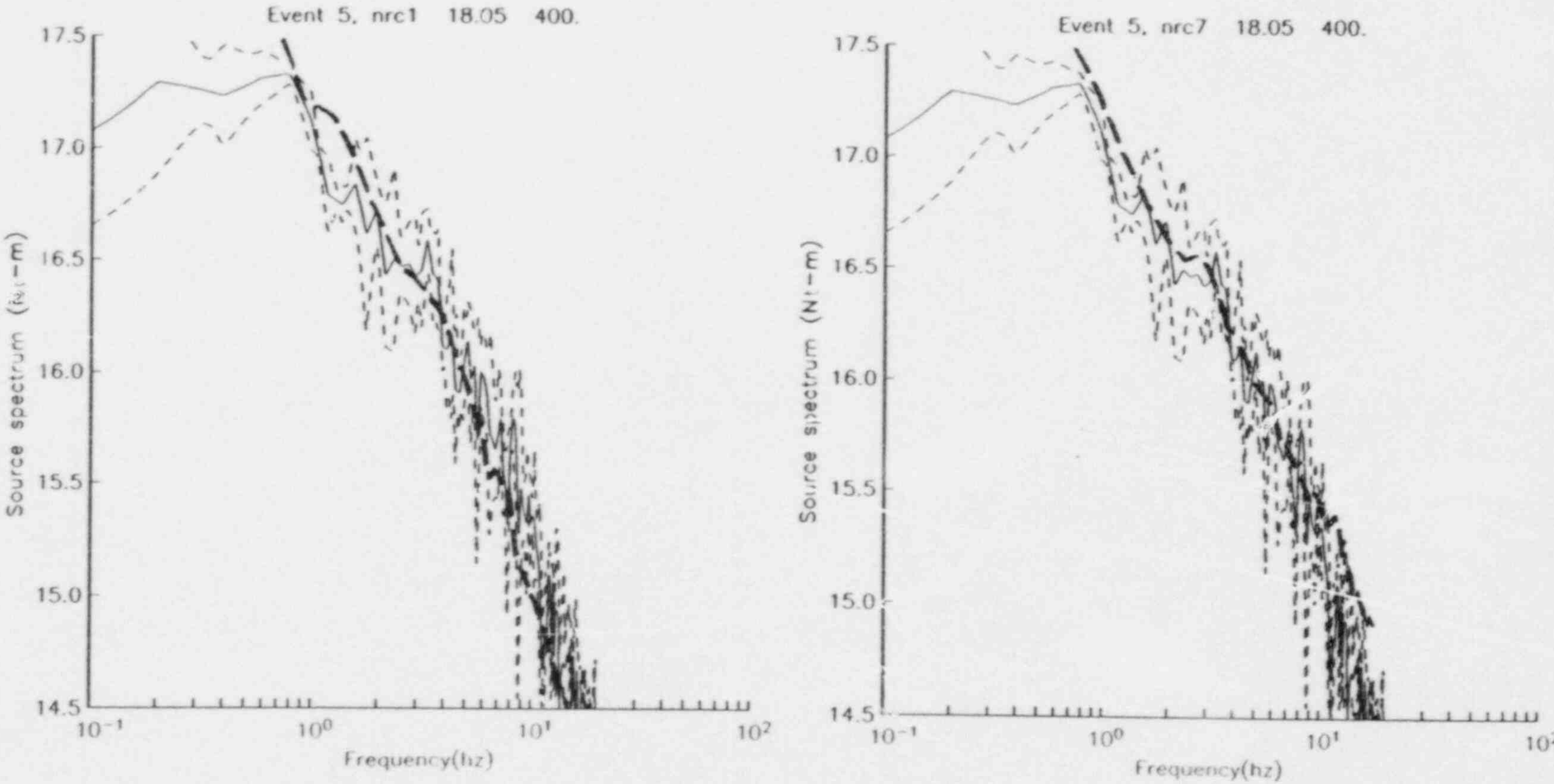

Figure 3.8. Average source spectrum of the July 22, 1983 aftershock (solid line) and ± 1 standard deviation (short dashed lines), together with the numerical source spectrum nrc1 (left) and nrc7 (right) (long dashed line) averaged over all takeoff angles and scaled to a moment of 10^{17} newton-meters and a stress drop of 200 bars.

subevents. The July 22, 1983 magnitude 6 aftershock was large enough to be modeled as a complex event using our summation procedure. We use the empirical source function derived from the magnitude 5.3 Event 2 recorded at California Division of Mines Station CHP as a subevent to model the magnitude 6 event recorded at the same station. Approximately 15 magnitude 5.3 subevents are required to be consistent with the moment of the magnitude 6 event. Since we do not know the geometry of the large event, we simulated it using a variety of subevent geometries ranging from a single source with 15 firings to 15 sources with a single firing each. The response spectra derived from these simulations are shown in Figure 3.9 together with the observed response spectrum from the magnitude 6 event.

The results are in very good agreement with the observations for all four simulations. This experiment demonstrates that our summation procedure can successfully reproduce the ground motion from a magnitude 6 earthquake consisting of approximately 15 subevents.

3.2.3 Simulation of the Magnitude 6.7 Coalinga Earthquake

The Coalinga main shock which occurred on May 2, 1983 was recorded at the Pleasant Valley Pump Station located approximately 10 km northeast of the epicenter. Uhrhammer, *et al.* (1983) estimate the dimensions of the fault as 15 km by 25 km. We simulate this event again using the May 9 aftershock (Event 2) as a subevent model. We use the empirical source function derived from the north-south component of the aftershock recording at USGS station SUB which was located close to the Pleasant Valley Pump Station. It requires an array of 7 by 11 subregions distributed over the 15 by 25 km area with two firings each to equal the moment of the main shock (based on the standard moment magnitude relation). We simulated the ground motion at SUB using one firing and two firings per subregion.

In Figure 3.10, we show the response spectra calculated from this simulation together with the observed response spectrum for this event. The observed response spectrum is the average of the response spectra recorded on the 45 degree and 135 degree instruments at the Pleasant Valley Pump Station (Borcherdt, 1983). The simulated response spectra agree very well in

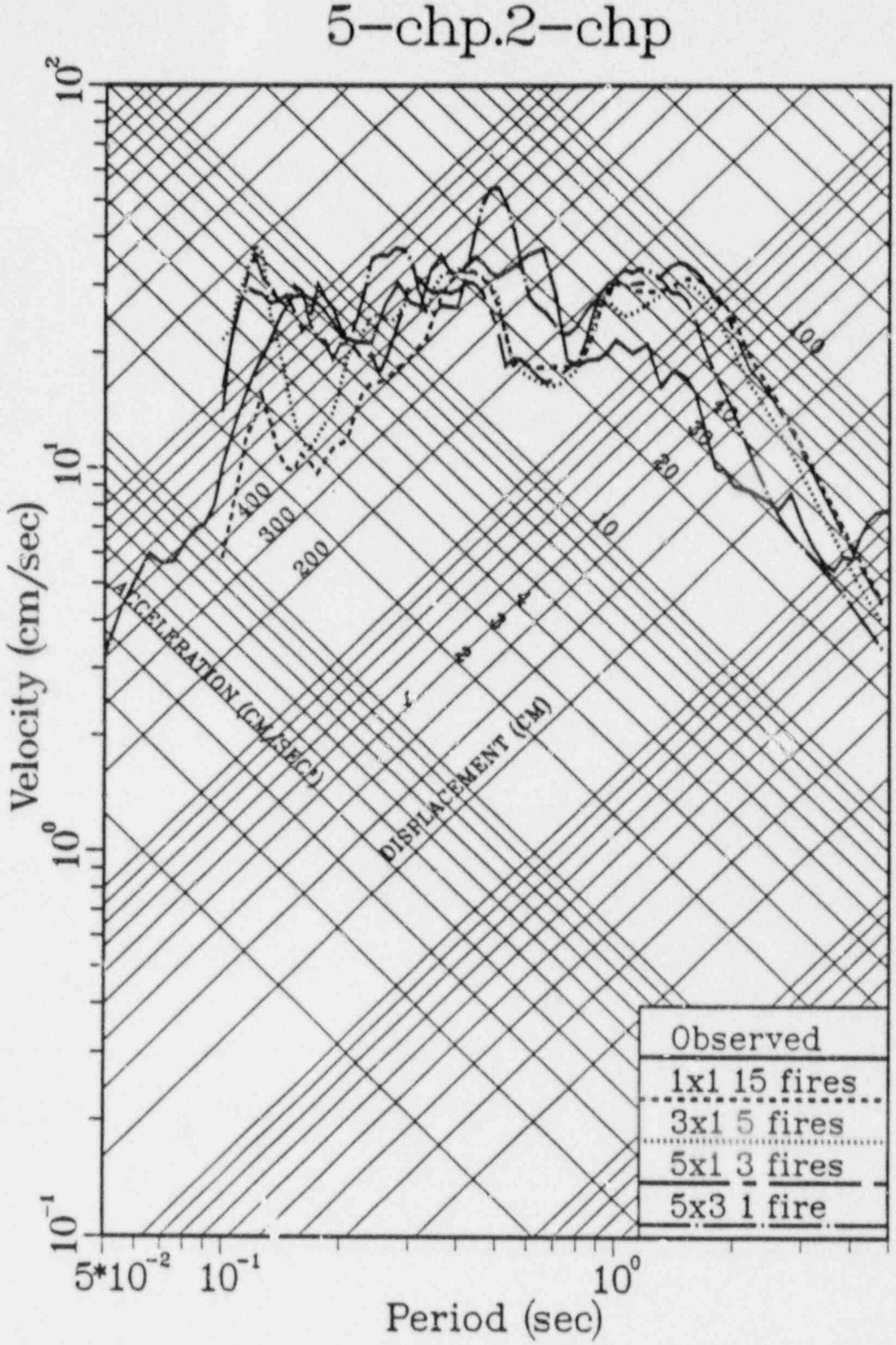

Figure 3.9. Simulated and observed response spectra for the July 22, 1983 magnitude 6 aftershock at Station CHP. The simulations were generated from 15 rays using source functions derived from the May 9, 1983 aftershock observed at this station.

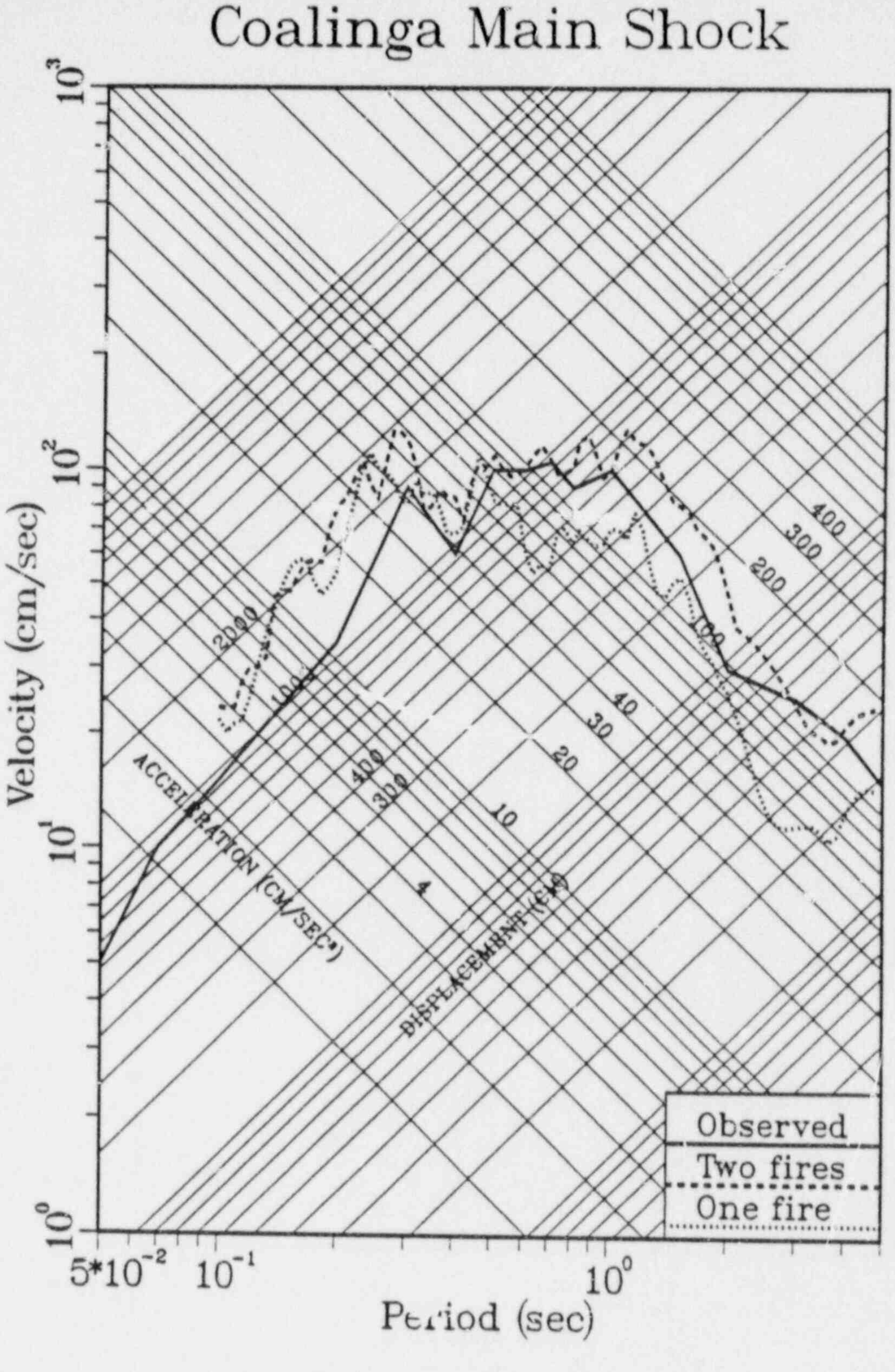

Figure 3.10. Simulated and observed response spectra for the Coalinga main shock at Station SUB using one and two fires per subregion over a 15 by 25 km area. The simulations were generated from 75 and 150 rays using the source function derived from the May 9, 1983 aftershock observed at this station. The solid line is the average of the two observed horizontal components.

both shape and amplitude with the observations, with the e. ception that the simulated response spectra are larger that the observed response spectra by slightly less than a factor of two between three and ten Hz. The simulation with two fires is a better match to the data in the 1 to 3 Hz frequency band.

This experiment demonstrates that the summation procedure can accurately predict the ground motion generated by an event two orders of magnitude larger than the subevent.

3.3 Comparison With 1985 Michoacan, Mexico Earthquake

The September 19, 1985 Michoacan, Mexico earthquake, of moment magnitude 8.1, was recorded by three accelerometer stations directly above the fault and one station just east of the fault. The ground motion data and fault characteristics are discussed by Anderson, *et al.* (1986). In this section, we show results of simulating the ground motion from this event, as recorded at Caleta de Campos, La Villita, Zihuatanejo, and La Union. This model test is particularly appropriate in that this event is probably the best instrumented large subduction zone thrust earthquake yet recorded. All four stations are on hard crystalline rock. These calculations exercises the earthquake model in a geometry very similar to that encountered in the WNP-3 sensitivity study, and as such constitute an important test of the model.

Figure 3.11 shows the geographic setting of the event, along with the corresponding earthquake geometry used in our test simulations. Figure 3.11a is taken from Anderson, *et al.*, and shows the aftershock zone, together with the epicenter and the locations of the three nearest recording stations. Fault parameters are derived from a set of recent papers in *Geophysical Research Letters*, (*UNAM*, 1986; Priestley and Masters, 1986; Ekström and Dziewonski, 1986; Riedesel, *et al.*, 1986; Eissler, *et al.*, 1986; Stolte, *et al.*, 1986). We use the following parameters for our simulation: Moment = 1.1×10^{21} Newton-meters; fault dip 12°; strike 293°; slip vector rake 76°. As shown in Figure 3.11b and c, we represent the event using a fault width of 50 km and a fault length of 170 km;

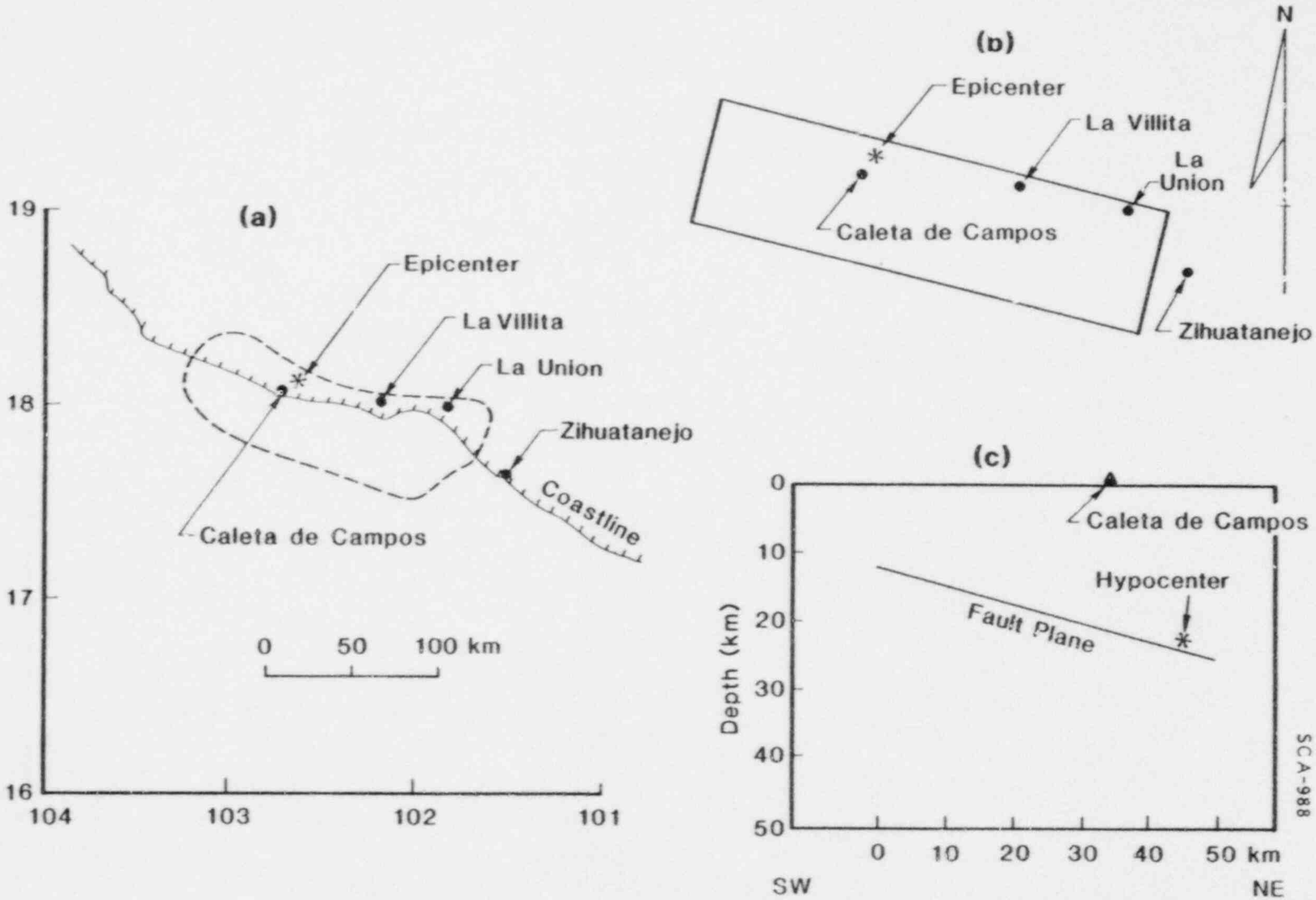

Figure 3.11. Epicenter and locations of accelerographs above the aftershock zone of the 19 September 1985 Mexico earthquake (after Anderson, *et al.*, 1986). The aftershock zone is outlined by the dashed curve. (b)The fault plane used in the simulation, projected onto a horizontal plane. (c) Cross-sectional view of fault geometry used in the simulation.

the long dimension of the rupture zone is slightly oblique to the strike direction, with a rake of 10°. The fault depth is constrained by S-P times on the Caleta de Campos accelerograms to approximately 20 km beneath that site. Table 3.5 shows the earth model used in the simulations. The P wave structure is from Havskov (1983), and S wave, density and Q profiles were estimated from the P wave values. The subevent model used in the simulations is the numerical source NRC1 with a local stress drop of 38 bars and a subevent dimension of 2.5 km, which corresponds to a moment magnitude of 5.7.

Using the seismic moment of 1.1×10^{21} Newton-meters and a fault width of 50 km, our Equation (2) implies a global stress drop of about 40 bars for this event. Using Equation 5, we can then determine the number of subevent slip episodes required to build up the appropriate static slip to correspond to the assumed moment. With $\Delta\tau_L$ equal to 100 bars the model overestimates the response spectrum at all frequencies. Figure 3.12 shows the north-south component response spectra at Caleta de Campos for simulations done with two values of $\Delta\tau_L$ (with all other parameters held fixed). Also shown are response spectra for the Caleta de Campos accelerograms from Prince, *et al.* (1985). For $\Delta\tau_L$ equal to 38 bars, the simulated ground motion is in excellent agreement with the data for periods above 0.5 seconds, and less than a factor of two high at shorter periods. For $\Delta\tau_L$ = 100 bars, on the other hand, the simulated response is a factor of 2 to 3 higher than the data for all periods. Very similar results are obtained at La Villita and La Union. In Figures 3.13 through 3.14 we show the response spectra calculated with $\Delta\tau_L$ equal to 100 and 38 bars, together with the observed response spectra at these stations.

In Figure 3.15, we show the observed Fourier acceleration spectra at Caleta de Campos, La Villita, and La Union, and the simulated spectra at these sites calculated with $\Delta\tau_L$ equal to 38 bars. The simulated spectra are an excellent match to the data at all three stations.

The close agreement of simulation and observation for $\Delta\tau_L$ equal to 38 bars leads us to compare the simulated accelerograms with the observed records for this case. The larger of the two horizontal acceleration components,

TABLE 3.5

EARTH MODEL FOR MEXICO EARTHQUAKE SIMULATION

Depth (km)	Thickness (km)	Compressional Velocity (km/sec)	Shear Velocity (km/sec)	Density (gm/cm^3)	Q
6.0	6.0	5.80	3.35	2.70	292
12.0	6.0	5.95	3.44	2.73	300
24.0	6.0	6.15	3.55	2.76	310
30.0	6.0	6.40	3.70	2.82	322
39.0	9.0	7.04	4.06	2.95	355
∞	∞	8.10	4.68	3.07	408

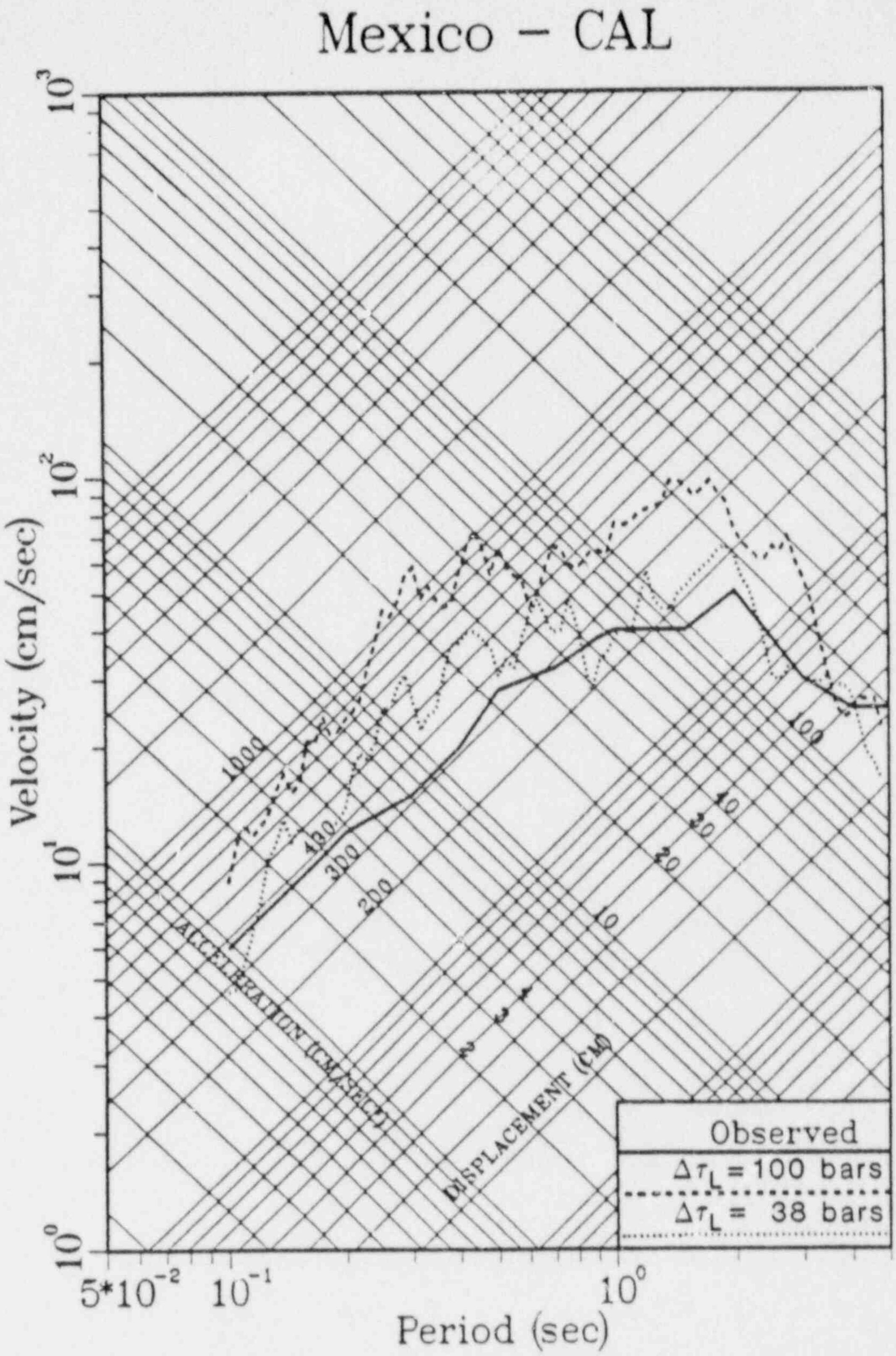

Figure 3.12. Response spectra for simulations of the N component, for two values of $\Delta\tau_L$, are compared to observations of the Mexico earthquake at Caleta de Campos (read from Figure 3a, Prince, *et al.*, 1985). Damping factor is five percent.

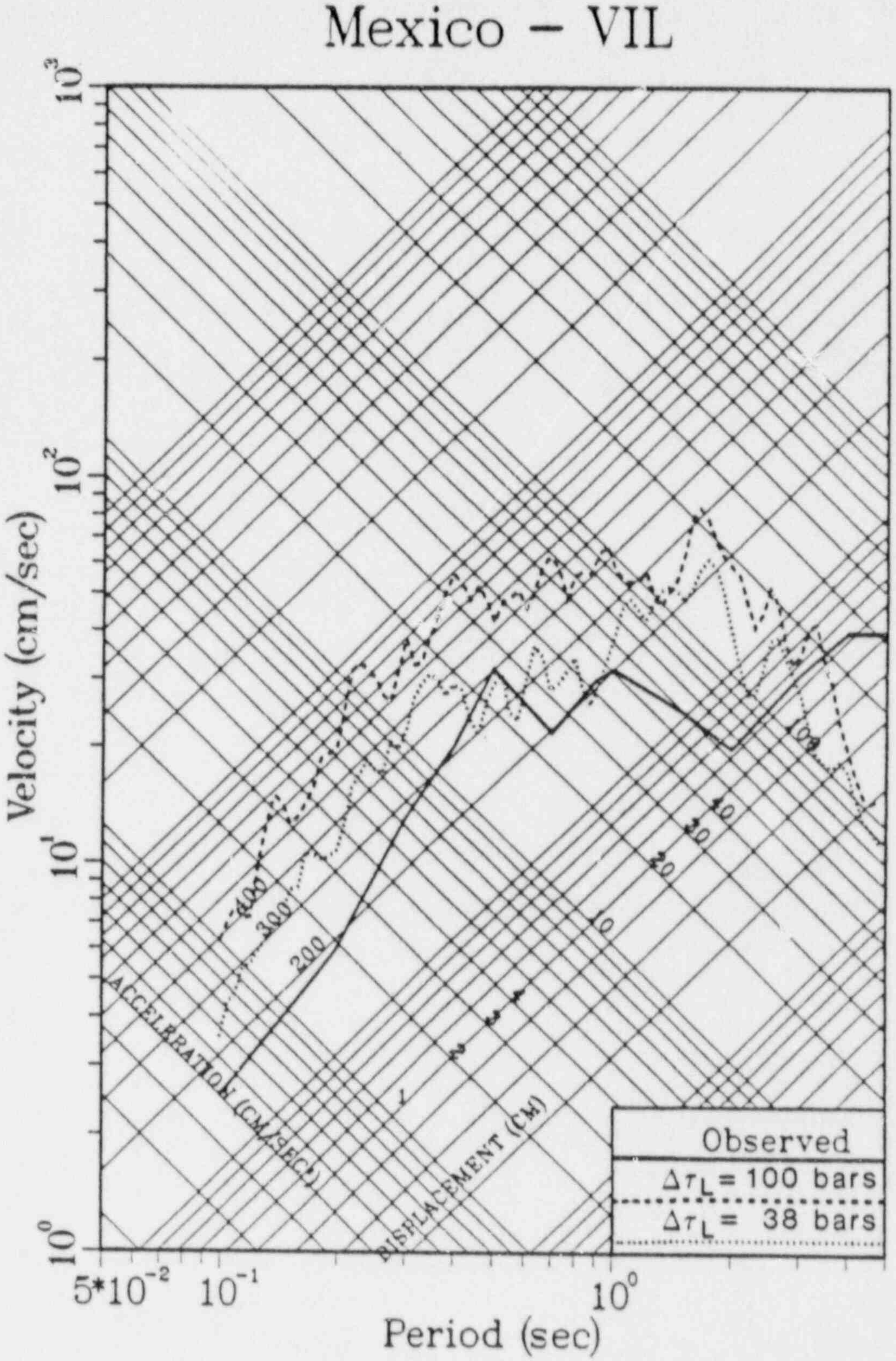

Figure 3.13. Response spectra for simulations of the north-south component at La Villita for two values of $\Delta\tau_L$. Also shown is the observed response spectrum at this site.

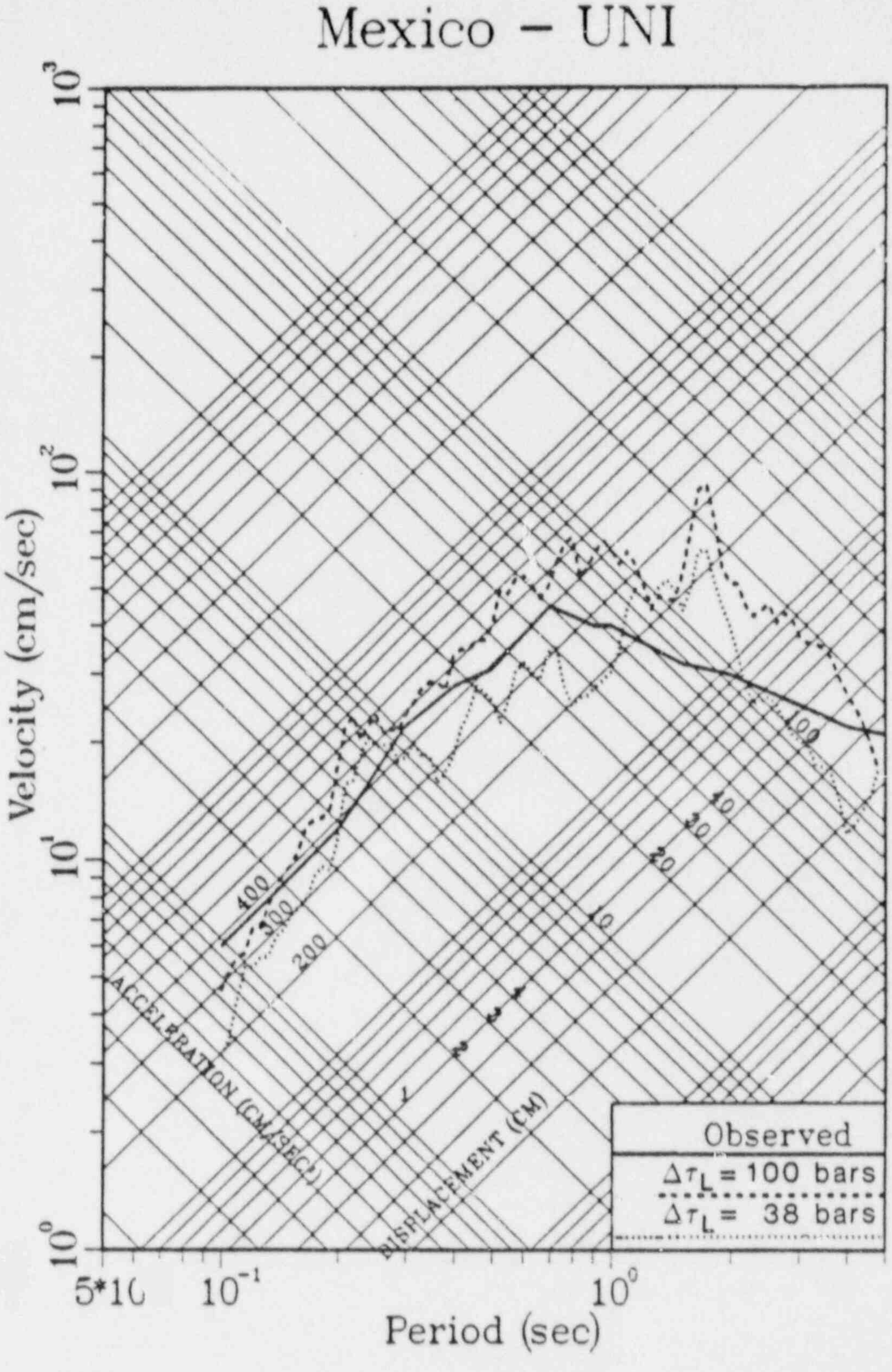

Figure 3.14. Response spectra for simulations of the north-south component at La Union for two values of $\Delta\tau_L$. Also shown is the observed response spectrum at this site.

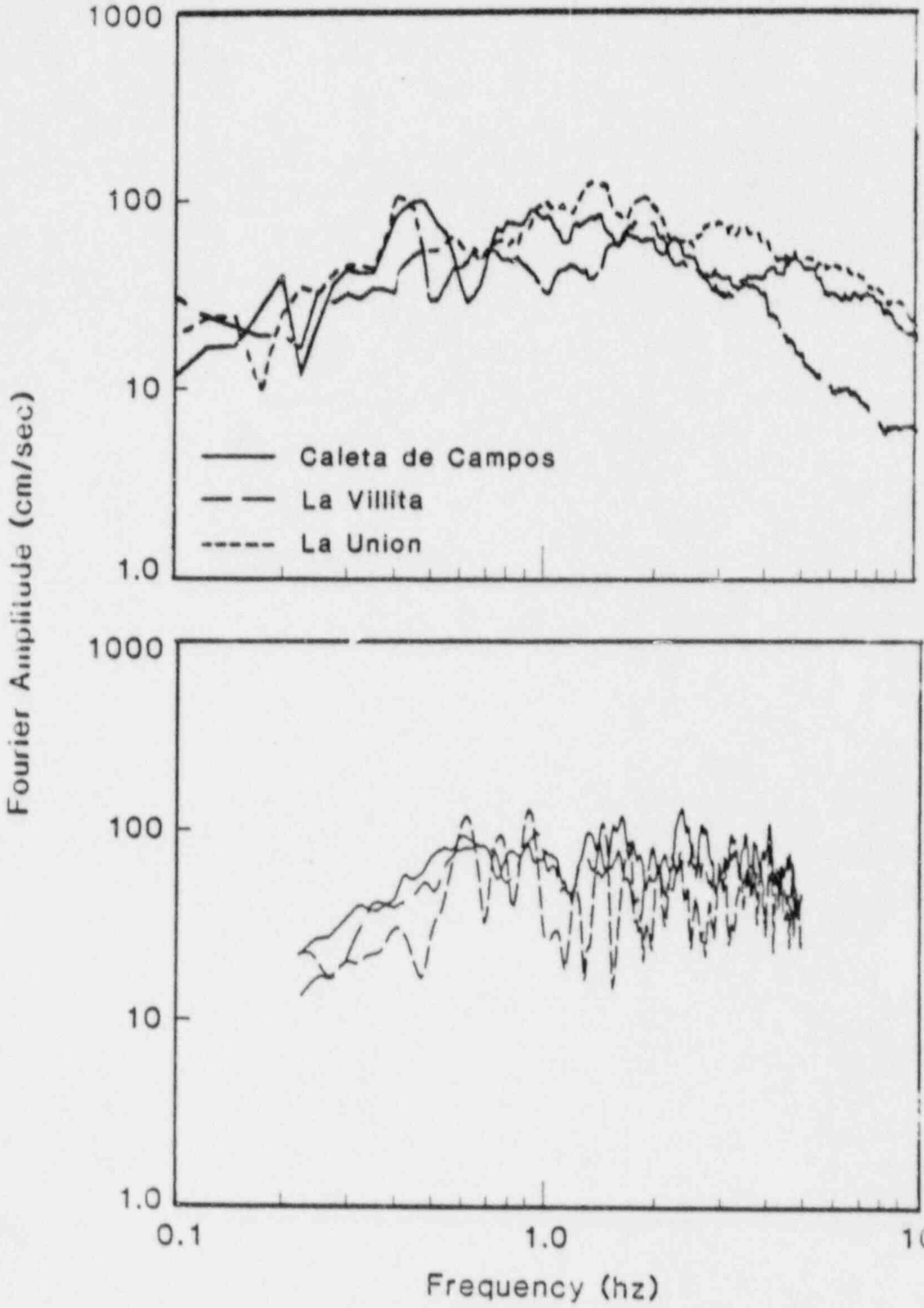

Figure 3.15. Observed and calculated Fourier acceleration spectra at Caleta de Campos (solid lines), La Villita (long dashes), and La Union (short dashes). The top figure shows the observed spectra; the bottom figure shows spectra calculated with $\Delta\tau_L$ equal to 38 bars.

the north component, is shown in Figure 3.16. The simulations are on top, the observed accelerograms are on the bottom. The agreement with these observations is excellent at all four stations. At Caleta de Campos, peak acceleration is overpredicted by about 20 percent. The overall character of the record is very well replicated in the simulation, and the predicted duration of the strong motion is similar to that observed. Similarly, at La Villita, the peak acceleration is over predicted by about 30 percent and the arrival times and duration of the record are reproduced very well. A secondary pulse arriving at about 55 seconds is due to a secondary rupture near the east end of the fault (this secondary rupture is discussed in several of the papers published in *Geophysical Research Letters*). At La Union and Zihuatenejo, the simulated accelerations match the data very well.

The choice of subevent size can also be constrained from the response spectra. As the equations and the analysis in the last chapter indicate the subevent size can affect both the low frequency and high frequency ground motion. In Figure 3.17, we show the predicted and observed response spectra at Caleta de Campos. The simulations were done with subevent dimensions of 2.5 km (corresponding to magnitude 5.7) and 1.25 km (magnitude 5.1). The simulation with the larger subevent is a much better fit to the data at both low and high frequencies.

These results demonstrate that the model can successfully represent the ground motion from a magnitude 8 earthquake in a geometry very similar to that of a hypothetical great earthquake in western Washington state. The results also serve to calibrate the model parameters a and $\Delta\tau_L$.

In the following section, we apply our model, with the constraints and modifications derived from the comparisons with observations in this chapter, to the prediction of ground motion at the WNP-3 site.

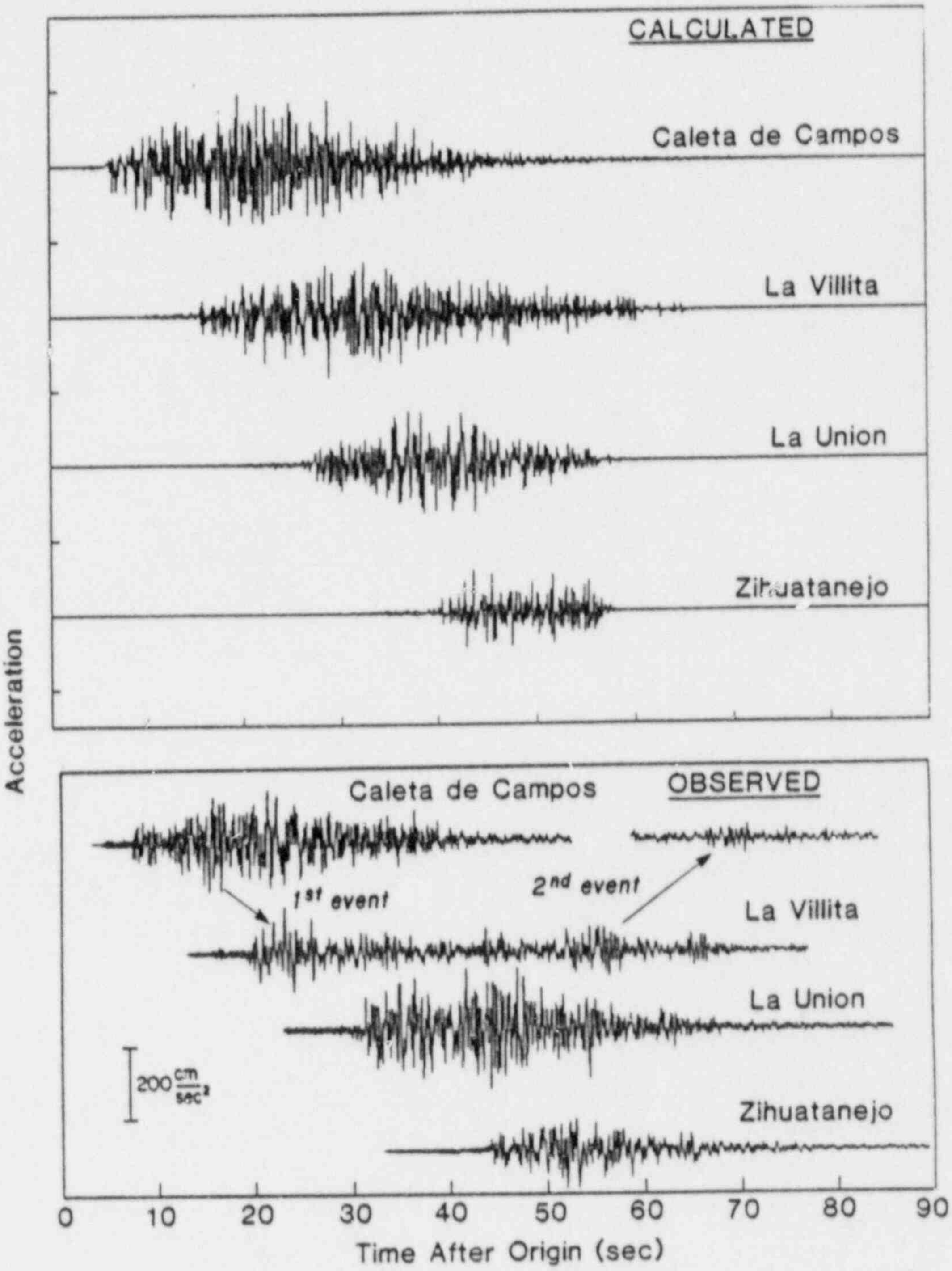

Figure 3.16. The north-south accelerograms recorded at Caleta de Campos, La Villita, La Union and Zihuatenejo (bottom four traces) are compared with simulated accelerograms ($\Delta\tau_L$ equal to 38 bars) at these four stations (top four traces). The recorded accelerograms are from Anderson, *et al.* (1986).

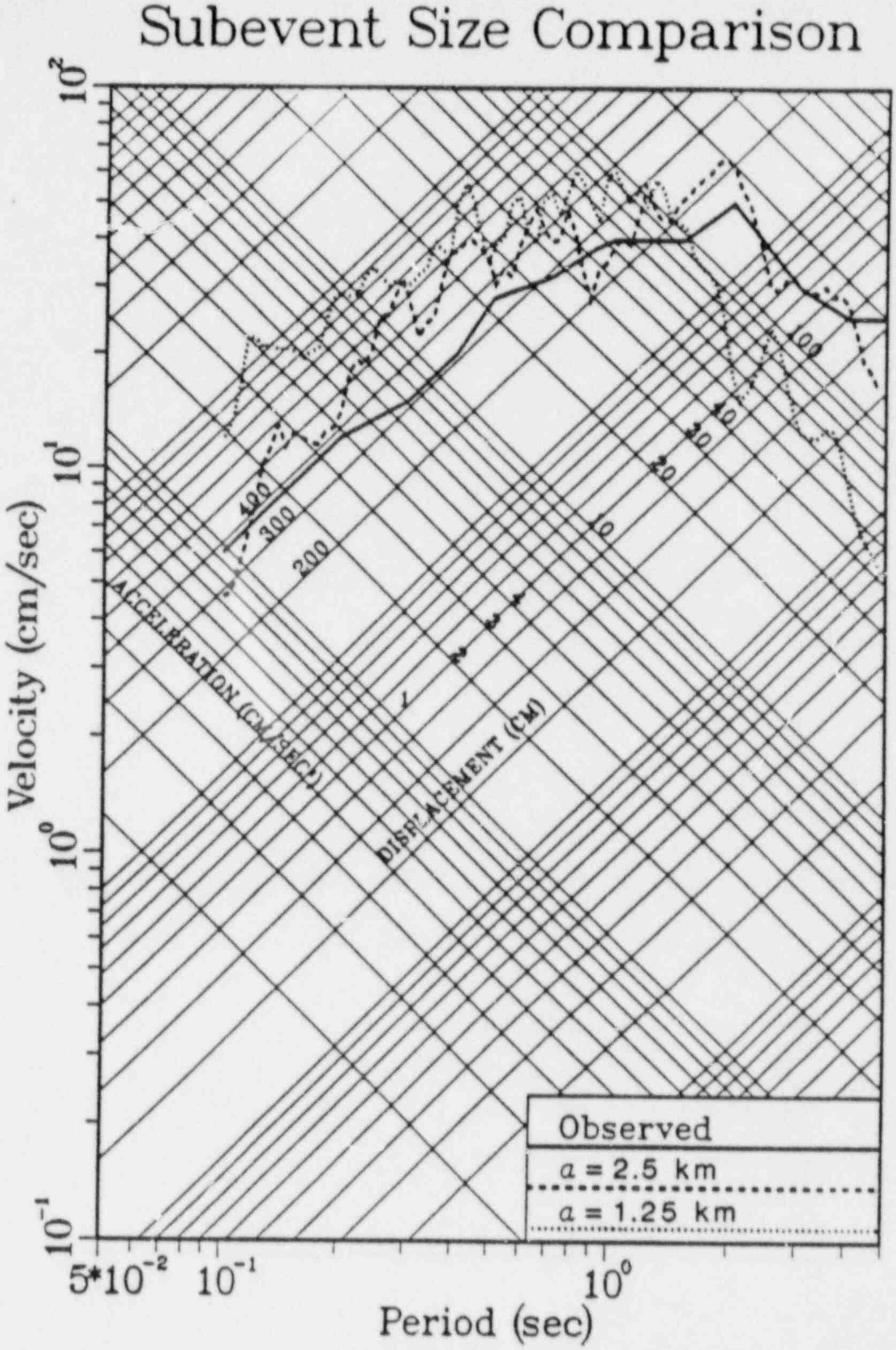

Figure 3.17. Simulated response spectra at Caleta de Campos using subevents of dimension 2.5 km and 1.25 km, respectively, with $\Delta\tau_L$ fixed at 38 bars. The larger subevent produces a better match to the data.

IV. SIMULATION OF GROUND MOTION AT WNP-3

4.1 Ground Motion Calculations

The anticipated ground motion at the WNP-3 site in the event of a large earthquake depends strongly on the fault location, and on the section of the fault that ruptures. Our approach to modeling the earthquake-induced ground motion at the WNP-3 site has been to simulate the ground motion for a set of parameters that cover the range of possible fault mechanisms near the site, and to identify "worst-case" situations. Throughout this section, the subevent model, local stress drop and subevent dimension have all been held fixed, as calibrated in Section 3.

The fault geometry used in this study is shown in Figures 4.1 and 4.2. The fault location is assumed to be known at a "hinge point" 185 km west of the WNP-3 site and to dip at a shallow angle between 9 and 20 degrees. Fault rupture is assumed to start at the base of the seismogenic zone and to propagate up the fault until it stops (at the final fault width) between the initiation point and the hinge point. Rupture can begin at any point on the fault, and continues at a prescribed rupture velocity until slip has occurred over a specified portion of the fault.

The most critical parameters for the prediction of ground motion are the fault width and the fault dip, which together control the nearest approach of the earthquake rupture to the site. The first part of this study is an examination of the effect of the variation of these parameters, with fault length, rupture velocity and stress drop held fixed (values used are listed in Table 4.1), using an earth model for the region from Crosson (1985), which is listed in Table 4.2. Two rupture geometries were used for each simulation (see Figure 4.2). In the first, rupture started at the closest point to the site on the intersection of the fault with the seismogenic zone. In the second case, rupture started at one corner of the fault and propagated toward the site.

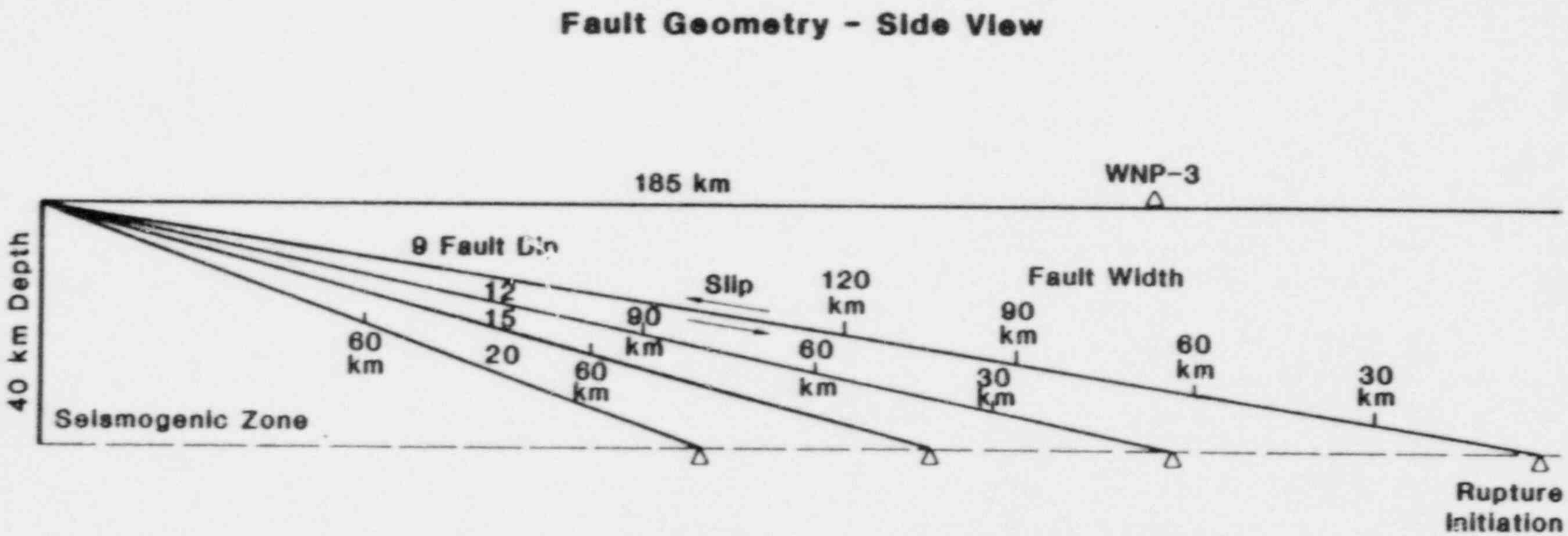

Figure 4.1. Side view of fault geometry. Rupture initiates at the base of the seismogenic zone and propagates up dip toward the "hinge point" 185 km to the west of the WNP-3 site.

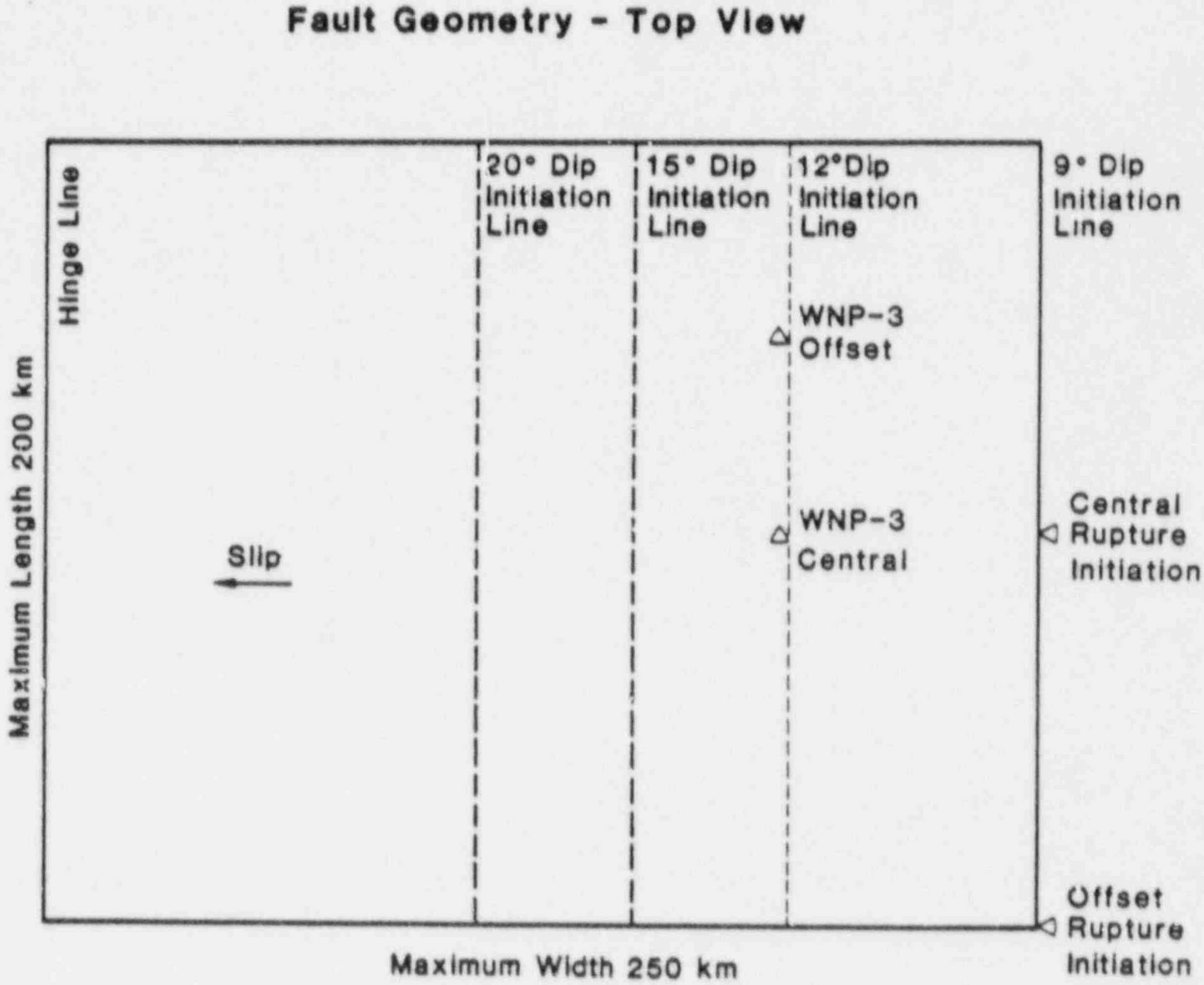

SCA-992

Figure 4.2. Top view of fault geometry. In the ground motion simulations, rupture always initiates at 40 km depth, but may occur at the closest point to the site (marked central), or away from the site (marked offset).

TABLE 4.1

PARAMETERS FOR GROUND MOTION SIMULATION

Fault Dip	9 to 20 Degrees
Fault Width	30 to 240 km
Fault Length	200 km
Global Stress Drop	40 Bars
Local Stress Drop	38 Bars
Subevent Radius	2.5 km
Rupture Initiation	Central and Offset
Rupture Velocity	3 km/sec

TABLE 4.2

EARTH STRUCTURE (Crosson, 1985)

Depth (km)	Thickness (km)	Compressional Velocity (km/sec)	Shear Velocity (km/sec)	Density (gm/cm^3)	Q
4	4	5.4	3.1	2.7	310
9	5	6.4	3.7	2.7	370
20	11	6.9	4.0	2.7	400
∞	∞	7.8	4.5	2.7	450

Synthetic seismograms and 5 percent damped response spectra were calculated for dips of 9, 12, 15 and 20 degrees, and fault widths ranging from 30 to 240 km. The response spectra at three frequencies and the peak velocities and accelerations are listed in Table 4.3, and plots of all calculated response spectra are in Appendix D. The peak accelerations and peak velocities listed in the table are averages of the two horizontal components for the two simulations with central and offset initiation points. As can be seen from Figure 4.1, the shallowest dip angles bring the fault much closer to the WNP-3 site than the steeper dip angles, and because of this difference significantly larger ground motions are predicted for dips of 9 and 12 degrees than for the other cases. In Figures 4.3 and 4.4, we show "worst case" response spectra for the two rupture initiation points and for the largest possible earthquake at each dip angle. In the case of the 9 degree dip angle, this represents a very large earthquake, with a moment magnitude of 8.8, rupturing an area 200 km by 240 km and passing approximately 30 km below WNP-3. The 9 degree simulations fall very close to the SSE spectrum for these large earthquakes. The response spectra for simulations of the 12 degree dipping fault in no case exceed the SSE. The response spectra for the 15 degree and 20 degree dipping faults are well below the SSE spectrum even for the largest possible rupture on these faults. In Figures 4.5 and 4.6, we show the calculated response spectra for a fault width of 90 km for each dip angle. This corresponds to a moment magnitude of 8.3 if the fault ruptures over the entire 200 km length of the fault. The response spectrurn for the 9 degree fault is everywhere below the SSE spectrum with its nearest approach occurring near 0.2 seconds period. The response spectra for the more steeply dipping faults are everywhere a factor of 2 or more below the SSE spectrum.

4.2 Discussion

The predicted ground motion is very insensitive to fault length. As a result, somewhat smaller magnitude earthquakes could give the ground motion shown in Figures 4.3 to 4.6 if rupture occurred on only part of the fault. In Figure 4.7, we show the response spectra predicted at the WNP-3 site, with the fault

TABLE 4.3

RESULTS OF GROUND MOTION SIMULATION FOR WNP-3 SITE

Fault Dip (deg)	Fault Width (km)	Moment Magnitude	5% Damped PSRV (cm/sec) 0.2 sec	0.4 sec	1.0 sec	Peak Acceleration (cm/sec^2)	Peak Velocity (cm/sec)
9	30	7.74	9	12	8	65	5
9	60	8.14	25	30	25	165	15
9	90	8.32	25	30	50	250	20
9	120	8.50	25	40	50	280	22
9	150	8.64	30	50	60	320	25
9	240	8.86	30	50	80	330	30
12	30	7.74	9	12	20	85	9
12	60	8.14	10	20	25	150	12
12	90	8.32	12	30	40	150	15
12	120	8.50	12	30	50	160	16
12	150	8.64	12	30	50	165	18
15	60	8.14	6	10	10	70	6
15	90	8.32	7	12	12	70	6
15	120	8.50	8	15	12	80	7
20	60	8.14	2	4	2	20	2
20	90	8.32	2	4	3	20	2

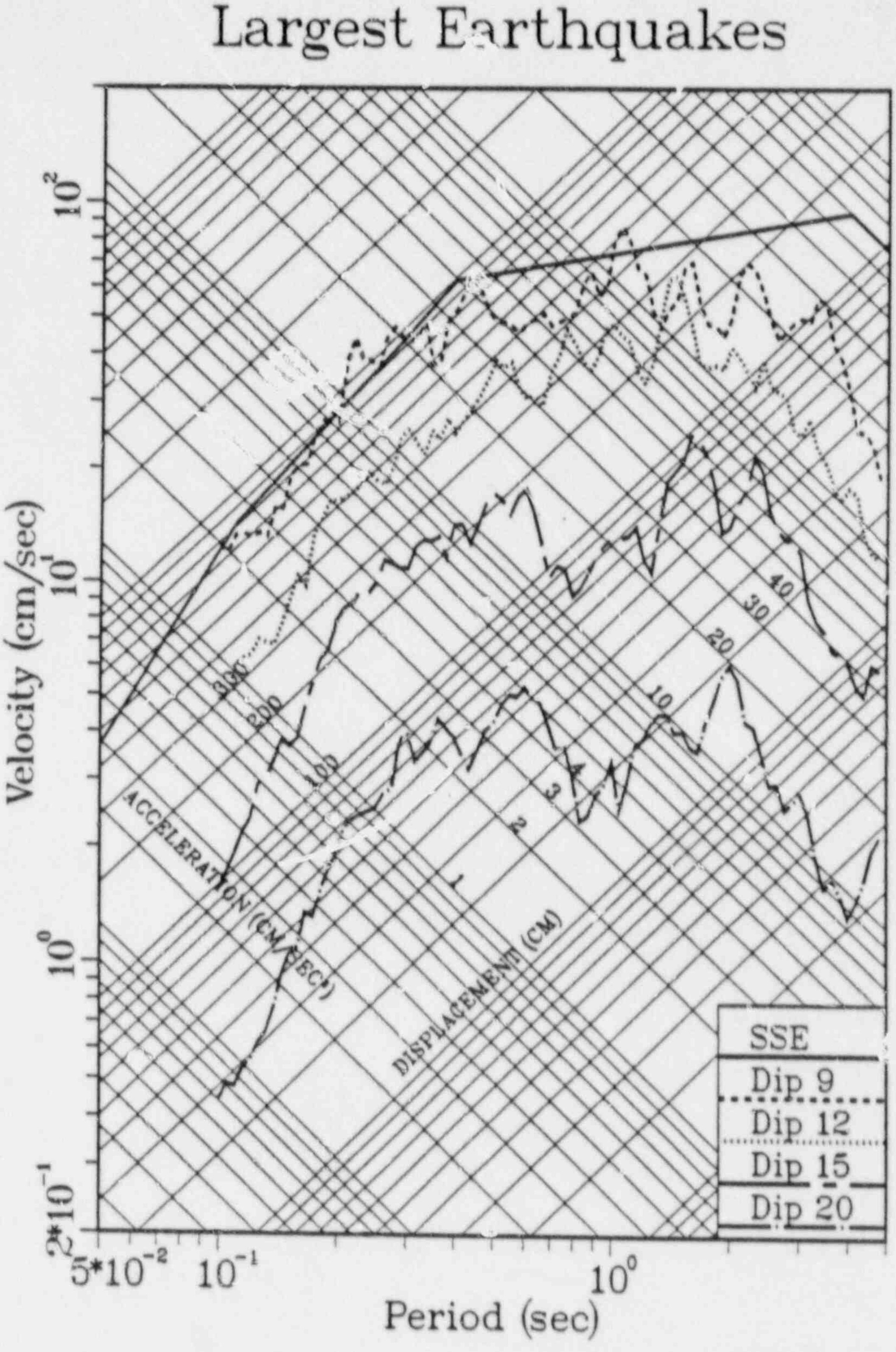

Figure 4.3. Predicted 5 percent damped response spectra for "worst case" earthquakes at dip angles of 9°, 12°, 15° and 20° with central rupture initiation. Solid line on this and other response spectra plots in this report is the SSE curve for the WNP-3 site.

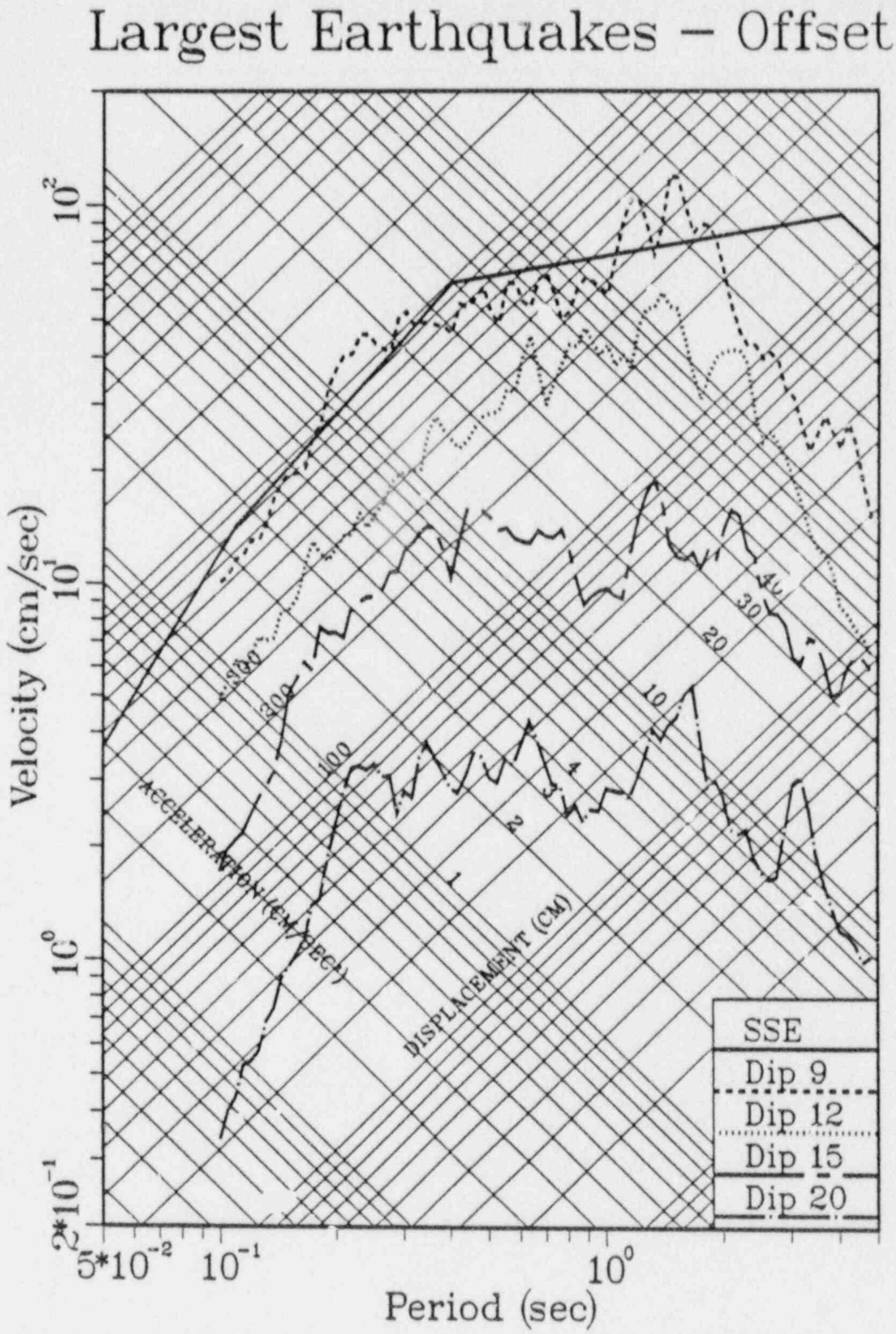

Figure 4.4. Predicted 5 percent damped response spectra for "worst case" earthquakes at dip angles of 9°, 12°, 15° and 20° with offset rupture initiation.

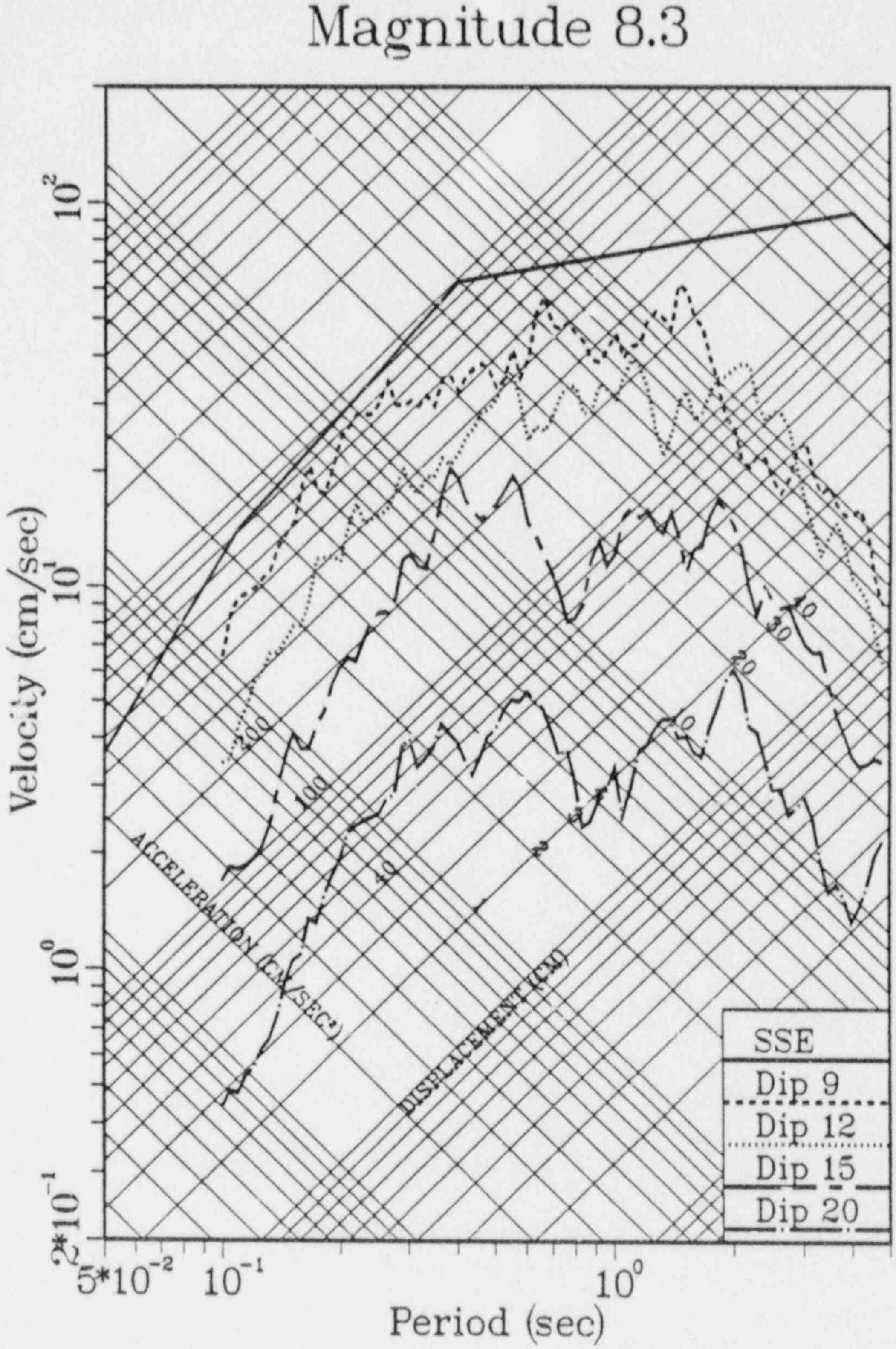

Figure 4.5. Predicted response spectra for fault width of 90 km (M_W = 8.3), for dip angles of 9°, 12°, 15° and 20° with central rupture initiation.

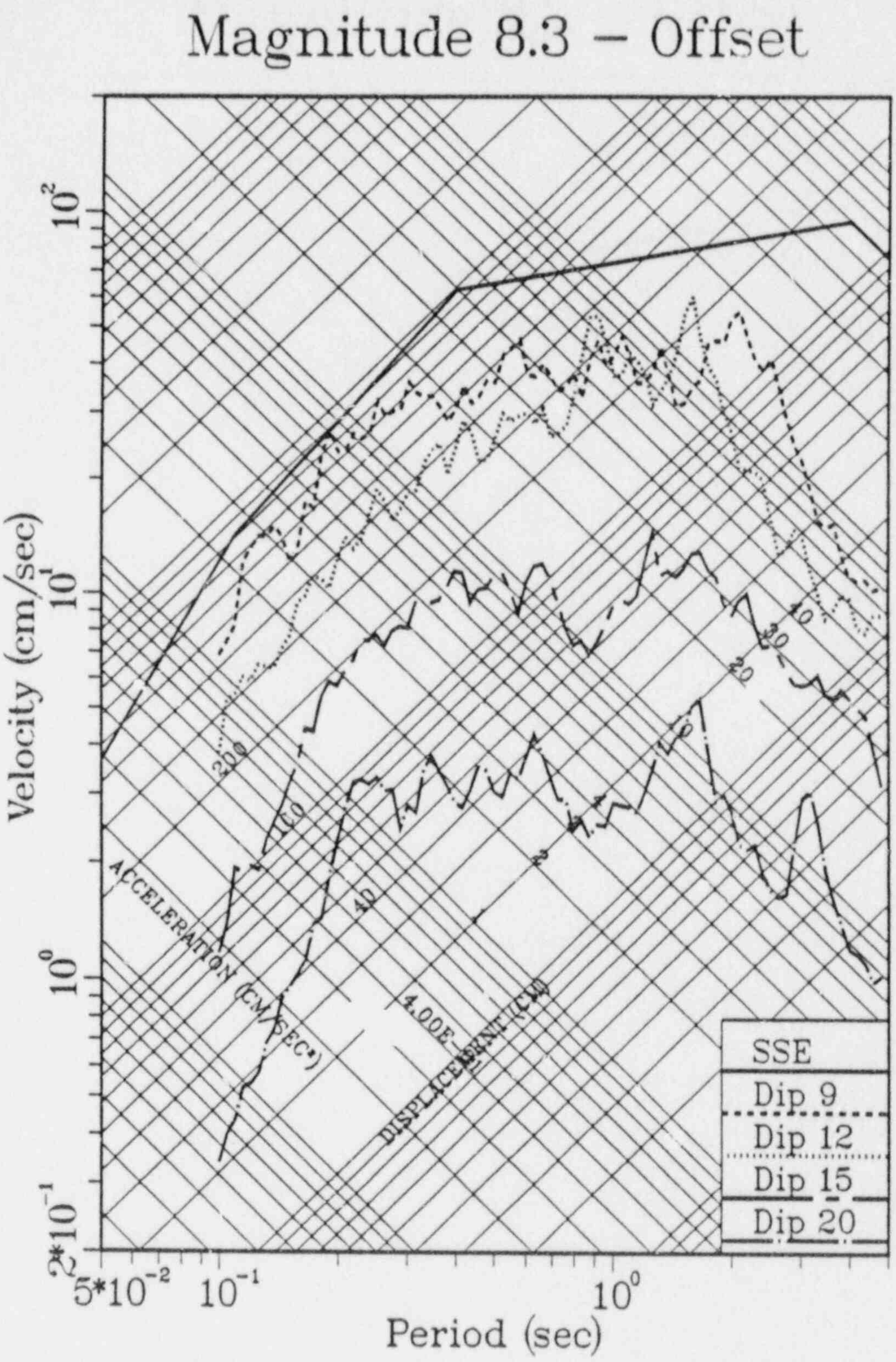

Figure 4.6. Predicted response spectra for fault width of 90 km (M_W = 8.3), for dip angles of 9°, 12°, 15° and 20° with offset rupture initiation.

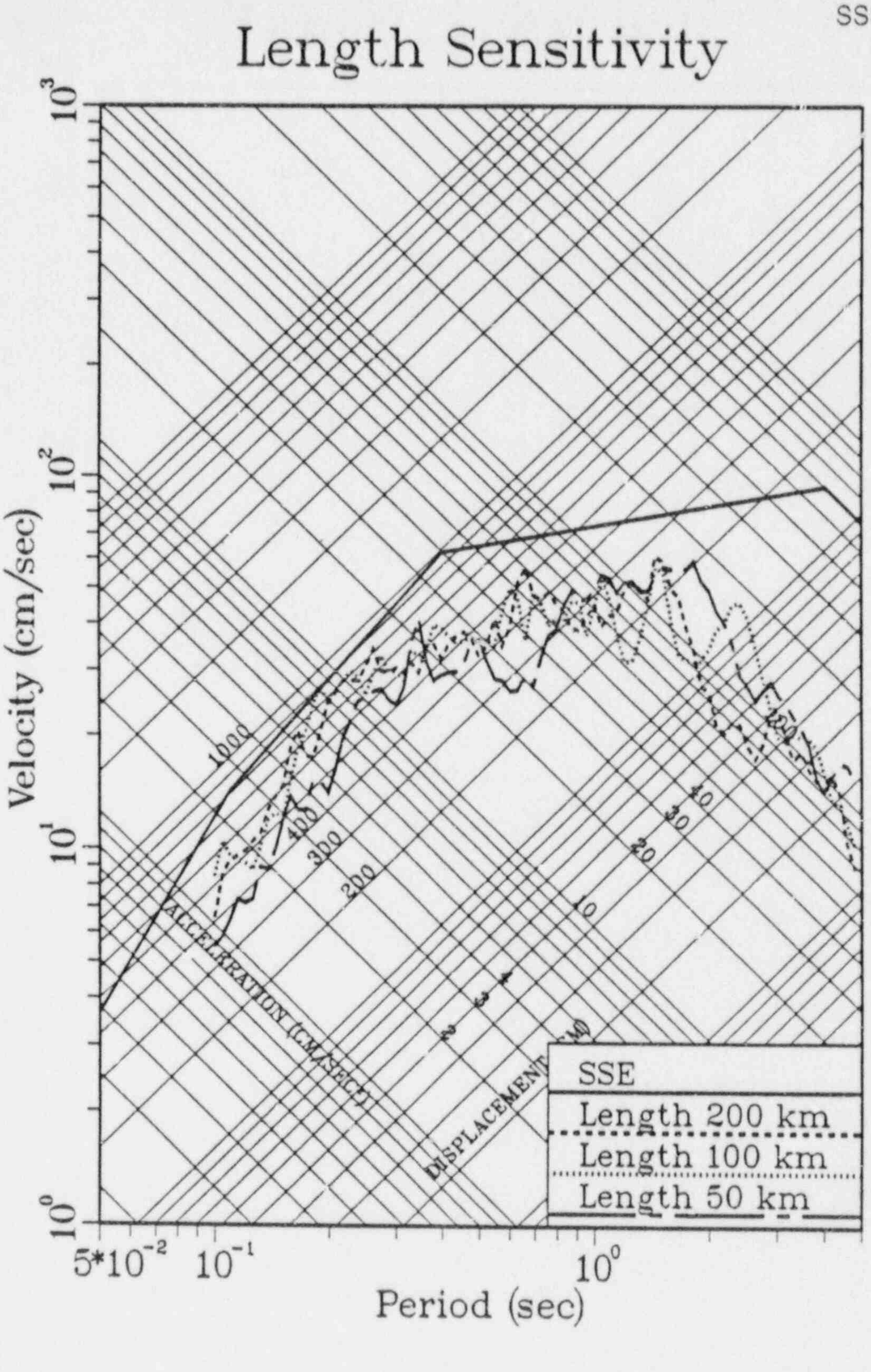

Figure 4.7. Response spectra are very insensitive to fault length. These response spectra were calculated for fault lengths of 200 km, 100 km, and 50 km. All three calculations were for a fault width of 90 km and a dip of 9 degrees. The moment magnitudes corresponding to these three cases are 8.32, 8.12 and 7.92, respectively.

length reduced to 100 km and 50 km. The fault width is 90 km and the dip is 9 degrees with central rupture initiation in both cases. There is no difference between the response spectra produced by the 200 km fault and the 100 km fault, although the magnitude of the 100 km event is reduced from 8.3 to 8.1. With the fault length reduced to 50 km, which reduces the magnitude to 7.9, the predicted response spectrum is reduced somewhat.

Several factors, such as the location of rupture initiation and variations in stress drop, earth structure, and attenuation could affect the predictions of the last section, and we have done a number of tests to try to estimate the uncertainty that variations in these factors introduce into our predictions. As can be seen in Figures 4.3 through 4.6, the results are very insensitive to the rupture initiation point. There is very little difference between the results with the central and offset rupture initiation point.

Variations in Q structure have little effect on the closer, higher amplitude cases, at the critical period range of 0.2 to 0.3 seconds, but may affect the results in the more distant cases. The Q structure in our model was determined from the generic relation $Q = 100\,\beta$, where β is the shear velocity in km/sec. To test the effect of variations in Q we did two test cases, one with Q increased to $200\,\beta$ and one with Q decreased to $50\,\beta$. In both cases the fault dip was 20 degrees and the fault width was 60 km, so the closest point on the fault was about 90 km from the receiver. The results are shown in Figure 4.8. There is little difference at lower frequencies (below 2 to 3 Hz) and about a factor of 2 increase (decrease) in amplitude in the 2 to 10 Hz frequency band for the increased (decreased) Q test case. The response spectrum is still well below the SSE for the higher Q case.

For periods lower than about 0.2 seconds, the Q model $100\,\beta$ may well be unrealistically low, in so far as it represents whole-path attenuation. However, Anderson and Hough (1984) have shown that accelerogram Fourier spectra also evidence an apparently path length-independent component of attenuation which can be represented in the same form as the whole-path component, i.e., $e^{-\pi\kappa f}$. For the 1971 San Fernando earthquake accelerograms recorded on rock,

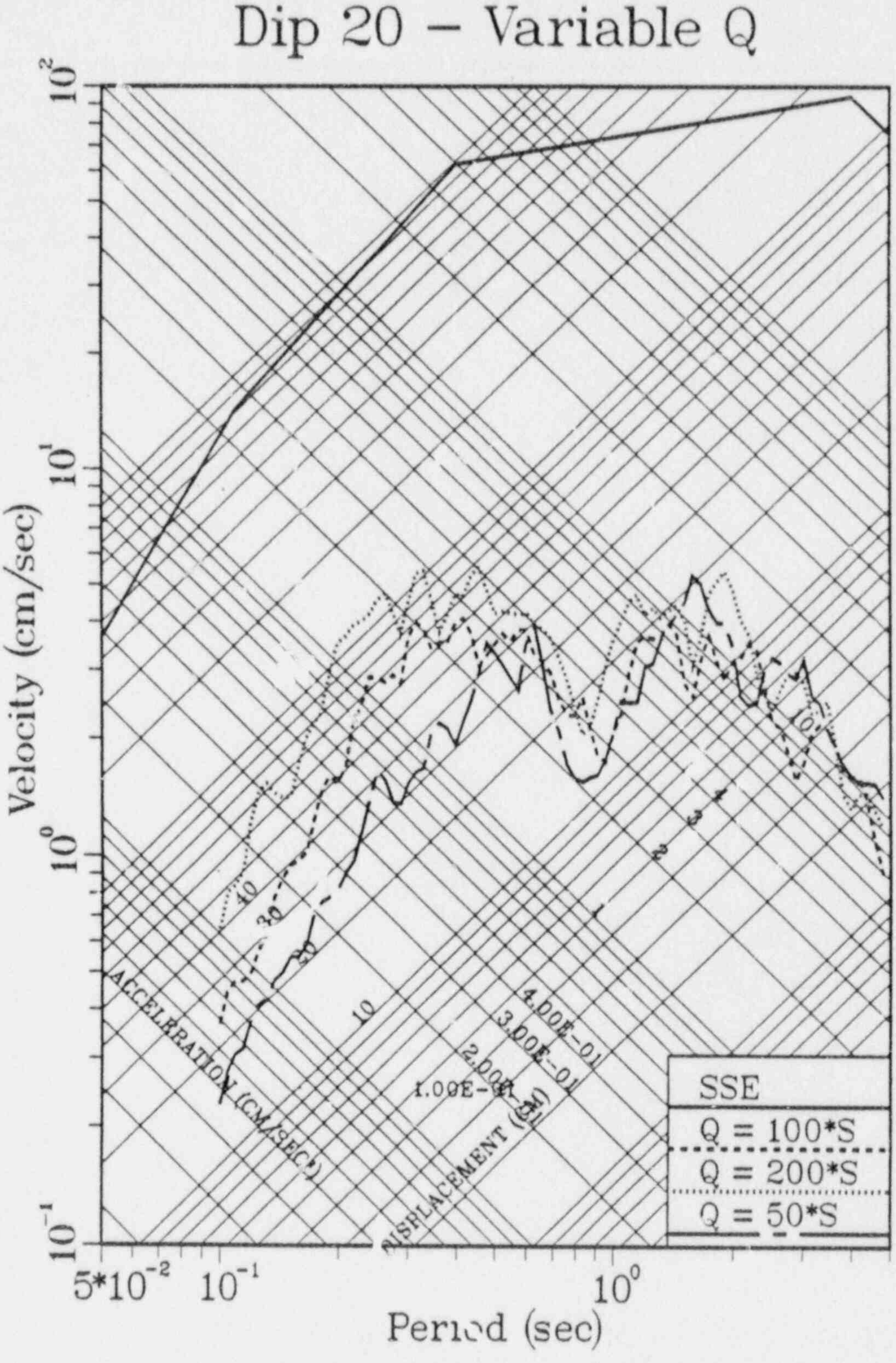

Figure 4.8. This figure shows response spectra variations caused by variations in attenuation. Shown are 20 degree dip, 60 km wide fault simulations with Q equal to 100 times the shear velocity (in km/sec), 200 times the shear velocity, and 50 times the shear velocity.

they found κ equal to approximately 0.04 sec. This corresponds to the shear wave attenuation coefficient obtained from the whole-path attenuation model used here (with $Q = 100\ \beta$) at a distance of approximately 50 km. Thus, for the 9 to 12 degree dipping faults, the attenuation model is expected to be relatively conservative at 0.1 seconds period. For the more distant faults, the Q model may be somewhat too attenuative below about 0.2 seconds period.

Variations in earth structure can affect our results in two ways depending on the location of the fault. If there is a shallow low-velocity surface layer, it can have the effect of amplifying the ground motion for rays at near-vertical incidence. We do not address this case, since the WNP-3 site is located on hard rock. On the other hand, layered earth structure can cause rays from more distant sources to be reflected away from the surface. As we pointed out in the last section, observation indicates that more energy reaches the surface than is predicted by ray theory for these cases.

To test for the effect of unrealistic amplitude reduction at grazing angles of incidence, we did two calculations in a 6.4 km/sec half space. The first test case was the magnitude 8.8, 9 degree dip, 240 km wide fault. There was no significant change in the results for this case. The second test case was the 20 degree dip, 60 km wide case. This was the case with the shallowest angle of incidence. When the Crosson structure was replaced with a half space, the amplitudes increased by about a factor of 2.

In addition, we examined the effect of adding additional rays to the primary S-wave. The effect was invariably negligible for the 9 and 12 degree dipping faults. The maximum effect was for the 20 dipping fault, which experienced approximately a 50 percent increase in response spectral amplitudes.

As can be seen from Equation 5, a change in the global stress drop (i.e., average fault slip divided by fault dimension) implies a proportional change in the number of slip episodes, N, for each subregion. In Figures 4.9 and 4.10, we show a set of results for the 60 km wide and 90 km wide faults with the

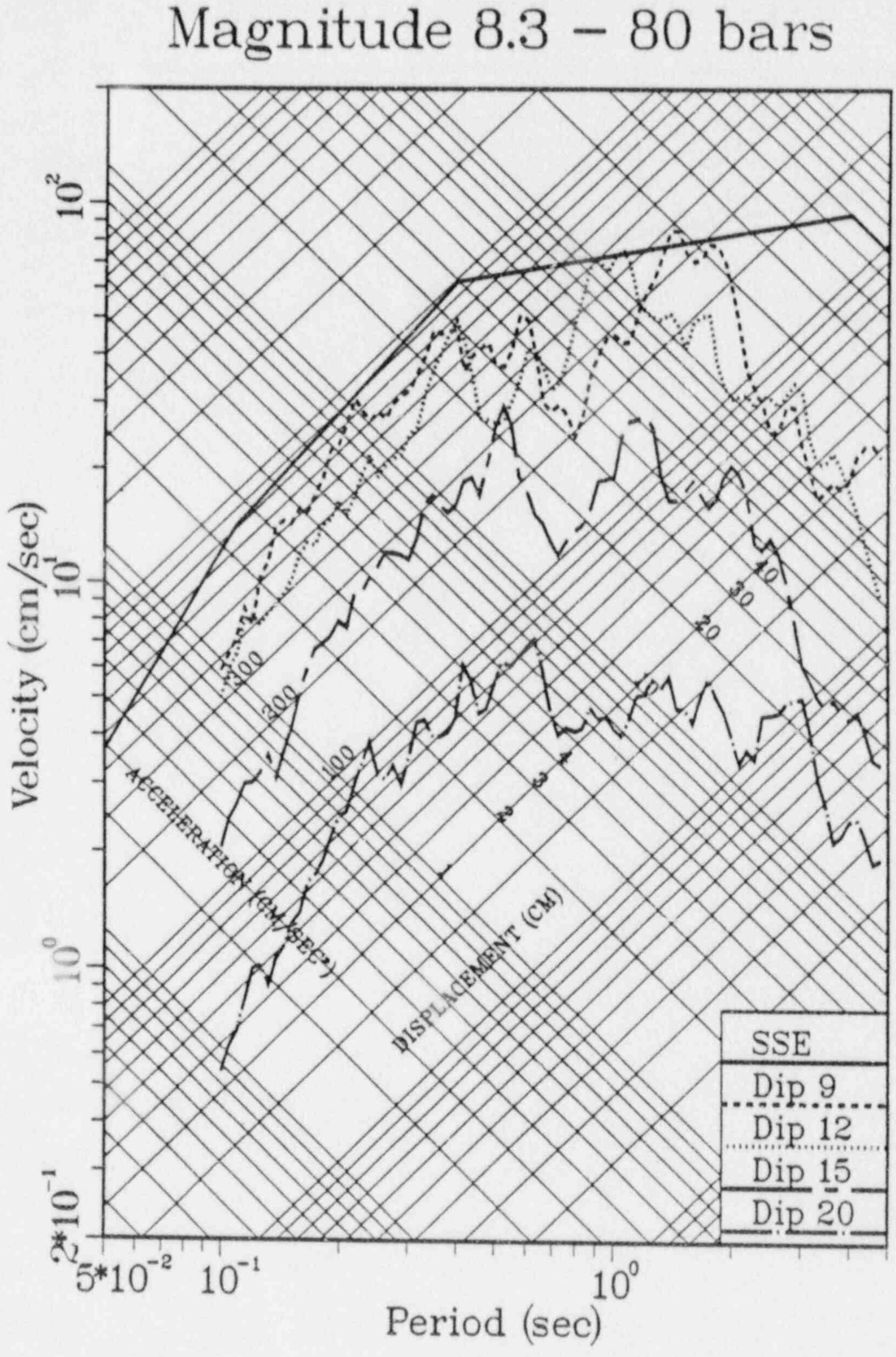

Figure 4.9. 60 km width simulations with the number of fires doubled for each subregion. This corresponds to a global stress drop of 80 bars and a moment magnitude of 8.3

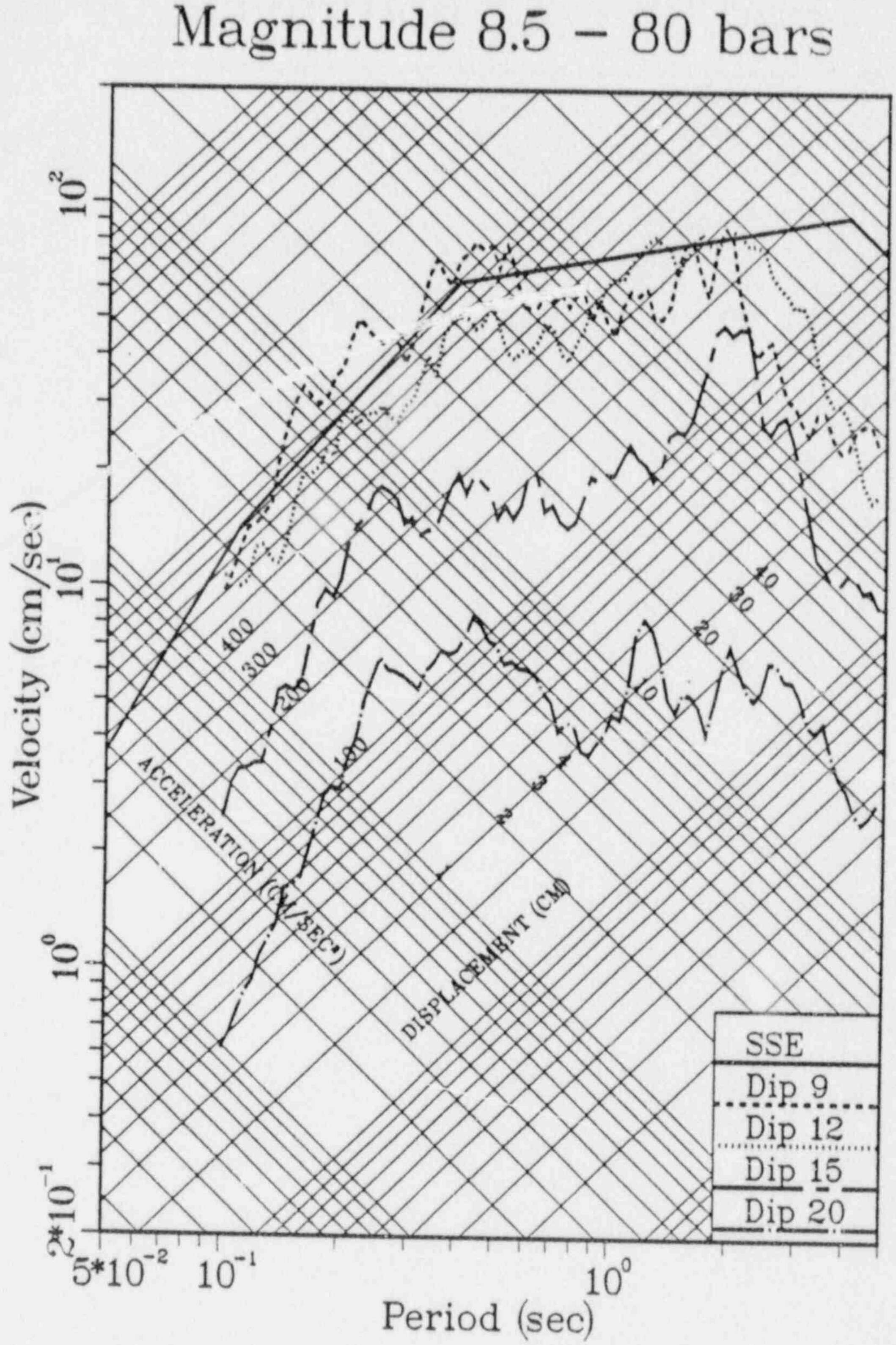

Figure 4.10. 90 km width simulations with the number of subevent repetitions doubled for each subregion. This corresponds to a global stress drop of 80 bars and a moment magnitude of 8.5.

repetition number N doubled. Assuming that the local stress drop $\Delta\tau_L$ remains constant at 38 bars, this means that the global stress drop for these hypothetical events is 80 bars, and the moment magnitudes of these events are increased by 0.2 to 8.3 for the 60 km wide events and to 8.5 for the 90 km wide events. As shown in the figures, the predicted response spectra from the 9 degree dip, magnitude 8.5 (90 km wide) simulation significantly exceeds the SSE. The increase in response spectral values, compared to the 40 bar global stress drop simulations (shown in Figures 4.5 and 4.6) is approximately a factor of $\sqrt{2}$, as predicted by Equation 2.10.

Finally, we compare our results with two other sets of observations. First, we compare our results for the magnitude 8.2 simulations with averages obtained by Heaton and Hartzell from a set of strong motion recordings of 25 shallow subduction zone earthquakes of magnitude 7.6 to 8.2 and the distance range 50 to 100 km. In our simulations, the closest point on the fault ranges from 30 km for the 9 degree simulation to 90 km for the 20 degree simulation. Figure 4.11 shows the comparison of the simulations with the empirical average and standard deviations of Heaton and Hartzell. The theoretical results are in reasonable agreement with the observations, with the results for the closest faults lying approximately one standard deviation above the mean of the observations, and the results for the most distant faults lying slightly more than one standard deviation below the mean.

Another earthquake with a geometry very similar to that of a hypothetical Washington state earthquake is the Valparaiso, Chile earthquake of March 3, 1985 moment magnitude 8.0 (Houston and Kanamori, 1986). This earthquake ruptured an area approximately 110 km in width by 170 km in length, Comte, *et al.* (1986). Most of the stations that recorded this event were located on soft soils and are not useful for comparison with the WNP-3 site; however one station, at Universidad Federico Santa Maria in Valparaiso, was located above the Eastern edge of the fault, and the depth to the fault at that location is well determined to be 39 km. The geometry is therefore almost identical to our simulation of the 12 degree dipping fault. In Figure 4.12, we show the

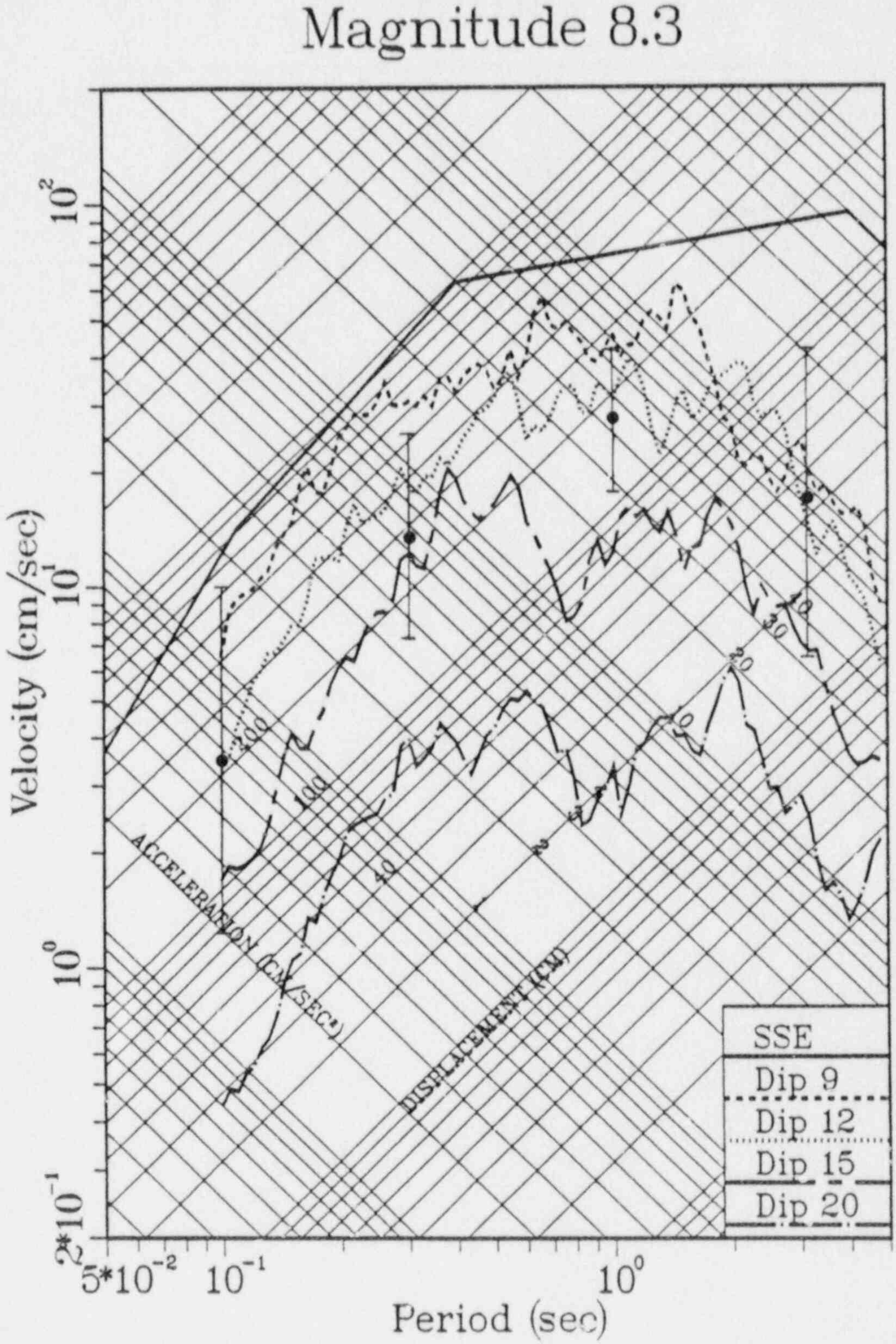

Figure 4.11. Comparison of simulated response spectra with the empirically derived average spectral values and standard deviations given by Heaton and Hartzell (1986). The observations are for a distance range of 50 to 100 km and a magnitude range of 7.6 to 8.3.

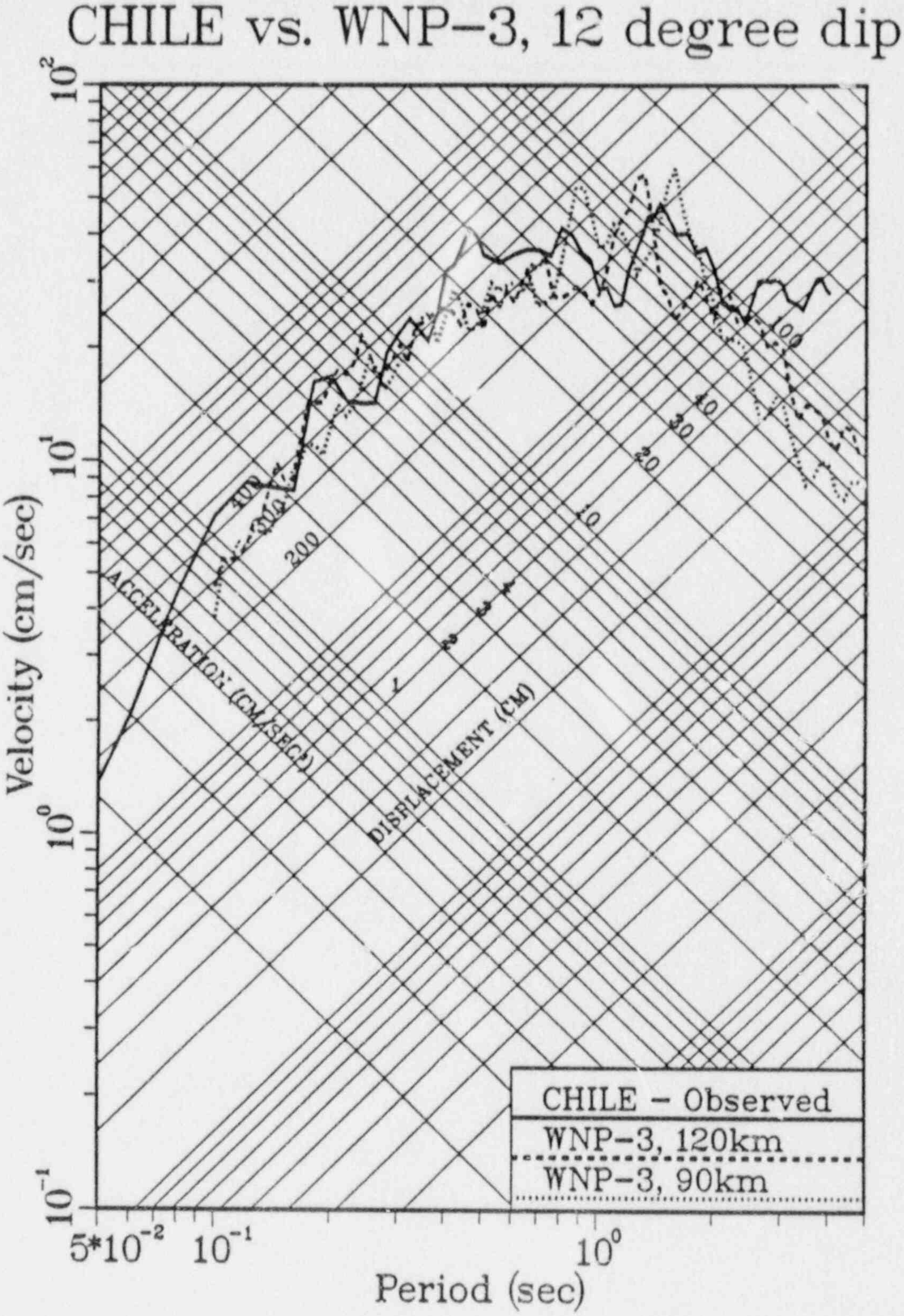

Figure 4.12. Comparison of an observed response spectrum from the March 3, 1985 Chile earthquake with the simulations for the WNP-3 site with the 12 degree dipping fault with widths of 90 and 120 km. The geometry of the Chile earthquake is similar to that for the hypothetical Washington state earthquake. The estimated width of the Chile earthquake was 110 km.

comparison of the observed response spectrum for the N70E component (the larger of the 2 horizontals) at this station (Saragoni, *et al.*, 1985) with the simulations for the 90 and 120 km wide, 12 degree dipping fault with offset rupture initiation. The agreement is quite remarkable, since no effort was made to match this data beyond a direct extrapolation of our predictions for the WNP-3 site. The 90 km simulation corresponds to moment magnitude 8.3, slightly higher than the 8.0 Valparaiso event.

4.3 Conclusions

The most important conclusion that can be drawn from this analysis in that the location of the fault relative to the WNP-3 site is of critical importance. If the fault is 40 km or more from the site (corresponding to our 12 degree dip model) ground motion is not expected to exceed the SSE, even for the largest possible earthquake.

If the fault approaches within about 30 km of the site, as in our 9 degree dip scenario, the expected ground motions from the largest possible events, of magnitude greater than 8.5, fall very near the SSE spectrum over the whole period range of interest. They exceed the SSE spectrum by a few tens of percent in the 0.2 to 0.3 second period range, which appears to be the critical part of the spectrum, i.e., that most likely to be exceeded by a large, shallow event. Ground motion for events 8.5 and smaller are predicted to fall below the SSE.

The above remarks refer to our mean estimates of ground motion, that is, those obtained using our standard earthquake model (e.g., $\Delta\tau_L$ = 38 bars, a = 2.5 km, $\Delta\tau_G$ = 40 bars, Q = 100 β). This model was calibrated through various comparisons with rock-site ground motion data presented in this section and in Section 3.

Some measure of the uncertainty in the estimates can be had by considering large, but plausible, variation in model parameters, for example, if a high (80 bar) stress drop model were considered, as in Section 4.2, then a magnitude 8.2 event (reducing the length of the magnitude 8.4 event in Section

4.2 to 100 km) is predicted to significantly exceed the SSE. We recommend, however, that uncertainty be estimated directly from the observed variability of ground motion observations on hard rock sites at distances of 50 km or less from the rupture zone of large thrust events.

V. REFERENCES

Aki, K.(1979), "Characterization of Barriers on an Earthquake Fault," JGR, 81, pp. 3575-3582.

Anderson, J. G., J. N. Brune, P. Bodin, J. Prince, R. Quaas, M. Onate, D. Almora and P. Perez (1986), "Preliminary Presentation of Accelerogram Data from the Guerrero Strong Motion Accelerograph Array, Michoacan-Guerro, Mexico, Earthquakes of 19 and 21 September 1985," Preliminary Report GAA-1A.

Anderson, J. G, P. Bodin, J. N. Brune, J. Prince, S. K. Singh, R. Quaas and M. Onate (1986), "Strong Ground Motion from the Michoacan, Mexico, Earthquake," Science, 233, pp. 1043-1049.

Anderson, J. and Hough (1984), "A Model for the Shape of the Fourier Amplitude Spectrum of Acceleration at High Frequencies," BSSA, 74, pp. 1969-1993.

Boore, D. M. (1983), "Stochastic Simulation of High-Frequency Ground Motions Based on Seismological Models of the Radiated Spectra," BSSA, 73, pp. 1865-1894.

Borcherdt, R. D. (1983), "The Coalinga Earthquake Sequence Commencing May 2, 1983," U. S. Geological Survey Open File Report 83-511.

Brune, J. M. (1970), "Tectonic Stress and the Spectra of Seismic Shear Waves," J. Geophys. Res., 75, pp.4997-5009.

Comte, D., A. Eisenberg, E. Lorca, M. Pardo, L. Pouce, R. Saragoni, S. K. Singh and G. Suarez (1986), "The Central Chile Earthquake of 3 March 1985: A Repeat of Previous Great Earthquake in the Region?", preprint.

Crosson, R. S. (1976), "Crustal Structure Modeling of Earthquake Data, 2. Velocity Structure of the Puget Sound Region, Washington," JGR, 81, pp. 3047-3054.

Crosson, R. S. (1985), "Earthquake Hazard Research in the Pacific Northwest Using Network Data," Proposal to the U. S. Geological Survey, February.

Crosson, R. S. (1986), "Where is the Subducting Slab Beneath the Pacific Northwest?", Abstracts for Papers, Meeting of the Seismological Society of America, Charleston, South Carolina.

Davies, J. N. and L. S. House (1979), "Aleutian Subduction Zone Seismicity, Volcano-Trench Separation and Their Relation to Great Thrust-Type Earthquakes," JGR, 84, pp. 4583-4591.

Davis, G. A., H. A. Coombs, R. S. Crosson, J. A. Kelleher, D. D. Tillson and W. A. Kiel (1984), "Juan de Fuca/North American Plate Convergence: Seismic or Aseismic Subduction," Report Prepared for the Washington Public Power Supply System, Nuclear Project No. 3, August.

Day, S. M. (1982a), "Three-Dimensional Simulation of Fault Dynamics: Rectangular Faults With Fixed Rupture Velocity," BSSA, 72, No. 3.

Day, S. M. (1982b), "Three-Dimensional Simulation of Spontaneous Rupture Propagation," BSSA, 72, No. 6.

Eaton, J. P. (1985), "The May 2, 1983 Earthquake and its Aftershocks: A Detailed Study of the Hypocenter Distribution and of the Focal Mechanisms of the Larger Aftershocks," in Proceeding of Workshop XXVII, Mechanics of the May 2, 1983 Coalinga Earthquake, U. S. Geological Survey Open File Report 85-44.

Eissler, H., L. Astiz and H. Kanamori (1986), "Tectonic Setting and Source Parameters of the September 19, 1985 Michoacan, Mexico Earthquake," Geophys. Res. Letters, Vol. 13, No. 6, pp. 569-572.

Ekström, G. and A. M. Dziewonski (1986), "A Very Broad Band Analysis of the Michoacan, Mexico, Earthquake of September 19, 1985," Geophys. Res. Letters, Vol. 13, No. 6, pp. 605-608.

Gradshteyn, I. S. and I. M. Ryzhik (1965), Tables of Integrals, Series and Products, Academic Press, New York.

Green, A. G., R. M. Clowes, C. J. Yorath, C. Spencer, E. R. Kanasewich, M. T. Brandon and A. S. Brown (1986), "Seismic Reflection Imaging of the Subducting Juan de Fuca Plate," Nature, 319 (16), pp. 210-213.

Gupta, I. N. and R. R. Blandford (1983), "A Mechanism for the Generation of Short-Period Transverse Motion from Explosions," BSSA, 73(2), pp. 571-592.

Hanks, T. C. and D. A. Johnson (1976), "Geophysical Assessment of Peak Accelerations," BSSA, 66, pp. 959-968.

Hanks, T. C. and H. Kanamori (1979), "A Moment Magnitude Scale," J. Geophys. Res., Vol. 84, pp. 2348-2350.

Hanks, T. C. and R. K. McGuire (1981), "The Character of High-Frequency Strong Ground Motion," BSSA, 71 (6), pp. 2071-2095.

Havskov, J., S. K. Singh, E. Nava, T. Dominguez and M. Rodriguez (1983), "Playa Azul, Michoacan, Mexico, Earthquake of 25 October 1981 (M_s = 7.3)," BSSA, 73, pp. 449-457.

Heaton, T. H. and S. H. Hartzell (1986), "Estimation of Strong Ground Motions from Hypothetical Earthquakes on the Cascadia Subduction Zone, Pacific Northwest," U. S. Geological Survey Open-File Report 86-328.

Irikura, K., "The Synthesis of Strong Ground Motions for Large Earthquakes Using the Records of Small Earthquakes as Empirical Green's Functions," Earthquake Notes, 55(1).

Iwan, W. D., M. A. Moser and C. Y. Peng, "Some Observations on Strong-Motion Earthquake Measurement Using a Digital Accelerograph," BSSA, 75, pp. 1225-1246.

Joyner, W. B. (1984), "A Scaling Law for the Spectra of Large Earthquakes," BSSA, 74 (4), pp. 1167-1188.

Kanamori, H. and D. L. Anderson (1975), "Theoretical Basis of Some Empirical Relations in Seismology," BSSA, 65, pp. 1073-1095.

Langston, C. A. and D. F. Blum (1977), "The April 29, 1965 Puget Sound Earthquake and the Crustal and Upper Mantle Structure of Western Washington," BSSA, 67, pp. 693-711.

Madariaga, R. (1977), "High-Frequency Radiation from Crack (Stress Drop) Models of Earthquake Faulting," Geophys. J. R. astr. Soc., 51, pp. 625-651.

McGuire, R. K. and T. C. Hanks (1980), "RMS Accelerations and Spectral Amplitudes of Strong Ground Motion During the San Fernando, California Earthquake," BSSA, 70, No. 5, pp. 1907-1919.

Mueller, C. S., E. Semberg and L. Wennerberg (1984), "Digital Recordings of Aftershocks of the May 2, 1983 Coalinga, California Earthquake," U. S. Geological Survey Open File Report 84-697.

Neuber, H. (1937), *Kerbspannungslehre,* Springer-Verlag, Berlin, "Theory of Notch Stresses: Principles for Exact Calculation of Strength With Reference to Structural Form and Material," the Office of Technical Information, AEC-tr-4547, 1958 (English Translation).

Owens, T. J., Hendrickson, M. and R. S. Crosson (1986), "Constraints on the Subduction Geometry Beneath Western Washington Using Broadband Teleseismic P-Waveform Modeling," Abstracts for Papers, Meeting of the Seismological Society of America, Charleston, South Carolina.

Papageorgiou, S. P. and K. Aki (1983a), "A Specific Barrier Model for the Quantitative Description of Inhomogeneous Faulting and the Prediction of Strong Ground Motion. I. Description of the Model," BSSA, 73(3), pp. 693-722.

Papageorgiou, S. P. and K. Aki (1983b), "A Specific Barrier Model for the Quantitative Description of Inhomogeneous Faulting and the Prediction of Strong Ground Motion II. Applications of the Model," BSSA, 73(4), pp. 953-978.

Priestley, K. F. and T. G. Masters (1986), "Source Mechanism of the September 19, 1985 Michoacan Earthquake and Its Implications," Geophys. Res. Letters, Vol. 13, No. 6, pp. 601-604.

Prince, J., R. Quaas, M. Onate, D. Almora, P. Perez, J. G. Anderson, J. N. Brune and P. Bodin (1986), "Preliminary Response Spectra from Accelerograms Recorded at Close Range by the Guerrero Accelerograph Array for the September 1985 Events," Preliminary Report GAA-1C.

Riddinhough, R. P. (1977), "A Model for Recent Plate Interactions Off Canada's West coast," Can J. Earth Sci., 14, pp. 384-396.

Riedesel, M. A., T. H. Jordan, A. F. Sheehan and P. G. Silver (1986), "Moment-Tensor Spectra of the 19 September 1985 and 21 September 1985 Michoacan, Mexico, Earthquakes," Geophys. Res. Letters, Vol. 13, No. 6, pp. 609.

Saragoni, R., M. Fresard and P. Gonzalez (1985), "Analisis de los Acelerogramas del Terremoto del 3 de Marzo de 1985," University of Chile Report.

Sato, T. and T. Hirasawa (1973), "Body Wave Spectra from Propagating Shear Cracks," Journal of Physics of the Earth, Vol. 21, pp. 415-431.

Scholz, C. H. (1982), "Scaling Laws for Large Earthquakes: Consequences for Physical Models," BSSA, 72 (1), pp. 1-14.

Shakal, A. F. and J. T. Ragsdale (1983), "Strong-Motion Data from the Coalinga, California Earthquake and Aftershocks," in *The 1983 Coalinga, California Earthquakes*, Special Publication 66, California Department of Conservation, Division of Mines and Geology.

Sneddon, I. N. and M. Lowengrub (1969), "Crack Problems in the Classical Theory of Elasticity," New York, John Wiley and Sons.

Spence, G. D., R. M. Clowes and R. M. Ellis (1985), "Seismic Structure Across the Active Subduction Zone of Western Canada," Preprint of Paper Submitted to JGR.

Stevens, J. L. and S. M. Day (1985), "The Physical Basis of m_b:M_s and Variable Frequency Magnitude Methods for Earthquake/Explosions Discrimination," JGR, 90(B4), pp. 3009-3020.

Stolte, C., K. C. McNally, J. Gonzalez-Ruiz, G. W. Simila, A. Reyes, C. Rebollar, L. Munguia and L. Mendoza (1986), "Fine Structure of a Postfailure Wadati-Benioff Zone," Geophys. Res. Letters, Vol. 13, No. 6, pp. 577-580.

Swanger, H. J., S. M. Day, J. R. Murphy and R. Guzman (1981), "State-of-the-Art Study Concerning Near-Field Earthquake Ground Motion," Nuclear Regulatory Commission Report NUREG/CR-1978, prepared by Systems, Science and Software.

Taber, J. (1983), "Crustal Structure and Seismicity of the Washington Continental Margin," Ph.D. Thesis, University of Washington.

Udwadia, F. E. and M. D. Trifunac (1974), "Characterization of Response Spectra Through the Statistics of Oscillator Response," BSSA, Vol. 64, pp. 205-219.

Uhrhammer, R. A. (1985). "The May 2, 1983 Coalinga Earthquake and Seismicity Rates and Strain Energy in the Central Coast Ranges, California," in *The 1983 Coalinga, California Earthquakes*, Special Publication 66, California Department of Conservation, Division of Mines and Geology.

UNAM Seismology Group (1986), "The September 1985 Michoacan Earthquakes: Aftershock Distribution and History of Rupture," Geophys. Res. Letters, Vol. 13, No. 6, pp. 573-576.

Zervas, C. E. and R. S. Crosson (1986), "P_n Observation and Interpretation in Washington," submitted to BSSA.

APPENDIX A

REGIONAL GEOLOGY AND TECTONICS

We have reviewed the regional geologic structure and tectonic setting of western Washington as it pertains to the geometry of potential subduction zone earthquakes and resultant ground motion at the WNP-3 site. The following summary cites only those studies most pertinent to the design of the sensitivity study described in Section IV.

The general seismic structure has been studied by several authors, but the studies by Crosson (1975, 1985) are most applicable to western Washington below WNP-3. Figure A.1 shows these seismic structures along with the one by Langston and Blume (1977) which pertains to the earth below Puget Sound. Our calculations have used the Crosson (1985) model since it is the most recent work. The two models by Crosson are quite similar and numerical experiments show that the results of this study are unaffected by the choice. The anelastic attenuation parameter Q is undetermined for this region. We have used the rule $Q_\beta = 100.*\beta$, where β is the shear wave velocity in km/sec, and $Q_\alpha = 4*Q_\beta$ for P waves. This yields values for Q_β of about 350 for most of the travel paths of interest, a value typical of shallow crustal rocks.

Of central importance for ground motion estimation is the position of the boundary between the subducted Juan de Fuca plate and the overlying North American plate. This region lacks a definitive set of thrust earthquakes which have helped locate the boundary in other areas thought to be similar.

The plate boundary has been explored by active seismic methods (Taber, 1983; Green, *et al.*, 1986; Spence, *et al.*, 1985), passive earthquake location and travel-time analyses (Weaver and Michaelson, 1985; Michaelson and Weaver, 1986; Zervas and Crosson, 1986) and teleseismic waveform modeling (Owens, *et al.* 1986). Figure A.2 shows the plate geometries proposed by some of these studies. The hinge line, where the plate begins to bend downward at the subduction margin appears well constrained by Taber (1983), and we have not varied its location in the sensitivity analysis in Section IV.

The maximum depth of our fault models is an estimate of the depth of the seismogenic zone, below which deformation presumably changes from brittle to ductile. The estimate, 40 km, is based on the seismicity observed for western Washington and on comparisons with areas such as the Aleutian arc (Davies and House, 1979). Since the rate of underthrusting in the Aleutian arc is higher than in western Washington, the depth to the brittle-to-ductile transition is thought to deeper there (Riddihough, 1977; Davis, *et al.*, 1984). However, we have chosen a conservative value of 40 km.

Estimates of the average fault dip between the hinge point and the base of the seismogenic zone vary greatly in the studies cited above. However, the range 9 degrees to 20 degrees bounds most of these estimates, and we adopt these bounds for the sensitivity study in Section IV.

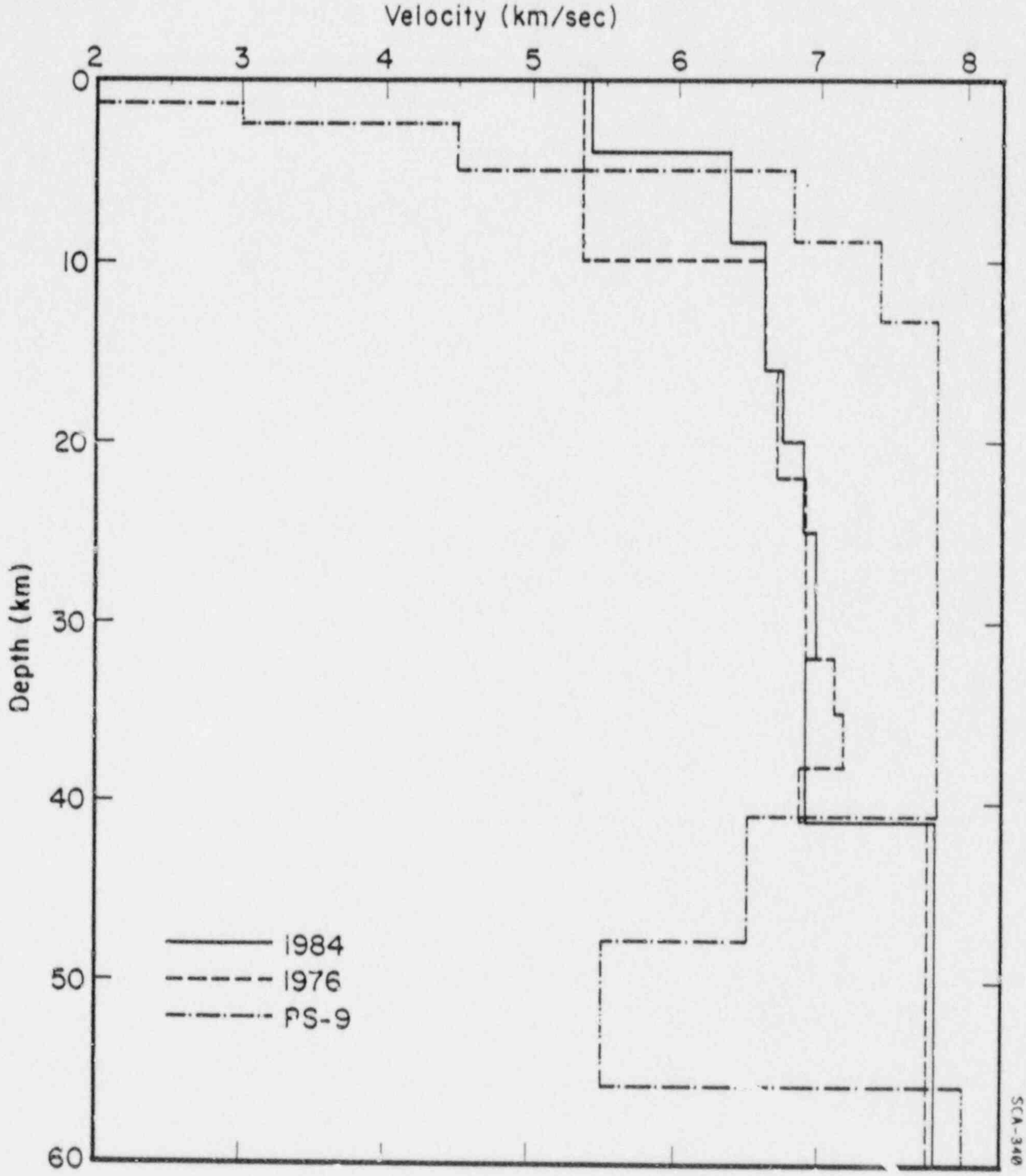

Figure A.1. P-wave velocity models proposed by Crosson (1976, 1985) and Langston and Blum (1977) for the Puget Sound region of western Washington.

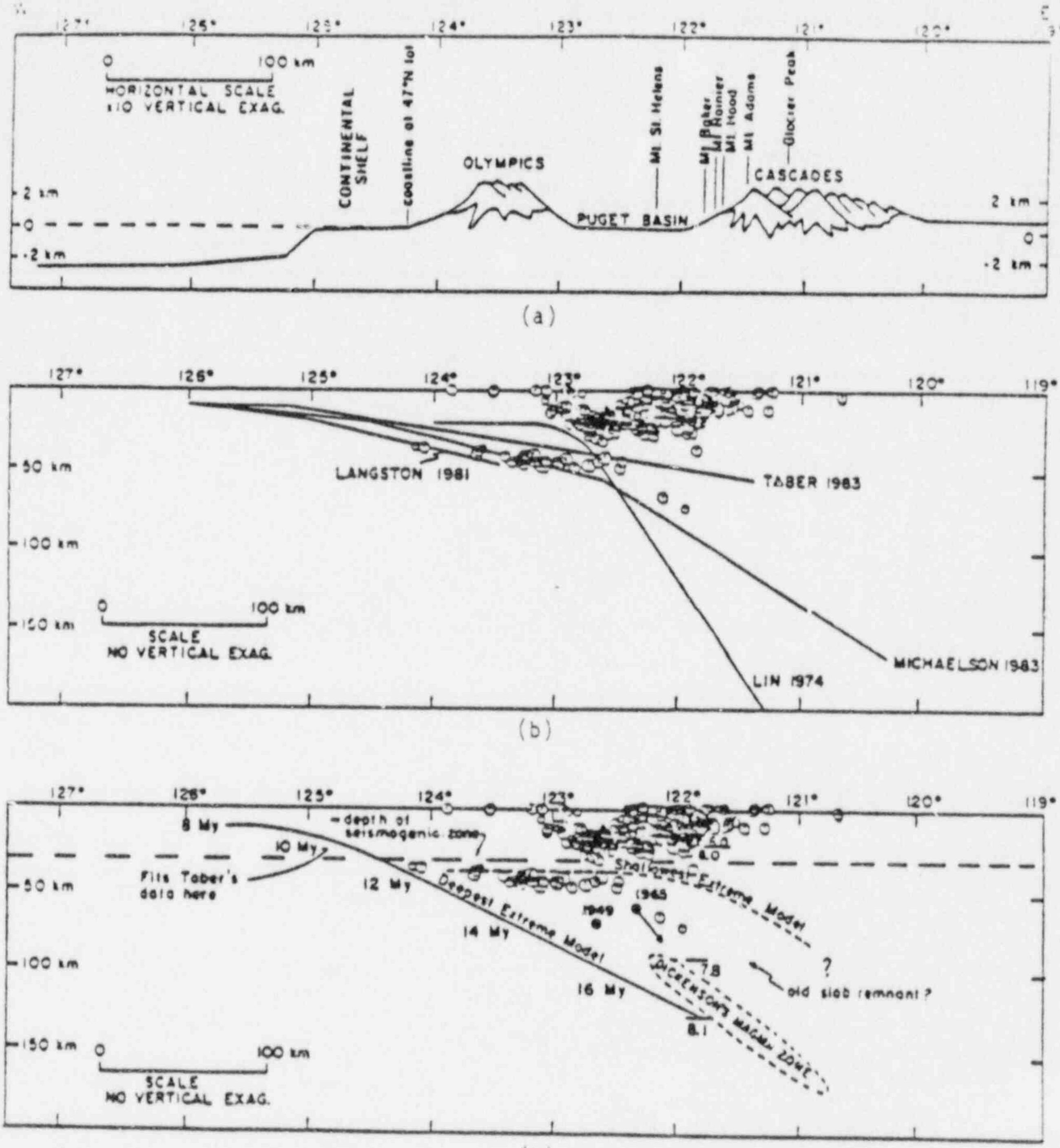

Figure A.2. Schematic cross sections showing possible alternative plate geometries in the vicinity of 47 degrees north latitude (from Crosson, 1985). the top panel (a) depicts topography with a vertical exaggeration of 10:1. The middle and bottom panels (b and c) have no vertical exaggeration and show earthquakes located in the south Puget Sound region between 1974 and 1983. The lines in Panel b represent the transition to high slab seismic velocities proposed by different authors. Shallow and deep extremes of the possible slab configuration are indicated in Panel c.

APPENDIX B

COMPUTATION OF SUBEVENT RADIATION

The Subevent Model

Each subregion slip episode is assumed to behave as a planar, nonuniformly prestressed shear crack. The slip history for two such events were used. They were computed using a finite difference method. For Calculation NRC1, the rupture velocity was prescribed to be 90 percent of the shear wave velocity. Calculation NRC7 was done with a slip-weakening criterion of failure governing crack evolution and Coulomb friction retarding the subsequent slip (Day, 1982a and b).

Figure B.1 shows the dynamic stress drop distribution over the crack for Calculation NRC7. Note that five localized patches are present on which the dynamic stress drop is more than twice the average value. For NRC1, the stress distribution was uniform and the subevent length and width were equal.

Subevent Seismic Radiation

The subevent simulation characterizes the fault slip as a function of time and position in the fault plane – $s(\xi_1, \xi_2, t)$. From s and the Green's function of the earth model, G, we can compute the subevent contribution $u(\underline{x}, t)$ to ground displacement via the representation theorem. In the frequency domain, we have

$$u_n(\underline{x}, t) = \iiint d\xi_1 d\xi_2 d\tau \dot{s}_i(\xi_1, \xi_2, \tau) \; \nu_j C_{ijpq} \; G_{np,q} \; (\underline{x}, \underline{\xi}, t-\tau), \qquad \text{(B.1)}$$

where C is the elastic tensor, ν is the unit normal to the fault plane and the spatial integral is over the fault subregion. We make the following two approximations. First, we assume that G can be approximated adequately by ray theory, one consequence being neglect of near-field contributions. Thus, the method is accurate only for wavelengths small compared to the distance from the source to the site of interest. Second, we simplify the integral by introducing an approximation equivalent to the Fraunhoffer approximation in optical diffraction theory. Specifically, we assume that we can neglect variation of G over the subregion, apart from a correction for travel time variations due to

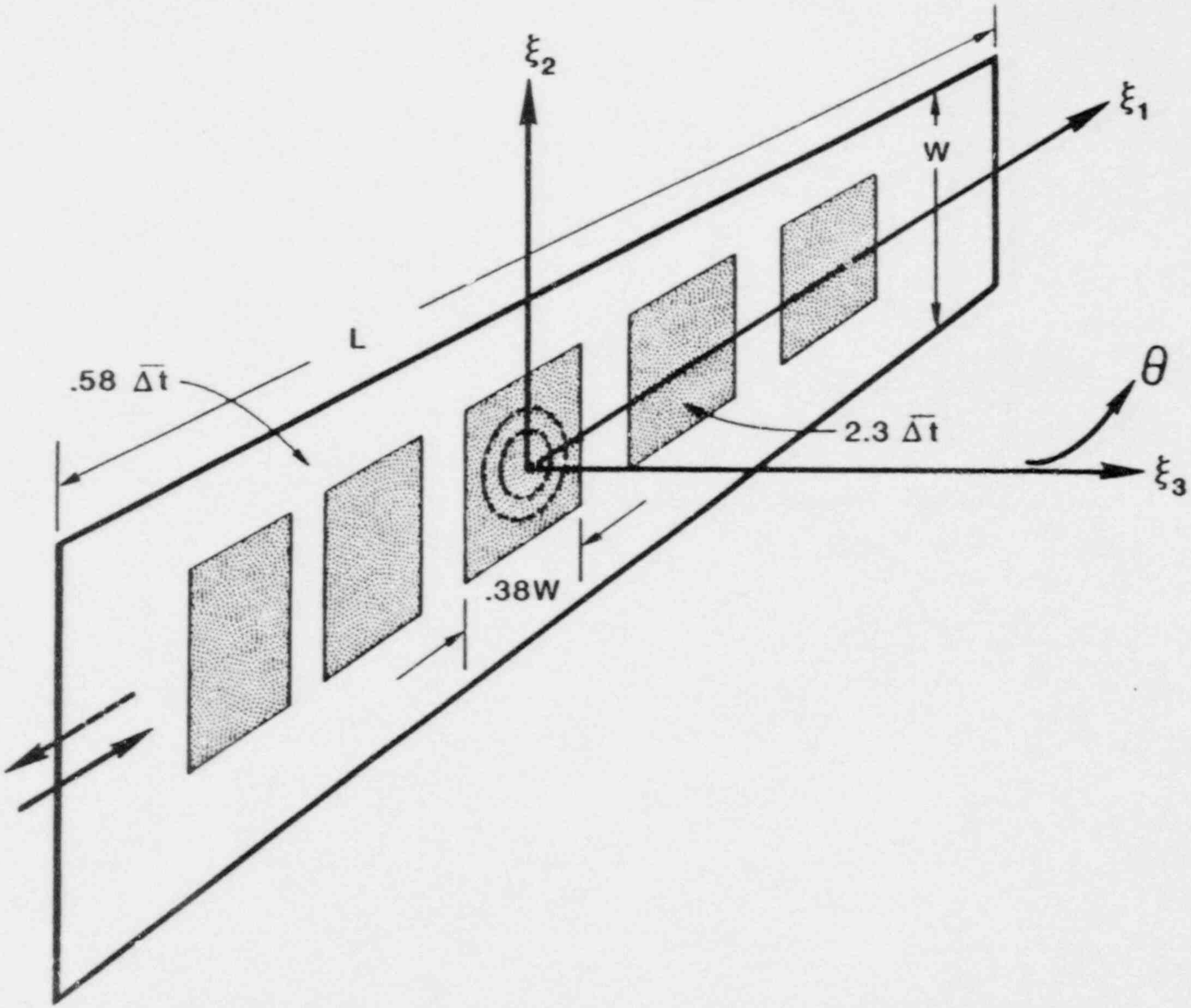

Figure B.1. Prestress geometry for the nonuniform subevent model NRC7. L and W are subevent dimensions and $\overline{\Delta\tau}$ is the average dynamic stress drop.

changes in ray-path length. We approximate the time delays separately for each S and P wave ray, only retaining first order terms in the fault plane coordinates. Referring to Figure B.2, we thus approximate a given S wave ray contribution $\nabla G^{(s)}$ by

$$\nabla G^{(s)}\left(\underline{x},\underline{\xi},\tau\right) \sim \nabla G^{(s)}\left[\underline{x},0,\tau - \frac{\underline{\xi} \cdot \gamma}{\beta}\right], \tag{B.2}$$

where β is the shear wavespeed and γ a unit vector in the ray direction. We use a similar expression for each P-wave ray. Assuming that the slip direction is invariant over the subregion, the corresponding contribution to the integral B.1 reduces, in the frequency domain, to terms of the form

$$u_n^{(s)}\left(\underline{x},\omega\right) = e_i \; \gamma_j \; C_{ijpq} \; G^{(s)}_{np,q} \; \left(\underline{x},0,\omega\right) \; \bar{\dot{s}} \; \left(k_1,k_2,\omega\right). \tag{B.3}$$

$\dot{s}$ is the three-dimensional Fourier transform of the slip speed $|\dot{s}|$,

$$\bar{\dot{s}}\left(k_1,k_2,\omega\right) = \iiint d\xi_1 \; d\xi_2 \; d\tau \; \dot{S}\left(\xi_1,\xi_2,\tau\right) \; e^{i\left(k_1\xi_1+k_2\xi_2-\omega\tau\right)} \quad . \tag{B.4}$$

$\underline{e}$ is a unit vector in the direction of slip, and k_1 and k_2 are given by

$$k_1 = \frac{\omega}{\beta}\,\gamma_1$$

$$k_1 = \frac{\omega}{\beta}\,\gamma_2 \quad .$$

The two approximations which led to B.3 restrict the range of wavelength over which the ground motion calculations are applicable. First, the use of ray theory implies the far field approximation – wavelength much less than distance

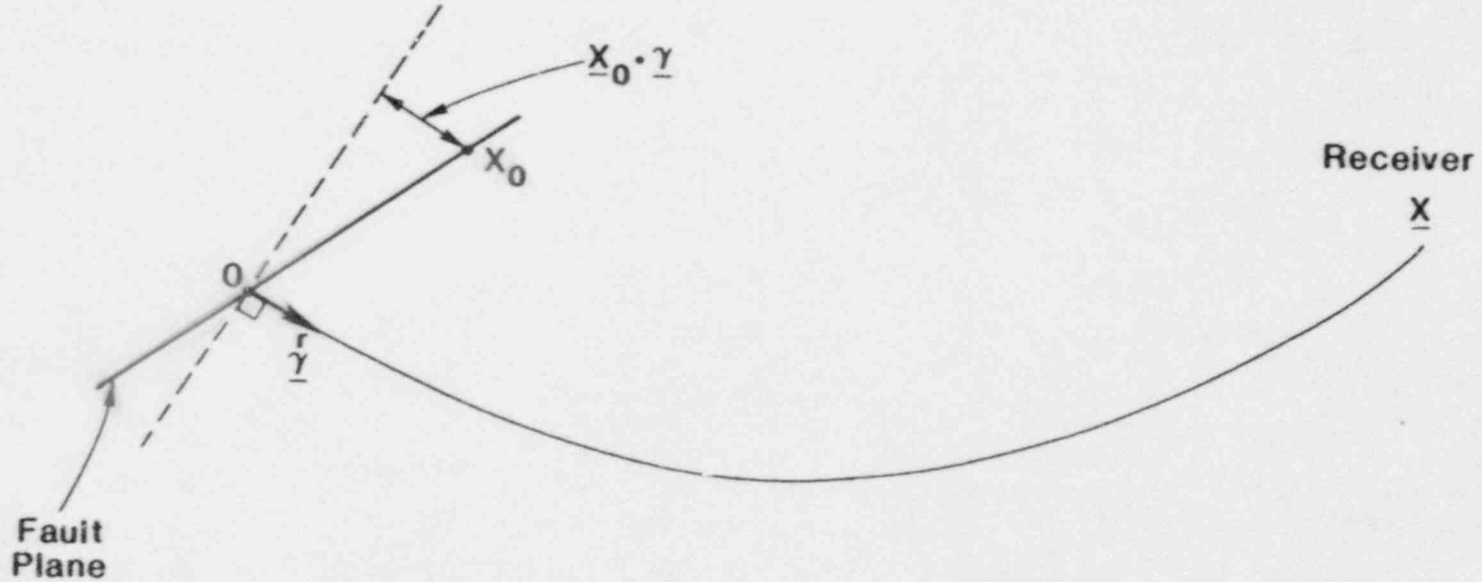

Figure B.2. Sketch of a ray leaving the center of a fault subregion. Contributions from adjacent points $\underline{x}_0$ of the subregion are obtained by a simple delay operator, with the path length diminished by $\underline{x}_0 \cdot \gamma$, where γ is a unit vector along the ray direction.

to the site. The shear wave is of most importance for strong motion at close range, and we have to consider a minimum range of roughly 30 km and maximum shear velocity of roughly 3.5 km/sec. Then the approximation should be acceptable for periods below roughly two seconds (wavelength/range $\simeq$ 1/5). Since our interest is in periods below one second for nuclear power plant response, the far field approximation is appropriate. Of course, the more general adequacy of ray theory still has to be addressed. We remark on this question in Section III, and several distinct shortcomings are identified in the course of comparing ray theory simulations to observation.

The second approximation, the linear treatment of phase (Fraunhofer approximation) imposes a short-period limitation. The approximation is carefully examined by Aki and Richards (1980, Page 805), who give the following conservative criterion on wavelength λ:

$$L^2 << \frac{\lambda r_0}{2} \tag{B.5}$$

where r_0 is source-receiver range and L is subevent dimension. The inequality is satisfied for shear waves down to about 0.15 seconds period.

APPENDIX C

APPROXIMATE ANALYTICAL SOLUTION

The earthquake model described in Section 2 represents ground motion as a sum of subevent contributions. Our interest is in sites directly above a very large fault plane. In this case, the maximal part of the wavetrain will be dominated by contributions from those subevents which are least attenuated by geometrical spreading and anelastic loss, that is, by those located on the part of the fault nearest the observation point. We focus on this maximal interval of the wavetrain and assume that it is characterized by the following approximations: (1) only the direct shear wave from a subevent is considered, (2) all subevent shear wave arrivals in this interval are identical in waveform, (3) the spectrum of this waveform has the form proposed by Brune (1970), (4) geometrical spreading, receiver functions, and radiation pattern for each ray in the maximal interval of the wavetrain are represented by the single factor R^{-1}, where R is the nearest point of the fault to the observation point, (5) arrival times of subevent shear waves are randomly distributed over the interval, and (6) the length of the maximal part of the wavetrain is long enough compared to periods of interest that we can justify treating it as stationary for the purpose of applying random vibration theory.

These approximations lead to a ground motion time series consisting of shot noise. That is, the ground displacement is the convolution of a random spike sequence with the subevent source function. We now compute the power spectrum of the ground acceleration, then apply random vibration theory to compute the response spectrum and peak acceleration.

Let S(t) be a Poisson-distributed, infinite array of delta functions, with mean rate of spike occurrence λ. That is,

$$S(t) = \sum_{n=-\infty}^{\infty} \delta \left(t - t_n\right)$$

where the t_n are randomly distributed such that the following probability pertains:

(Note that the Brune stress drop parameter $\Delta\sigma$ is approximately a factor of two less than the stress drop associated with the numerical source models when scaled to have the same low and high-frequency asymptotes. For comparison with the numerical simulations, $\overline{\Delta\tau}_L$ should be interpreted as $2\,\Delta\sigma$.)

The power spectrum of the random subevent sequence, in the high frequency limit, is then the product of Equation (C.5) and the second term of Equation (C.3):

$$S_{ss}\ |\hat{a}|^2 \sim \left(\frac{0.32\ \pi\ \Delta\sigma}{\rho\ \beta\ R}\right)^2 \lambda\ e^{-\frac{2\pi R f}{Q\beta}} \quad . \tag{C.6}$$

We next determine the peak relative displacement of a damped harmonic oscillator in response to the shot noise series, denoting the relative displacement by u(t). The energy spectrum of a damped harmonic oscillator impulse response to acceleration is

$$|H(f)|^2 = \frac{1}{\left(2\pi\right)^4\left[\left(f_0^{\,2} - f^2\right)^2 + \left(2\ \gamma\ f_0\ f\right)^2\right]} \tag{C.7}$$

where f_0 is the natural frequency and γ is the critical damping fraction. Multiplying by $S_{ss}|\hat{a}(f)|^2$ gives the oscillator relative displacement power spectrum. Using Equation C.6 gives

$$S_{uu}(f) \sim \left(\frac{0.32\ \pi\ \Delta\sigma\ a}{\rho\ \beta\ R}\right)^2 \frac{\lambda\ e^{-\frac{2\pi R f}{Q\beta}}}{(2\pi)^4\left[\left(f_0^{\,2} - f^2\right)^2 + \left(2\ \gamma\ f_0\ f\right)^2\right]} \tag{C.8}$$

at high frequency.

The mean square value of the oscillator relative displacement over the duration of oscillator response T_u is

$$\frac{1}{T_u} \int_{-\infty}^{\infty} |u(t)|^2 \, dt = \int_{-\infty}^{\infty} S_{uu}(f) \, df \quad . \qquad \text{(C.9)}$$

$$= \left[\frac{0.32 \; \pi \; \Delta\sigma \; a}{\rho \; \beta \; R}\right]^2 \lambda \, \frac{1}{(2\pi)^4} \int_{-\infty}^{\infty} \frac{df \; e^{-\frac{2\pi R f}{Q\beta}}}{\left[f_0^{\,2} - f^2\right]^2 + \left[2 \, \gamma \, f_0 \, f\right]^2} \quad . \qquad \text{(C.10)}$$

For small γ, the oscillator response is strongly peaked around f_0. So long as f_0 is small compared with $Q\beta/R$, an excellent approximation is to evaluate the exponential factor at $f = f_0$. The remaining integral is easily integrated via Parseval's theorem, using the oscillator impulse response:

$$\frac{1}{(2\pi)^4} \int_{-\infty}^{\infty} \frac{df}{\left[f_0^{\,2} - f^2\right]^2 + \left[2 \, \gamma \, f_0 \, f\right]^2} =$$

$$\frac{1}{\left(1-\gamma^2\right)\left(2\pi\right)^2 \, f_0^{\,2}} \int_0^{\infty} dt \; e^{-2(2\pi) \, \gamma f_0 \, t} \, \sin^2 \left(1-\gamma^2\right)^{1/2} 2 \, \pi \, f_0 \, t \quad .$$

From Gradshteyn and Ryzik (1965), Page 478, Equation 3.895,

$$\int_0^{\infty} e^{-\beta x} \sin^{2\,m} x \, dx = \frac{2 \, m!}{\beta \left(\beta^2 + 2^2\right)\left(\beta^2 + 4^2\right) \; \ldots \; \left[\beta^2 + (2\,m)^2\right]} \quad ,$$

whence

$$\frac{1}{T_u} \int_{-\infty}^{\infty} |u(t)|^2 \, dt \approx \left(\frac{0.32 \, \pi \, \Delta\sigma \, a}{\rho \, \beta \, R}\right)^2 \frac{1}{4(2\pi)^3} \frac{\lambda \, e^{-\frac{2\pi R f}{Q\beta}}}{\gamma \, f_0^3} . \qquad (C.11)$$

The peak oscillator response can be related to the rms response via random vibration theory. The rms response in just the square root of Equation C.11:

$$U_{rms} = \frac{0.32 \, \Delta\sigma \, a}{4 \sqrt{2\pi} \, \rho \, \beta \, R} \left(\frac{\lambda}{\gamma \, f_0}\right)^{1/2} f_0^{-1} \, e^{-\frac{\pi R f_0}{Q\beta}} \qquad (C.12)$$

To relate u_{rms} to the oscillator peak response u_{max}, we follow Udwadia and Trifunac (1974). From random vibration theory, the expected value of u_{max} is

$$E \frac{(u_{max})}{\sqrt{2} \, u_{rms}} \sim \left\{ \ln \left[(1-\epsilon^2)^{1/2} N_p \right] \right\}^{1/2} + \frac{1}{2} \gamma \left\{ \left[\ln \, (1-\epsilon^2)^{1/2} N_p \right] \right\}^{-1/2}$$

(valid for large $(1-\epsilon^2)^{1/2} N_p$) (C.13)

where N_p is the number of peaks in the sample time series and ϵ depends upon the spectral shape. For damping ratios 0.01 to 0.1, the oscillator response is sufficiently monochromatic to approximate N_p by $T_u \, f_0$, and ϵ is roughly in the range 0.2 to 0.6. Equation C.13 is so insensitive to ϵ in this range that C.13 can be replaced by $(\ln N_p)^{1/2}$ for our purposes (see, for example, Udwadia and Trifunac, Figure 4). This gives

$$E(u_{max}) \sim \frac{0.32}{4 \sqrt{\pi}} \frac{\Delta\sigma \, a}{\rho \, \beta \, R} \left[\frac{\lambda \, \ln \, (T_u \, f_0)}{\gamma \, f_0}\right]^{1/2} f_0^{-1} \, e^{-\frac{\pi R f_0}{Q\beta}} . \qquad (C.14)$$

The pseudo-velocity response V is $2 \pi f_0 \, u_{max}$, or

$$V(f_0) \sim \frac{0.32\sqrt{\pi}}{2} \; \frac{\Delta\sigma \; a}{\rho \; \beta \; R} \left[\frac{\lambda \; \ln \; (T_u \; f_0)}{\gamma \; f_0}\right]^{1/2} e^{-\frac{\pi R f_0}{Q\beta}} \tag{C.15}$$

(Recall that the local stress drop $\Delta\tau_L$ in the numerical simulations refers to our numerical subevent models, for which stress drop is approximately twice the Brune prediction $\Delta\sigma$.)

Similarly, we can calculate the peak acceleration, a_{max}, which is just

$$a_{max} = \lim_{f_0 \to \infty} 2\pi \; f_0 \; V \; (f_0) \; . \tag{C.16}$$

We need to recompute the integral in Equation C.10 for the case $f_0 >> Q\beta/R$. In this case the integral is

$$\int_{-\infty}^{\infty} \frac{e^{-\frac{2\pi R f}{Q\beta}}}{\left(f_0^{\,2} - f^2\right)^2 + \left(2 \; \gamma \; f_0 \; f\right)^2} \, df \approx \frac{1}{2 \; \gamma \; f_0^{\,2}} \int_{-\infty}^{\infty} \frac{e^{-\frac{2\pi R f}{Q\beta}}}{f_0^{\,4} + 4 \; \gamma \; f_0^{\,2} \; f^2} \; df$$

$$= \frac{Q\beta}{\pi \; R \; f_0^{\,4}} \left[1 - 2! \left(\frac{Q \; \beta \; \gamma^{1/2}}{f_0 \; \pi \; R}\right)^2 + 4! \left(\frac{Q \; \beta \; \gamma^{1/2}}{f_0 \; \pi \; R}\right)^4 - \; \ldots \right]$$

$$\approx \frac{Q\beta}{\pi \; R \; f_0^{\,4}} \; . \tag{C.17}$$

Then we repeat the steps leading from Equation C.10 to C.15. Following Hanks and McGuire (1981) we use the estimate $Q\beta/\pi R$ for the predominant frequency, and approximate N_p (appearing in Equation C.13) by $T_u \; Q\beta/\pi R$. Then, plugging the result into Equation C.16 gives

$$a_{max} = \frac{0.32\ \sqrt{2}\ \pi\ \Delta\sigma\ a\ \lambda^{1/2}}{\rho\ \beta\ R} \left(\frac{Q\beta}{\pi R}\right)^{1/2} \left[\ln\left(\frac{Q\beta}{\pi R}\ T_u\right)\right]^{1/2} \quad (C.18)$$

If whole-path attenuation does not dominate over exponential decay due to source and/or site effects, then the factor $(Q\beta/\pi R)^{1/2}$ should be replaced by $f_{max}^{1/2}$, where f_{max} is the source- or site-controlled cutoff frequency (Hanks and McGuire, 1981; Anderson and Hough, 1984).

Finally, we require an estimate of the shot rate, λ. A fairly crude estimate may do, since λ enters Equations C.15 and C.18 only as a square root. The duration of the dominant ground motion contribution can be roughly approximated as rupture duration over the portion of the fault whose receiver distance is with $\sqrt{2}$ of this minimum distance (a 45° cone about the fault normal at nearest approach). The mean shot rate λ during this dominant motion can be approximated by the total number of subregions in this near-receiver zone times the number of repeat firings N which can occur while the rupture is sweeping this zone. Thus, we have the following rough estimates:

$$T_u \approx \frac{2R}{\nu_R} + T_R \quad (C.19)$$

$$\lambda \approx \frac{N\ \pi\ R^2}{4\ a^2\ T_u} \quad (C.20)$$

APPENDIX D

SIMULATED RESPONSE SPECTRA AT THE WNP-3 SITE

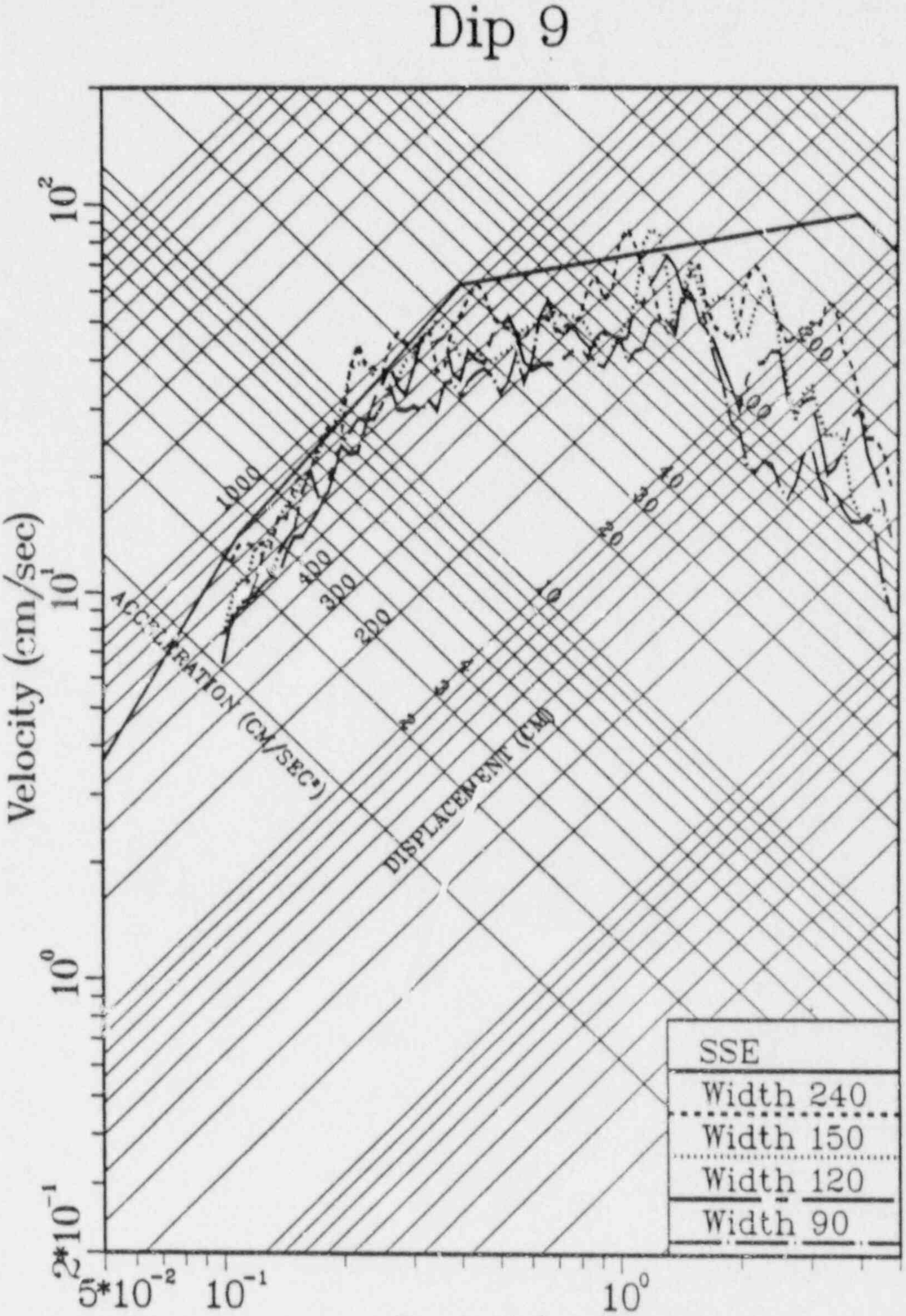

Figure D.1. Simulated 5 percent damped response spectra at the WNP-3 site for an earthquake with a dip of 9°, central rupture initiation point, and widths of 240 km, 150 km, 120 km and 90 km.

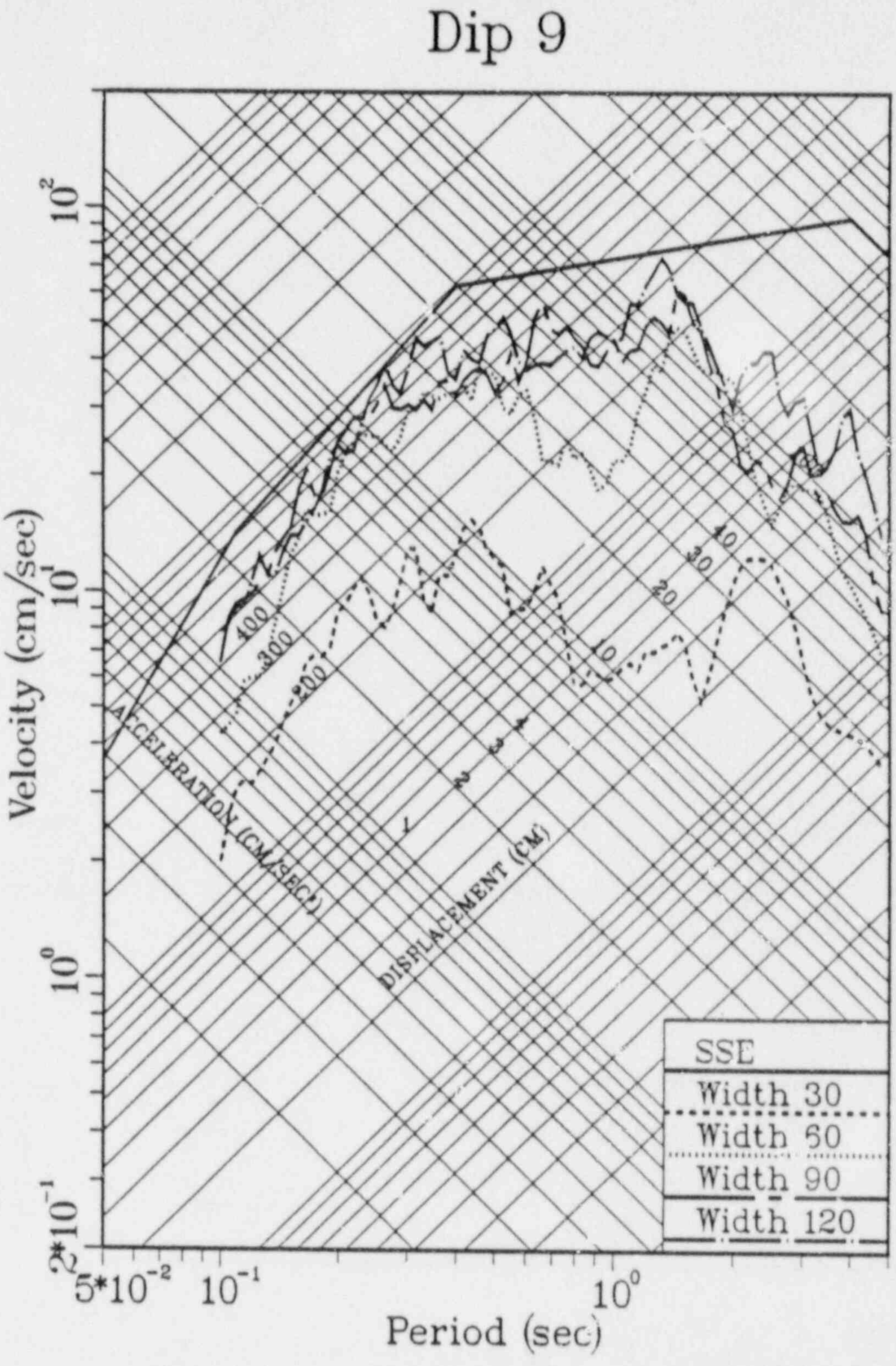

Figure D.2. Simulated 5 percent damped response spectra at the WNP-3 site for an earthquake with a dip of 9°, central rupture initiation point, and widths of 30 km, 60 km, 90 km and 120 km.

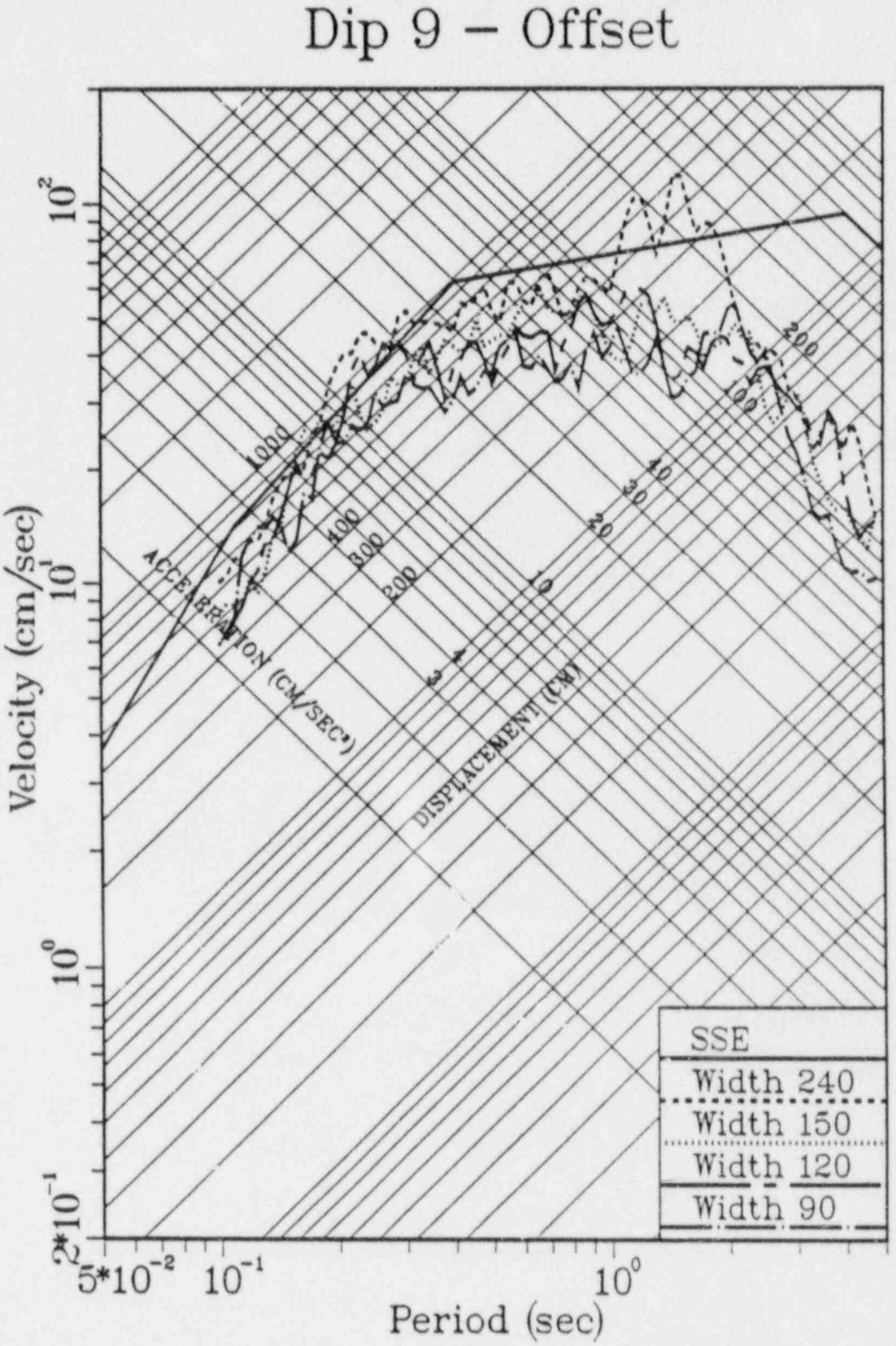

Figure D.3. Simulated 5 percent damped response spectra at the WNP-3 site for an earthquake with a dip of 9°, offset rupture initiation point, and widths of 240 km, 150 km, 120 km and 90 km.

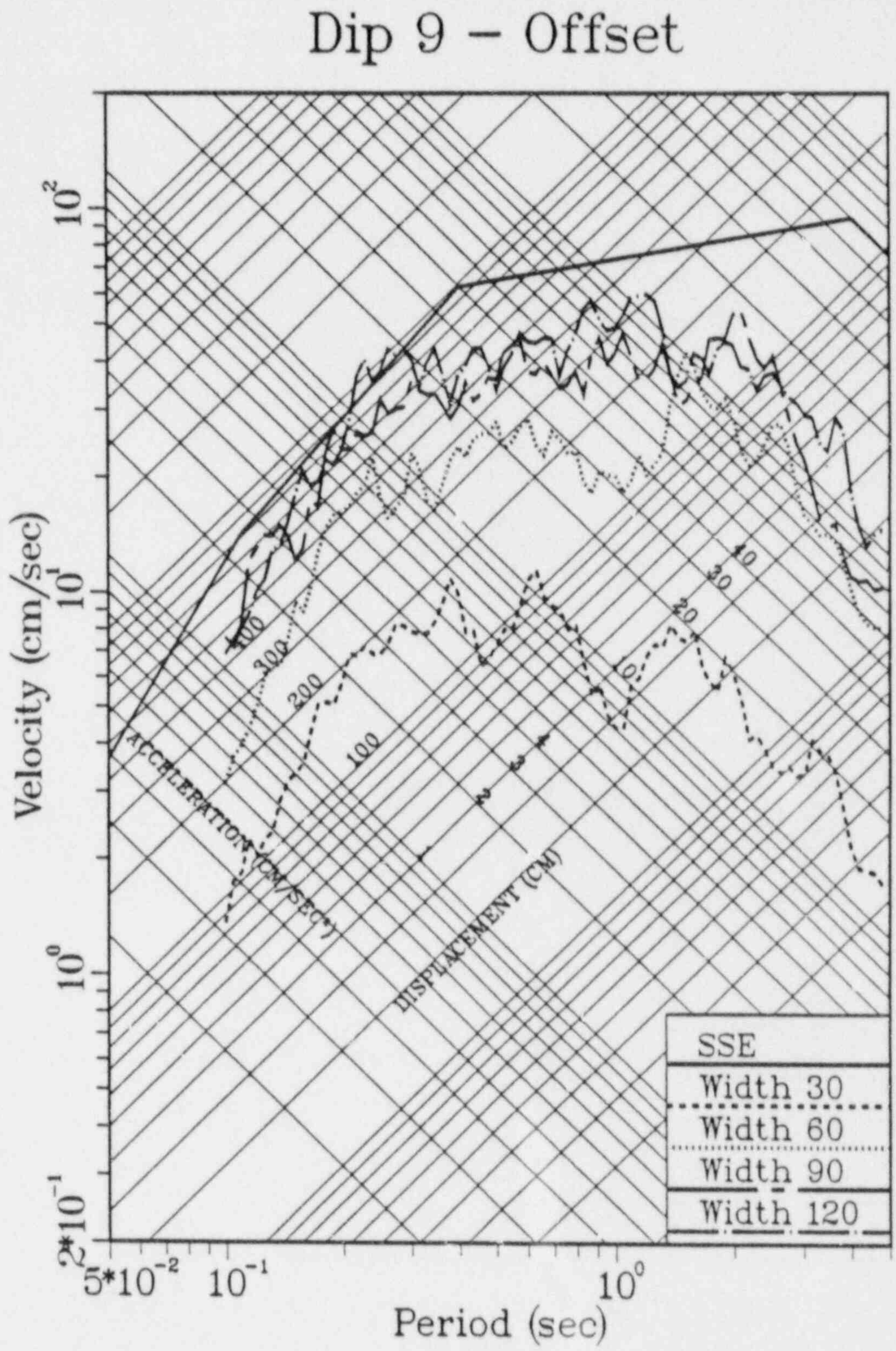

Figure D.4. Simulated 5 percent damped response spectra at the WNP-3 site for an earthquake with a dip of 9°, offset rupture initiation point, and widths of 30 km, 60 km, 90 km and 120 km.

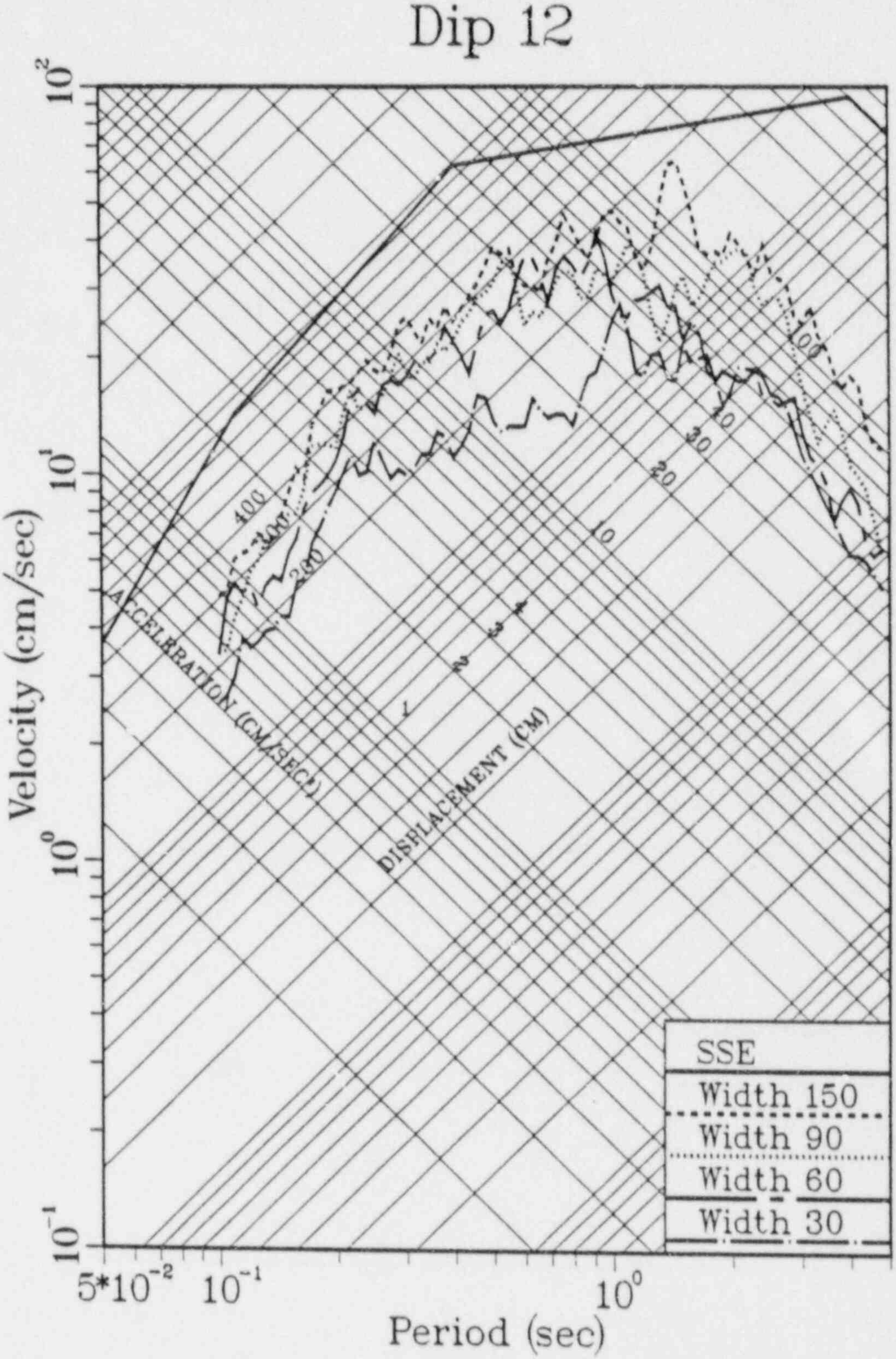

Figure D.5. Simulated 5 percent damped response spectra at the WNP-3 site for an earthquake with a dip of 12°, central rupture initiation point, and widths of 150 km, 90 km, 60 km and 30 km.

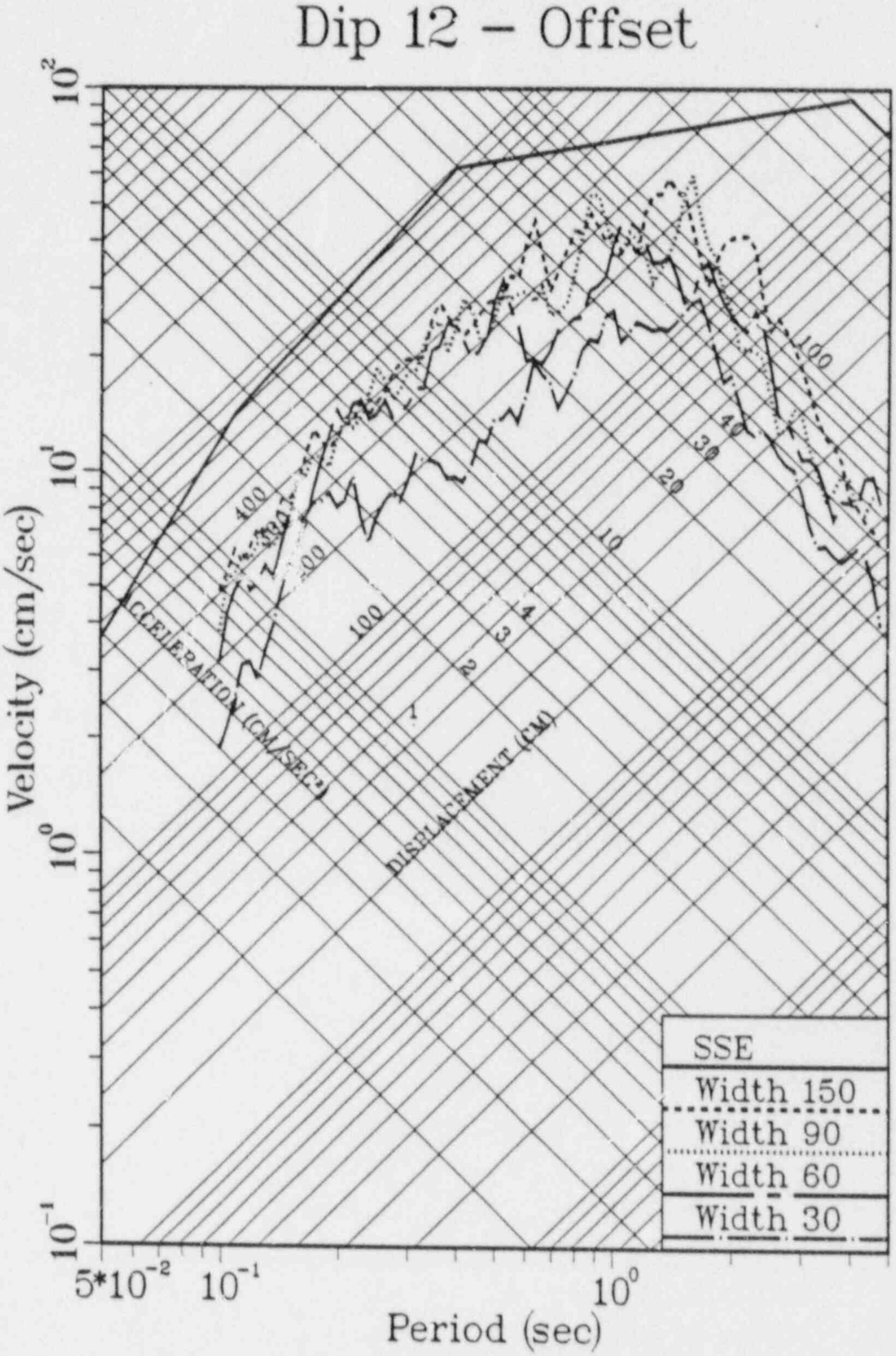

Figure D.6. Simulated 5 percent damped response spectra at the WNP-3 site for an earthquake with a dip of 12°, offset rupture initiation point, and widths of 150 km, 90 km, 60 km and 30 km.

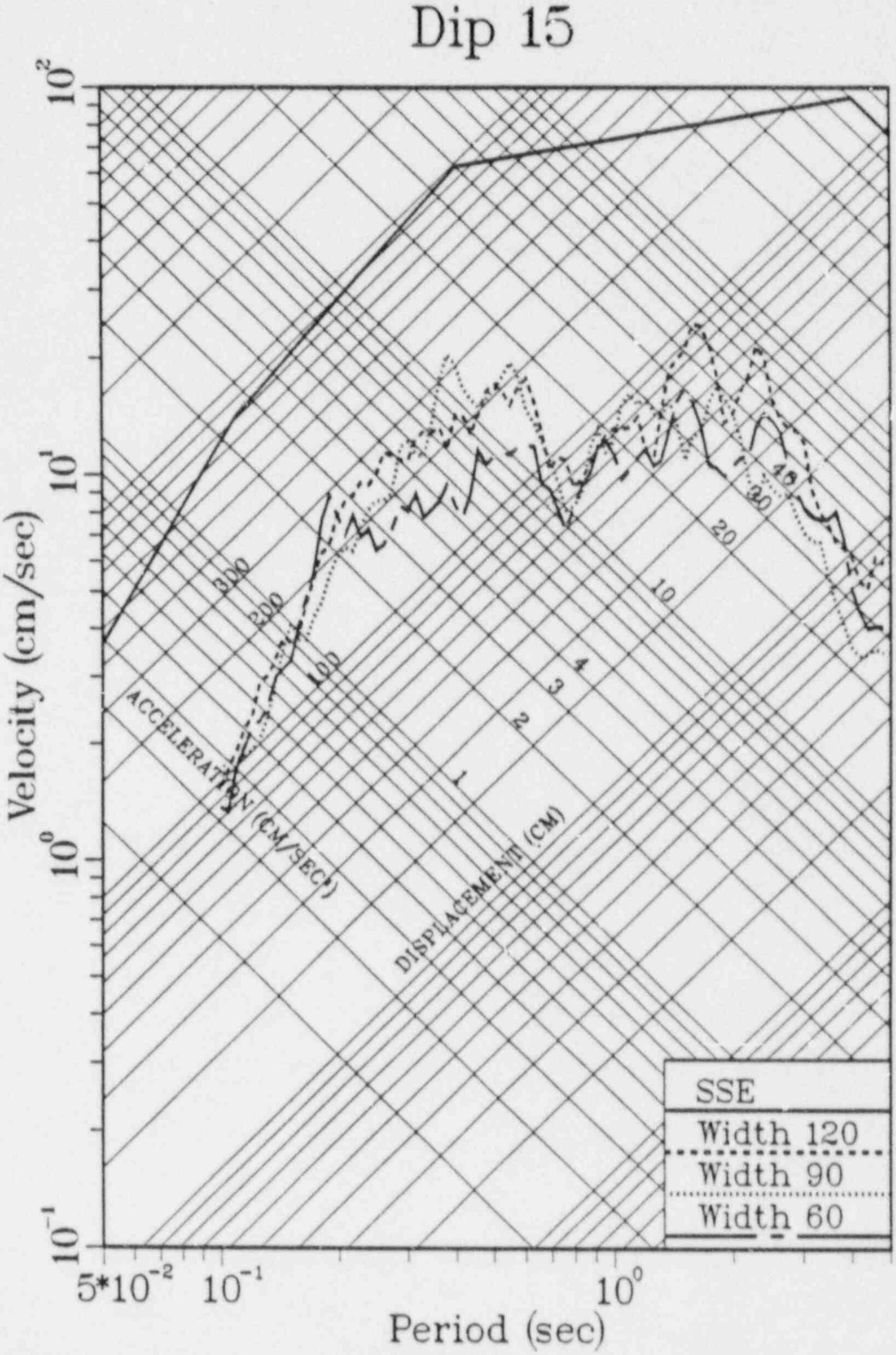

Figure D.7. Simulated 5 percent damped response spectra at the WNP-3 site for an earthquake with a dip of 15°, offset rupture initiation point, and widths of 120 km, 90 km and 60 km.

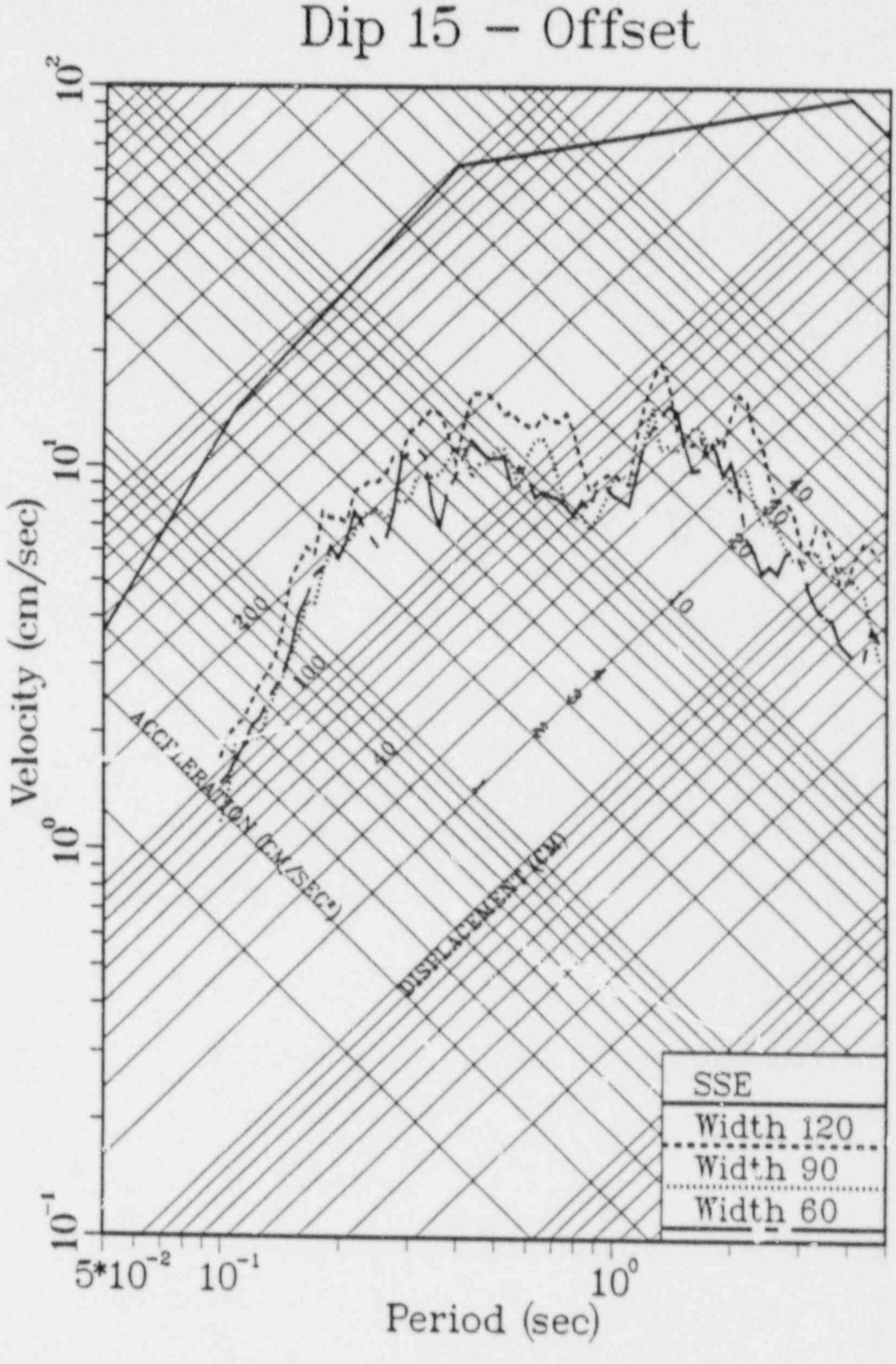

Figure D.8. Simulated 5 percent damped response spectra at the WNP-3 site for an earthquake with a dip of 15°, offset rupture initiation point, and widths of 120 km, 90 km and 60 km.

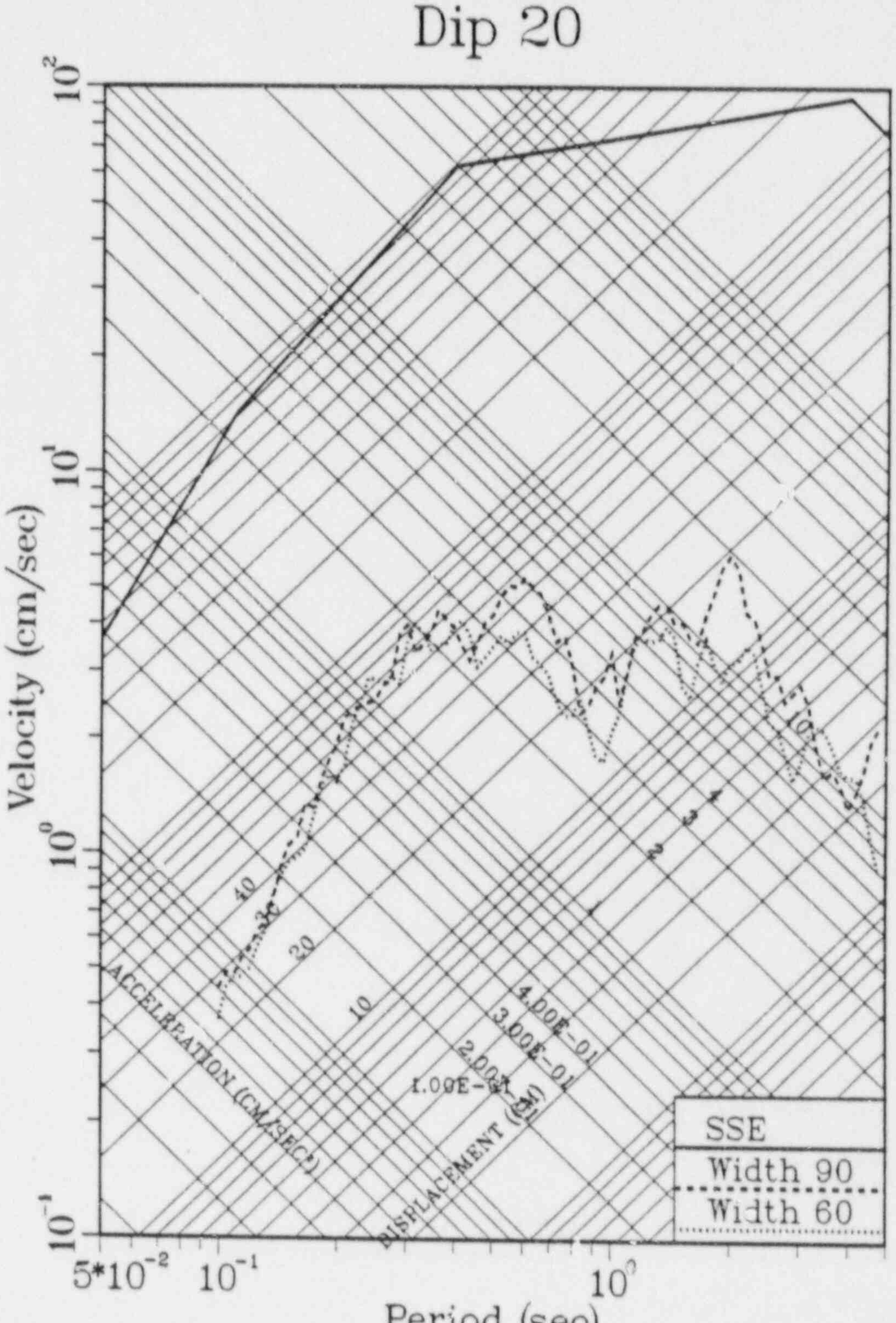

Figure D.9. Simulated 5 percent damped response spectra at the WNP-3 site for an earthquake with a dip of 20°, central rupture initiation point, and widths of 90 km and 60 km.

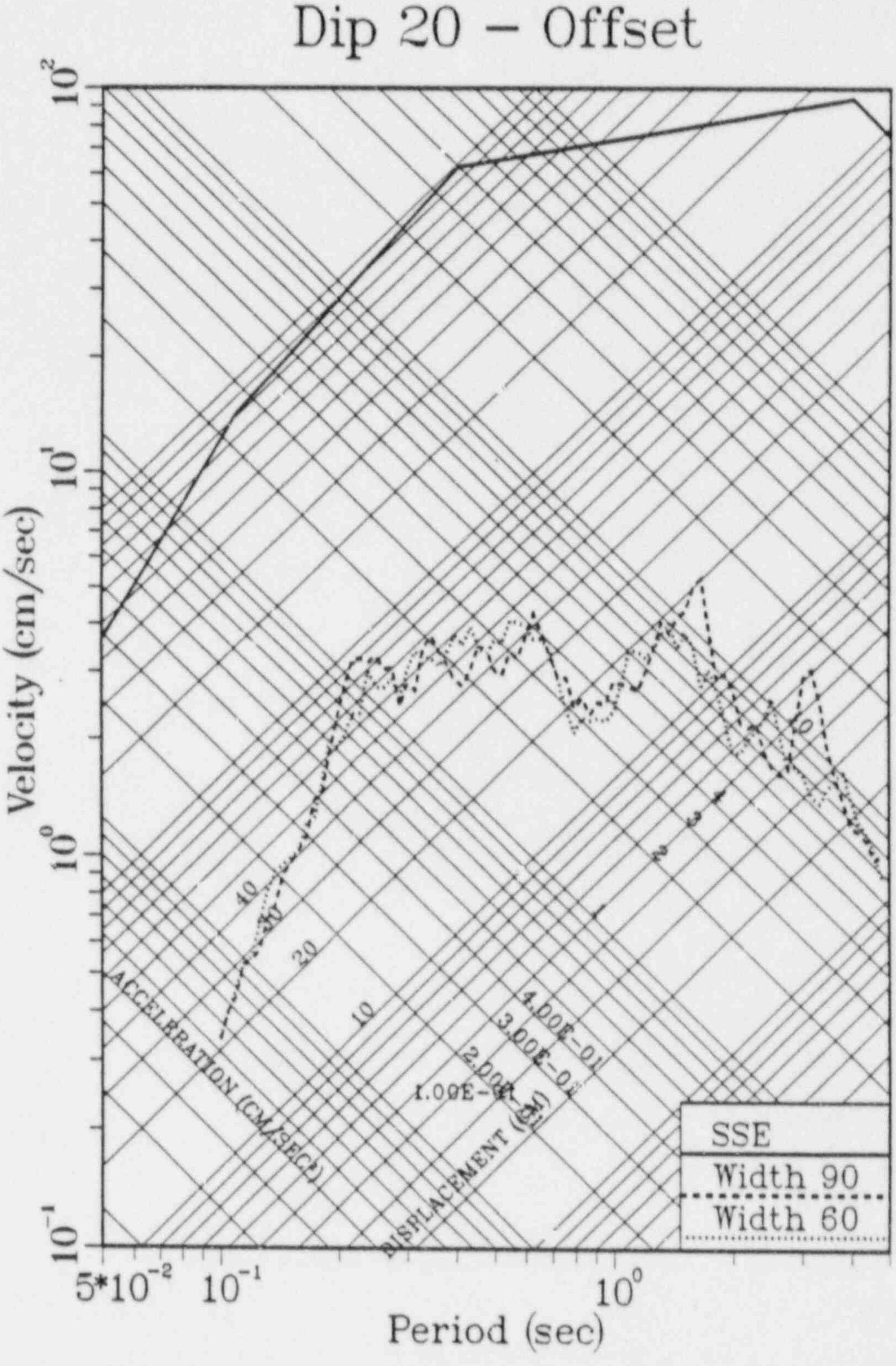

Figure D.10. Simulated 5 percent damped response spectra at the WNP-3 site for an earthquake with a dip of 20°, offset rupture initiation point, and widths of 90 km and 60 km.